INTERNAL STRUCTURE OF POLYELECTROLYTE MULTILAYERS ON NANOMETER SCALE

I n a u g u r a l d i s s e r t a t i o n

zur

Erlangung des akademischen Grades eines

Doktors der Naturwissenschaften

der

Mathematisch-Naturwissenschaftlichen Fakultät

der

Ernst-Moritz-Arndt-Universität Greifswald

vorgelegt von

Oxana Ivanova

geboren am 06. April 1980

in Sankt-Petersburg (Russland)

- Greifswald, 2010 -

Dekan:	Prof. Dr. Dr. Klaus Fesser
1. Gutachter:	Prof. Dr. Christiane A. Helm
2. Gutachter:	Prof. Dr. Monika Schönhoff
Tag der Promotion:	15. Oktober 2010

Ich möchte mich ganz herzlich bei allen Mitarbeitern des Instituts für Physik für zahllose fachverwandte sowie fachfremde Unterstützung bedanken.

Contents

Part I

Introduction to the Field of Research

Chapter 1

Introduction

The idea to create materials with specific properties is as old as mankind. Besides the knowledge how to create the material, the knowledge how to manipulate it in a proper way is essential. This requires deep understanding of background physics and chemistry, especially of surface phenomena at the nanoscale. Development of new experimental methods makes the nano–cosmos accessible as a tool for advanced materials. Increasing importance of functionalized surfaces and nanocomposite systems places their properties in the foreground of scientific and technical interest. Flexible composition control of such systems can be gained by use of multilayer technology.

The polyelectrolyte multilayers are a new class of organic thin films that allow precise control of film thickness within a few nanometers. Furthermore, it is possible to manipulate molecular architectures composed of a number of functional materials and study physical phenomena on the molecular level.

1.1 Polyelectrolytes and their Properties

The term polyelectrolyte denotes a class of macromolecular compounds or polymers with high molecular weight whose repeating units bear an electrolyte group that dissociates in a suitable polar solvent (usually water) and acquires a large number of elementary charges. In Fig. 1.1 a general schematic of the polyelectrolyte structure is shown. The polyelectrolyte ionizable groups, whose dissociation in solution makes the polyelectrolyte charged, leave ions of one sign bound to the chain and mobile counterions in solution. The charged groups contribute substantially to the chain stiffness and conformational degrees of freedom. The properties of polyelectrolytes are similar to both: electrolytes (they exhibit electrolytic conductivity and interionic interaction) and neutral polymers (their solutions are often viscous).

Polyelectrolytes are classified according to their origin as either natural or synthetic. Many biological macromolecules are polyelectrolytes. The most important examples are DNA and RNA molecules, which dissociate in solution forming a strongly negatively charged polyion surrounded by an atmosphere of small mobile counterions, like K^+, Na^+, Ca^{+2} and Mg^{+2}. Common synthetic polyelectrolytes are especially interesting for industrial applications because they dissolve in polar solvents like water, instead of most neutral hydrocarbon polymers, which are only soluble in organic solvents [Görnitz1997]. Some natural polyelectrolytes, such as glue and gum, have been used from time immemorial as thickeners. The use of gum as a protective colloid is as old as the use of India ink, which is finely ground

soot, suspended in water and stabilized with gum arabic [Overbeek1976].

Despite their widespread presence and use, polyelectrolytes remain among the least understood materials in soft condensed matter. They are difficult to understand because of the entwined correlations of chain configuration and polyelectrolyte charges. In analogy to acids, one can distinguish weak and strong polyelectrolytes according to the degree of their dissociation in solution. The strong polyelectrolytes completely dissociate in solution and their ionic groups are present in a large pH–window (1<pH<13) in contrast to weak polyelectrolytes that only partially dissociate at intermediate pH (6–8). Since weak polyelectrolytes are not fully charged in solution their fractional charge can be modified by changing the solution pH or ionic strength (measure of the ion concentration in solution).

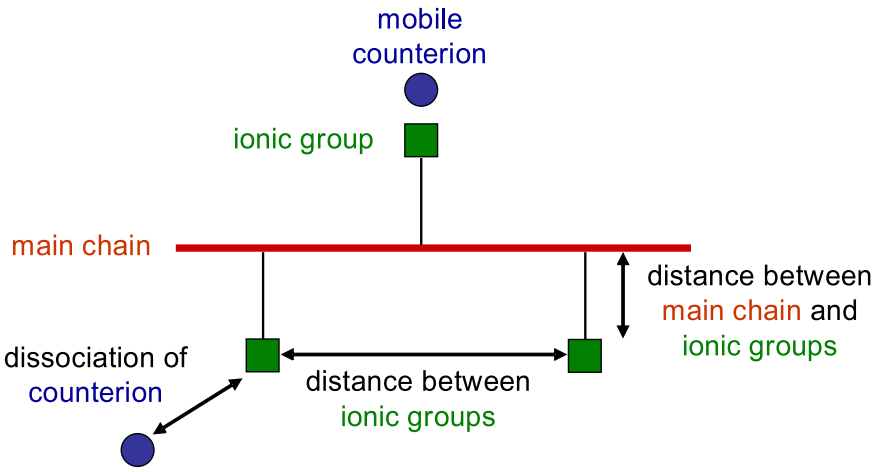

Figure 1.1: Schematic of the polyelectrolyte macromolecule structure. Note that structure may vary for different polyelectrolytes. Idea of the picture is adapted from A. Laschewsky tutorial on polyelectrolytes.

1.2 Layer-by-Layer Assembly of Polyelectrolytes

In 1991, G. Decher and J.–D. Hong presented a new layer-by-layer (LbL) sequential assembly technique for depositing ultrathin films [Decher1991]. This technique was first suggested by R. K. Iler with regard to the concept of creating layers of oppositely charged colloidal particles [Iler1966]. Each time that an initially charged substrate is exposed to a solution of oppositely charged polyions, a definite amount of polyelectrolyte (PE) is adsorbed. Provided that each adsorption step leads to charge inversion of the surface, the subsequent deposition finally results in a layered complex, stabilized by strong electrostatic forces, so–called self–assembled polyelectrolyte multilayer (PEM) [Schönhoff2003a]. Schematic illustration of the first two adsorption steps and resulting polyelectrolyte multilayer system, consisting of several layers deposited onto planar solid support is shown in Figure 1.2. It is important to note that with the exception of the conventional solution–dipping method developed by Decher (a technique also used in this thesis) spraying and spin self–assembly methods were introduced more recently [Schlenoff2000], [Cho2001]. These techniques provide much shorter processing times for multilayer build–up, which is important for PEMs, consisting of a large number of layers; however, they have certain disadvantages. Thus, difference in film thick-

ness between dipping and spraying is not fully understood. Also, the spin self–assembly method is restricted with respect to the substrate size and planarity.

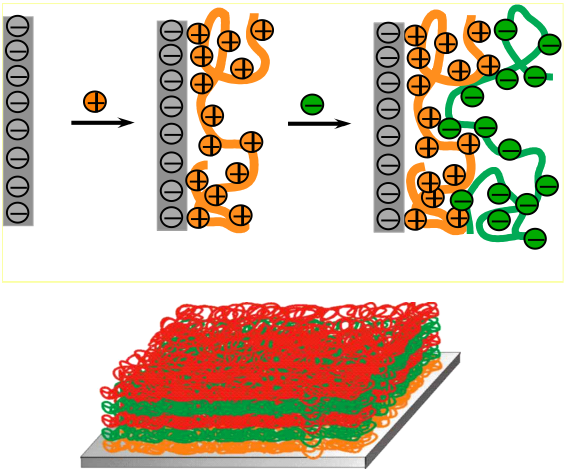

Figure 1.2: Schematic of the layer-by-layer assembly (top) resulting in ultra–thin polyelectrolyte multilayer film adsorbed onto solid substrate (bottom). Here different colors represent positively and negatively charged polyelectrolytes (polycations and polyanions) respectively. Charge of the substrate is shown in gray circles.

In contrast to other thin film deposition techniques that have been reported in the literature, an alternative approach - LbL adsorption of polyanions and polycations - is far more general. This technique is independent on the size, shape and topology of the substrate and has been extended to other materials such as proteins or colloids [Decher1997]. Indeed, the well known vacuum (physical vapor) deposition technique requires specialized expensive instrumentation and specific type of substrates [Mattox2003]; spin coating is restricted to the macro- and nanofilms, in this case contamination by dust is likely and film thicknesses on the order of one molecular layer cannot be achieved [Pauleau2002]; both, chemisorption (where the chains are attached through establishment of a covalent bond between the substrate and the polymer) [Oura2003] and the Langmuir–Blodgett technique (in which monolayers are formed on a water surface and then transferred onto a solid substrate) can be used only with certain classes of molecules [Ulman1991].

The adsorption of PEM on a solid surface is possible due to the presence of electric surface charge that appears when the surface is immersed in water. Generally, a surface may become charged either by ionization/dissociation of surface chemical groups or as a result of adsorption of ions from the surrounding solution [Reinhardt2008]. Most of the surfaces used as support for multilayer build–up (like silicon, quartz, glass etc.) become negatively charged in water. In the case of silicon which is material used in this work, the surface charge is negative due to OH^- groups produced by exposure of the clean silicon surface to air. Details on PEM build–up, silicon cleaning procedure and the structural formulas of polyelectrolytes applied in this thesis are given in Chapter 3. The physics of polyelectrolyte multilayer formation will be discussed in the following chapter.

The versatility of the multilayer formation process with respect to the variety of materials which can be used as building blocks, and furthermore the possibility of combination with other assembly procedures results in a high application potential for a broad range of different

areas of materials development [Schönhoff2003b]. For example, polyelectrolyte multilayers can be used in light–emitting devices [Fou1996], sensor applications [Rubinstein1989], as gas separation membranes [Tieke2000], hydrophobic and antireflection coatings [Hiller2002], Bragg mirrors [Zhai2004] and so on. Interesting applications due to the self–organization of polyelectrolyte multilayers include incorporation of proteins [Lvov1995], [Jessel2003], [Wittmera2007], dye molecules [Nicol2003], colloids [Bogdanovic2002] and even fullerenes [Bae1995].

Besides multilayers that adsorb on planar surfaces (so–called, planar multilayers), micro- and nanocapsules covered by PEMs also have a broad range of applications, e.g. in encapsulation as drug carrier systems [Antipov2004], [Zhu2007] or microreactors [Dähne2001]. The build–up of capsules is realized by coating of colloidal particles with polyelectrolytes and subsequent removal of the core [Donath1998], that result in stable, hollow polymeric shell structures (see Fig. 1.3).

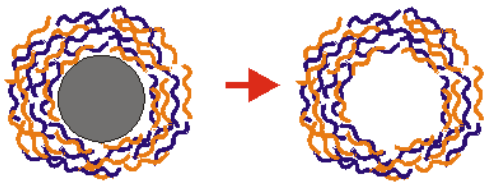

Figure 1.3: Schematic representation of the polyelectrolyte multilayer film adsorbed onto spherical particle (left) and the resulting hollow polyelectrolyte capsule after removal of the core (right).

All potential applications (in biotechnology, medicine or industry) require basic understanding of the PEM structure and control in the process of layer formation. Due to practical significance and theoretical interest, much effort has been made to clarify the unique characteristics of metal–polymer multilayers adsorbed onto planar support. Besides steric stabilization (spatial arrangement), polyelectrolytes provide additional electrostatic strengthening, also known as electrosteric stabilization of colloids [Notea2006]. As a result, nanoparticles can show their unique optical and electrical performance, while the composites show typical properties of organic polymers, such as elasticity, transparency etc. Often, the multicomposites exhibit properties which go beyond those of the various constituents. Optical theory of metallic nanoparticles is presented in Section 4.2.

Commonly used methods for characterization of polyelectrolyte multilayer structures are optical techniques, like UV–Vis spectroscopy and ellipsometry; mechanical techniques, like quartz crystal microbalance (QCM) that allows the measurement of mass adsorbed during the multilayer build–up; reflectivity techniques like X–ray or neutron reflectivity; surface sensitive microscopic methods, like scanning probe microscopy (SPM) and particularly atomic force microscopy (AFM); different electrochemical techniques for investigation of ion transport and so on.

The data presented in this thesis are obtained by X–ray and neutron reflectivity, AFM and UV–Vis spectroscopy. These techniques deliver significant information for this study regarding the thickness and composition of thin films. X–ray reflectivity is sensitive to electron density gradients, and therefore provides information about film thickness, average electron density and film–air roughness. Neutrons are the unique probe that is sensitive to the inter-

nal order of the multilayers (scattering length density variation) due to partial deuteration of the layers. UV–Vis light induces the characteristic absorption peak of polyelectrolytes and embedded nanoparticles. AFM allows the observation of film structures at the molecular level and the characterization of the surface topology of the films.

1.3 LbL Multilayers: State of the Art and Properties

PEMs are complex materials with interesting properties on different length scales. On the segmental scale, they are combined similarly to polyion complexes in solution and on a scale larger then several nanometers their behaviour is determined by internal interfaces, since they form two–dimensional stratified layers, which are growing step–by–step into the third dimension [Schönhoff2003a]. The nanoscale arrangements of organic molecules can be controlled at least in one dimension (along the layer normal) by the number of adsorbed layers [Decher1997]. The thickness of a single layer is of the order of several Ångstroms and, therefore, the total film thickness can be precisely tuned by the number of adsorbed layers. Since the segmental distribution of one polyelectrolyte layer exceeds its thickness, the monomer density is constant along the surface normal for both polycations and polyanions [Schönhoff2003b].

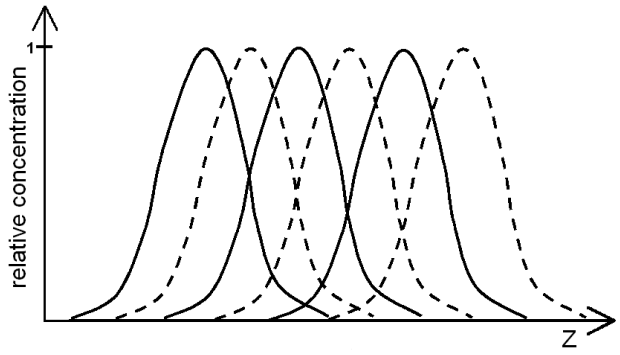

Figure 1.4: Schematic of the segmental distribution of polyanions and polycations in PEM introduced by Decher, *Science* (1997). Relative concentration of ionic groups is plotted against surface normal. In this model each layer is represented by an arbitrarily chosen sinusoidal concentration profile. Dashed and full curves corresponding to polyanions and polycations, respectively. The sum of the concentration of equal ionic groups is unity in both the cationic and anionic case. This picture is adapted from M. Schönhoff, *Curr. Opin. Col. and Interf. Sci.* (2003).

PEMs prepared by the LbL technique show a strong interpenetration between the oppositely charged neighboring layers, avoiding defect propagation from layer to layer. A film model in which high overlap of the layers of equal charge allows 1:1 stoichiometry of anionic and cationic groups within the film is shown in Fig. 1.4. The interpenetration of consecutive layers is accompanied by the formation of ion contact pairs, built by cation and anion monomers of neighboring polyelectrolytes, which are responsible for the pronounced stability of multilayers. Thus, build–up of multilayers can be explained by the formation of polyanion–polycation complexes due to exchange of counter-ions (in some cases polymers also adsorb by hydrogen bonding, i.e. electrostatic force of attraction, which exists between

covalently bonded hydrogen atom of one molecule and an electronegative atom of the other molecule) [Klitzing2004].

Depending on the polyelectrolytes used, one can tune the chemical and physical properties of these ultra–thin films. In accordance with Ladam [Ladam2000] and following [Salomäki2003], the polyelectrolyte multilayer film can be subdivided into three regions (see Fig. 1.5).

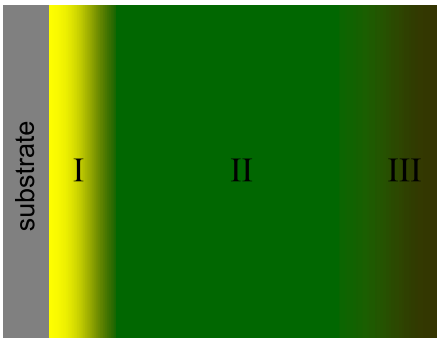

Figure 1.5: Schematic of PEM zone model introduced by Ladam, *Lagmuir* (2000). According to this model, the polyelectrolyte multilayer film can be assumed to consist of three zones, denoted by I, II, and III. Zone I or precursor zone is closest to the substrate and often considerably thinner. Zone II is in the middle or core of the film and zone III is the outer zone close to the surface of the film. The main assumption is the similarity of individual layer pairs in zone II. Note that internal interfaces are not sharp, but kind of "fuzzy" (cf. Fig. 1.4) and therefore transitions between zones are gradual.

The mesoscopic structural aspects of PEMs like multilayer thickness, degree of interpenetration of successive polyelectrolyte layers, the roughness and the surface coverage have been extensively studied in the last years and several reviews have been published that summarize most of the results obtained to date [Schönhoff2003a], [Schönhoff2003b], [Klitzing2006]. Thus, the type of polyelectrolyte affects the total PEM thickness and the type of multilayer growth; polyelectrolyte layers are strongly interpenetrated and there are no clear borderlines between them [Decher1997], [Gopinadhan2005]. The film thickness of some polyelectrolyte systems increases linearly with number of deposition cycles, while for other systems – exponentially [Hübsch2004]. The balance between hydrophobicity and hydrophilicity of the polyelectrolytes seems to play an important role for the thickness. A certain degree of hydrophobicity induces a stronger increase in multilayer thickness [Klitzing2004].

The response of multilayers on external conditions during build–up as well as on post–deposition treatment is attracting increasing attention. Thus, influence of the salt content of the deposition solutions [Dubas1999], the charge density of the polyions [Elzbieciak2008] (either varied by charge dilution in copolymers or as a result of the pH in weak polyion solutions), the charge density of the polycations during swelling of PEMs [Köler2009] etc has been reported. The effect of deposition temperature on the build-up of polyelectrolyte multilayers has received comparatively little attention, despite the fact that the observed effects are reasonably large. It was found, that the film thickness increases by up to 75% on temperature rise from 5^0 C to 45^0 C for PEMs built from 1 mol/L salt solution [Büscher2002], [Gopinadhan2005]. A profound influence on the the rate of multilayer

build–up due to increase of temperature in the deposition process has been demonstrated by Salomäki [Salomäki2005].

Nowadays more and more studies are focused on the molecular–scale properties of polyelectrolyte multilayers. A major interest here is the possibility to tune the composition of the membrane and its thickness on the nanometer scale. Thus, one of the most important questions concerns the water content of the multilayer film or capsule wall, respectively, which determines key properties like permeability and elasticity [Schönhoff2007]. Moreover, swelling in water or in other solvents provides crucial information about the internal properties of PEMs. Fundamental work has further addressed questions concerning the role of secondary interactions, and response to variations in the external environment, such as e.g. temperature, screening of electrostatics, etc.

1.4 Objectives

The present work investigate the influence of preparation conditions, as well as external parameters on polyelectrolyte multilayer films. Polyelectrolyte multilayers (PEMs) are formed by sequential adsorption from aqueous solutions of oppositely charged poly (allylamine hydrochloride) (PAH) and poly (styrene sulfonate) (PSS) polyelectrolytes. The properties of the resulting ultrathin films are quantified in terms of parameters on a molecular scale. The main issues discussed in this work address the following questions:

- Is swelling of PEMs in heavy and light water reversible for the investigated system? How tight is the water bound?
- How do the properties of PEMs, such as film thickness, internal and outer roughness and amount of water bound to the layer, depend on experimental conditions such as the preparation temperature and the type of salt in the polyelectrolyte solution?
- How does the incorporation of a nanoparticle monolayer into PEM affect their aggregation?

The thesis is divided into four parts as follows: The first chapter provides an introduction to the problem. Here, basic concepts are introduced and a brief overview of the state of the art is given. In the next chapter, the physics of the underlying processes are discussed. Part two starts with chapter 3 which contains basic information about the materials used in this thesis and provides a description of the preparation procedure of colloidal nanoparticles and multilayered thin films (consisting of either organic compounds or inorganic matter adsorbed onto solid surfaces). The principles of the diagnostic techniques employed for investigation of both overall and internal film structure, surface topology and optical properties of thin films are described in chapter 4. Chapter 5 discusses the analysis of experimental data. The third part of the thesis reports the experimental results obtained. It is divided into three chapters, each of them dealing with different aspects of the PEM properties:

- Chapter 6 deals with the impact of relative humidity on the PEM properties and proton – deuterium exchange in PAH monomer during swelling.
- In chapter seven, the influence of preparation conditions on PAH/PSS polyelectrolyte multilayer systems is investigated.

- The investigation of silver nanoparticle composition in polyelectrolyte multilayer system is presented in the chapter eight.

The final part of the thesis contains a summary of the experimental results obtained. Here, additional information concerning symbols and bibliography is also provided.

Chapter 2

Physical Background

In order to understand the fundamental physical properties of multilayers, leading to the strong response of polyelectrolyte multilayers (PEMs) to variation of external conditions in the studied system, the basic principles of multilayer formation are reviewed here.

2.1 Influence of Electrostatic and Non–Electrostatic Interactions

The formation of polyelectrolyte multilayer architectures is based on alternating deposition of oppositely charged polyelectrolytes (polycations and polyanions) from aqueous solution to a solid support [Decher1991]. Multiple electrostatic bonds causing a strong attraction between oppositely charged polyelectrolytes are generally discussed as being responsible for the formation and stability of PEMs [Decher1997]. In principle, the adsorption of molecules, carrying more than one equal charge (negative for anionic and positive for cationic polyelectrolytes), allows the charge reversal on the surface (cf. Fig. 2.1, step A).

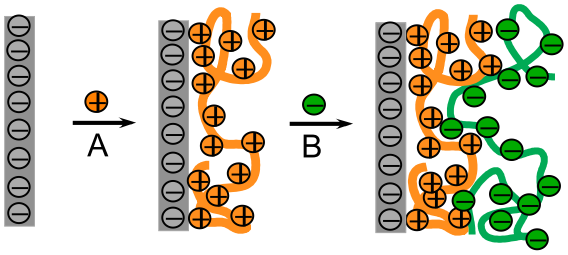

Figure 2.1: Schematic of the molecular details of multilayer formation: absorbtion of positively charged polyelectrolyte on negatively charged substrate leads to the surface charge reversal (step A) that enables formation of simple multilayer film architecture (step B).

This has two important consequences: (i) repulsion of equally charged molecules limits the adsorption to a monolayer, and (ii) the ability of an oppositely charged molecule to be adsorbed in the next step on top of the previous layer (cf. Fig. 2.1, step B). Cyclic repetition of both adsorption steps leads to the formation of multilayer structures. On the one hand the phenomenon of strong electrostatic attraction that occurs between a charged surface and an oppositely charged molecule in solution has long been known to be a factor in the

adsorption of small organics and polyelectrolytes [Stuart1991], but it has rarely been studied with respect to the molecular details of layer formation [Haller1978]. On the other hand, the adsorption of oppositely charged polyelectrolyte layer leads to a local charge neutralization. The apparent contradiction can be solved by the generation of an excess surface charge density used for the next adsorption step (so–called charge overcompensation).

Surface force measurements [Berndt1992] indicated that, indeed, at the initial stage of the adsorption, the polymer forms stoichiometric ion pairs and the layer becomes electroneutral. Yet, at a higher polyion concentration a restructuring process of the adsorbed polymer builds a new double layer by additional binding of polymers [Biesalski2002]. Some experiments [Sukhorukov1998] show that a neutralization and charge overcompensation of a polyelectrolyte layer is achieved by the charges of an adjacent adsorbed layer. The surface potential is difficult to define from the experiment, but ψ_ζ potential (electrical potential in the interfacial double layer) can be determined by e.g. electrokinetic measurements. It was found, that after each adsorption step the ψ_ζ potential changes its sign. This experimental result is supported by the theoretical explanation of charge overcompensation, calculated with classical self–consistent mean field theory [Joanny1999]. Thus, under the assumption that charge overcompensation is needed, effect of polymer charge density is crucial since a threshold charge density should be overcome for the formation of multilayers [Schöler2002]. However, recent measurements [Neff2006] show that no change in sign of the ψ_ζ potential is necessary to form PEM and therefore, the driving force for the LbL assembly need not be electrostatic interaction and strongly depends on the investigated system.

2.1.1 Electrostatic Interactions: Electric Double Layer

In aqueous solution the individual properties of the polyelectrolytes assumed to be covered by long ranged intra– and intermolecular Coulomb interactions between the electrical charges of the chain [Görnitz1997]. These expectations are based on mean field theories, such as the Poisson-Boltzmann formalism, which are routinely used in colloid science and computational biology [Israelachvili1992]. Assumptions of this theory are: water is homogeneous continuum with a certain dielectric constant, ions are point charges and do not interact with each other forming continuous charge distribution.

Since for objects suspended in water dissolved ions are always present, the interaction of the charged bodies with the free ions profoundly modifies the nature of the electrostatic interaction [Jones2002]. In particular, the ions in an electrolyte have a screening effect on the electric field from individual ions.

More than a century ago (in 1879) Ludwig Helmholtz proposed simple model of an electric double layer, where surface charges are balanced by a layer of oppositely charged ions (counter–ions). Later, Gouy and Chapman took into account a thermal motion of the ions, that leads to the formation of diffuse layer. The Gouy–Chapman-Stern model combines the Helmholtz single adsorbed layer model with the Gouy–Chapman diffuse layer model [Adamson1997]. Fig. 2.2 demonstrates the representation of this model. Here, rather then a direct Coulomb interaction between two charged bodies, one finds a screened Coulomb interaction which exponentially decays in strength with distance.

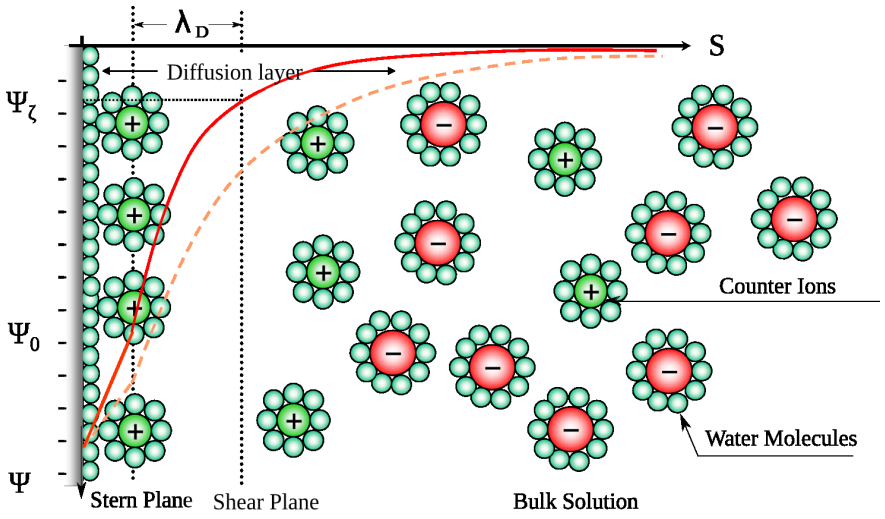

Figure 2.2: Schematic representation of the ion distribution that form a diffuse concentration profile away from the surface. The electrical potential ψ at a negatively charged interface is plotted over the distance s for electrolyte solution without additional salt (dashed line). Here the layer tightly bound to the surface is known as Stern plane. Between the surface (s=0) and this plane potential decreases linearly. Zeta potential (ψ_ζ) is value of the electric potential on the border between mobile and immobile ions surrounding the surface (also called Shear plane). Note that ions are surrounded by a shell of associated water molecules because of the large dipole moment of water. Debye screening length λ_D is the distance over which significant charge separation can occur. By addition of salt (straight line) value of ψ_ζ reduces and eventually approaching zero (electrical double layer collapse). The picture is adapted from PERC, University of Florida.

An electrostatic potential $\psi(s)$ at a distance s from the surface, and density of ions $c_i(s)$ are described by the Boltzmann equation:

$$c_i(s) = c_{i,\infty}\, exp\left(\frac{-\,ze\,\psi(s)}{\mathrm{k_B T}}\right) \tag{2.1}$$

where $c_{i,\infty}$ is ionic concentration in bulk solution, z - valency of the ions, e - elementary charge, ze - the charge of the ions, $\mathrm{k_B} = 1.38 \cdot 10^{-23}$ JK^{-1} - Boltzmann constant, T - ion (solution) temperature.

The potential $\psi(s)$ itself is determined by the distribution of net charge $\varrho(s)$ and given by Poisson equation:

$$\varrho(s) = -\varepsilon_m \varepsilon_0 \left(\frac{d^2\psi}{ds^2}\right) \tag{2.2}$$

where ε_m is the dielectric constant of the medium, ε_0= 8.8·10^{-12} Fm^{-1} - electric permittivity of vacuum. For water at room temperature $\varepsilon_m = 80$, therefore electrostatic interactions are much weaker in water than in air, where $\varepsilon_m = 1$.

Since counterions are needed to balance the charge of the surface, $\varrho = ze$ and combination of two previously written equations gives the well known Poisson–Boltzmann equation:

$$\frac{d^2\psi}{ds^2} = -\left(\frac{ze\, c_{i,\infty}}{\varepsilon_m \varepsilon_0}\right) e^{-\dfrac{ze\psi}{\mathrm{k_B T}}} \tag{2.3}$$

In most of the cases, the aqueous solution contains mobile salt ions that effectively reduce or screen the charges. The salt ions of opposite charge are drawn to the charged object and form a loosely bound counterion cloud around it. For monovalent salts, like NaCl, the concentration of both negatively (c_-) and positevely (c_+) ions can be written as:

$$c_{i,\pm} = c_{i,\infty} \exp\left(\frac{-\,\mathrm{z\,e}\,\psi}{\mathrm{k_B\,T}}\right) \tag{2.4}$$

The net charge density is given by $\varrho(s) = ze\,(c_+ - c_-)$, therefore equation 2.3 can be rewritten as:

$$\frac{d^2\psi}{ds^2} = -\left(\frac{2ze\,c_{i,0}}{\varepsilon_m\varepsilon_0}\right)\sinh\left(\frac{\mathrm{ze}\psi}{\mathrm{k_B T}}\right) \tag{2.5}$$

Under the Debye–Hückel approximation $\sinh\left(\dfrac{\mathrm{ze}\psi}{\mathrm{k_B T}}\right) \approx \dfrac{\mathrm{ze}\psi}{\mathrm{k_B T}}$ with boundary conditions: for an isolated plate in solution both the potential ψ and its gradient $\dfrac{d\psi}{ds} \to 0$ as $s \to \infty$.

Thus, the potential also known as Debye–Hückel potential can be expressed as:

$$\psi(s) = \psi_0\, e^{-\kappa_D\, s} \tag{2.6}$$

where the inverse value of κ_D is the length which characterizes the screening and known as Debye screening length λ_D:

$$\lambda_D = \left(\frac{\varepsilon_m\,\varepsilon_0\,\mathrm{k_B\,T}}{2\,e^2\,n_0\,z^2}\right)^{1/2} \tag{2.7}$$

At distances much greater then λ_D, the strength of the direct electrostatic interaction between charged objects rapidly falls to zero, cf. Fig. 2.2.

In salt solutions, the electrostatic interaction is screened and decays with the Debye length that is related to the ionic strength of the solution I in moles per liter (mol/L) by the following expression:

$$\lambda_D = \frac{1}{(8\pi z^2\, l_B\, \mathrm{I})^{1/2}} \tag{2.8}$$

where ionic strength of the solution is equal to the molar concentration c for 1:1 electrolytes (like NaCl), l_B is Bjerrum length, length over which the electrostatic interaction between two elementary charges e in solution is compensated by the thermal energy $\mathrm{k_B T}$ (l_B=0.7 nm for pure water at room temperature) and defined as:

$$l_B = \frac{e^2}{4\pi\varepsilon_m\varepsilon_0\,\mathrm{k_B\,T}} \tag{2.9}$$

The Bjerrum length is used to describe strength of the Coulomb interaction in polyelectrolytes, since the conformation of polyelectrolyte chains is governed by the electrostatic repulsion of the charges on the chain additionally to Gaussian statistics that describe uncharged chains (neutral polymers) in a good solvent. Water is a good solvent for ions because of its large dielectric constant; in bad solvents polyelectrolytes collapse and precipitate.

2.1.2 Effect of Salt on Formation of PEMs

Additional salt reduces the amplitude and the range of repulsive electrostatic force between equally charged chains or chain segments. The range of the electrostatic interaction is measured by the Debye length λ_D, which is a function of the ionic strength. For monovalent ions and water at 25^0 C, the Debye length is given by the following formula:

$$\lambda_D = \frac{0.3 \text{ nm}}{\sqrt{\text{I}}} \tag{2.10}$$

Thus even for relatively modest salt concentrations electrostatic effects are strongly screened. At physiological conditions (I=0.1 mol/L) and for monovalent ions (z=1) the Debye screening length $\lambda_D \approx 1$ nm. This means that although the Coulomb interactions are long–ranged, at physiological conditions they are strongly screened above length scales of a few nanometers, which results from multi–body correlations between ions in a salt solution [Netz2003]. The Debye–Hückel approximation becomes progressively more accurate with increasing salt concentration and in the limit of zero salt it reduces to Coulomb interactions. When Debye screening length is less or equal to the diameter of water molecules surrounding the ion (0.3 nm), the mean field theory is not appropriate anymore, since it ignores molecular nature of the liquid and therefore, Monte Carlo and molecular dynamics simulations become more meaningful (for more details see [Kotelyanskii2004]). Generally, the mean field theory breaks down at small distances, where it no longer faithfully describes the ionic distribution and forces between two surfaces [Israelachvili1992].

Figure 2.3: Schematic representation of the salt effect on the shape of a polyelectrolyte in solution. Addition of salt makes polyelectrolytes contract into random coils.

Pure electrostatics predicts a flat polyelectrolyte adsorption onto an oppositely charged surface [Netz1999]. Experimental studies [Decher1997] show that the film thickness for some PEM systems increases with increasing salt concentration despite the fact that addition of salt into solution screens electrostatic attraction between the polyelectrolyte and oppositely charged surface. It was reported that the film thickness increases even at higher salt concentrations, up to 3 mol/L [Steitz2000], where the Debye length is smaller then the diameter of hydrated counterion. In this case the electrostatic attraction is completely screened, therefore other interactions should become significant. Thus, due to the screening of the charges along the polyelectrolyte chains by the excessive presence of smaller salt counter–ions in solution, single macromolecule is changing its conformation and becomes more coiled (cf. Fig. 2.3). In pure water the charges on a linear polyelectrolyte chain repel each other due to Coulomb repulsion and therefore the chain has more expanded, rigid–rod–like conformation. By adding salt, the polyelectrolyte chain intents to collapse to a more conventional conformation which is essentially identical to a neutral chain that is usually found to be in a

random conformation in solution. This results in a larger thickness and a stronger roughness of the adsorbed layers [Klitzing2006].

Thus, in order to explain the phenomenological behaviour of layer formation, not only the Coulomb attraction, but also additional contributions to the free energy of complexation have to be considered. These additional interactions generally include: hydrophobic attraction of the chains [Ahrens2004]; steric forces, which restrict the angles of rotation about the backbone [Strobl1996] are predominantly entropic in origin; entropic forces [Schönhoff2003a] such as the entropy increase of counterions as a consequence of their release, hydrogen bonding [Stockton1997] and other interactions. While the electrostatic interactions are qualitatively understood, little is known about the nature, the origin and the influence of secondary forces [Shiratori2000]. The role of electrostatic and non–electrostatic (secondary) interactions for multilayer procedure is a question of major interest.

2.1.3 Classification and Range of Intermolecular Forces

As previously mentioned, at large separation distances the interaction between two solid surfaces in liquid can be described by continuum electrostatic double layer theory (where the individual nature of the molecules, their discrete size, shape, and chemical structure are neglected). At surface separations approaching molecular dimensions, continuum theory breaks down and the discrete molecular nature of the liquid molecules has to be taken into account [Butt2003]. Thus, the interactions within solutions of neutral polymers are presumed to be short–ranged, i.e. of the order of a molecular diameter.

In context of soft condensed matter the order of magnitude of the interactions are usually compared to thermal energies [Jones2002]. At room temperature thermal energie $k_BT = (1.38 \cdot 10^{-23}\text{J/K} \cdot 300\text{K}) = 4.14 \cdot 10^{-21}\text{J}$. If bond energy is very much bigger than the thermal energy at room temperature: $E_{bonds} \gg k_BT$ then stable (chemical) bonds are formed. In contrast, if the bond energy is comparable to the thermal energy or only a few times bigger: $E_{bonds} \geq k_BT$, then there is a finite probability that the bond may be broken and subsequently reformed by thermal agitation, so–called temporary or physical bonds.

- *Van der Waals forces.* These interaction arise between uncharged, weakly interacting atoms and molecules. The interaction is not strongly directional and the typical interaction energy is approximately 10^{-20}J, which is of the same order of magnitude as by interaction of two molecules in contact and as thermal energy k_BT at room temperature.

- *Ionic interactions.* Ionic interactions, describable by Coulomb potential is non–directional and is substantially stronger than the van der Waals interaction. Typically, it is a couple of orders of magnitude larger than k_BT at room temperature. However, the interaction is strongly modified by ions in solution.

- *Hydrogen bonding.* Hydrogen bonding occur between hydrogen atom (which is covalently bounded to an electronegative atom like oxygen and thus has a significant unshielded positive charge) and the other electronegative atom. In such a way hydrogen bonding between water molecules is formed. This attractive energy plays an important role in many biological macromolecules and is about 2 to $6 \cdot 10^{-20}$J that corresponds to 5 to 15 k_BT.

- *The hydrophobic interaction.* The molecular interaction between water and the neutral hydrocarbon–based molecules known as hydrophobic interaction. This interaction is of crucial importance in promoting self–assembly in both biological and non–biological systems [Jones2002]. With the exception of some biological polymers and proteins, most polyelectrolytes have hydrophobic groups [Ahrens2004]. The hydrophobic interaction leads to phase separation between oil and water, so–called hydrophobic effect. Hydrophobic surfaces attract each other [Christenson1992]. Thus, the introduction of molecule that cannot form hydrogen bonds into water decrease the entropy, since water contains a network of strong hydrogen bonds. Therefore, network locally rearranges to maximize the number of hydrogen bonds; this results in restriction of possible configurations of the water molecules close to the solute, thus decreasing their contribution to the entropy. Dissolving polyelectrolyte in water results in formation of a highly ordered shell of water molecules around the macromolecule. Formation of polyelectrolyte multilayer, that includes association of two hydrophobic pairs leads to entropically favorable release of water molecules into the bulk solution.

2.1.4 Temperature Effect: Hydrophobic Interactions

A clear indication of the importance of non–electrostatic interactions for the formation of polyelectrolyte multilayers is the temperature effect. This effect on the film thickness [Büscher2002], internal roughness [Gopinadhan2005] and the rate of the layer-by-layer buildup [Salomäki2005] was reported for multilayers made from various polyelectrolytes in concentrated salt solutions. A likely short–ranged interaction force between polyelectrolytes would be the hydrophobic force acting between the apolar backbones of the chains, since the signature of hydrophobicity is its temperature dependence [Tanford1980], [Dill2003].

Also, by changing solvent quality (from good to bad), e.g. by increasing the preparation temperature, short ranged polymer–polymer attraction is increased and solvent–polymer interaction is reduced [Ahrens2004]. Solvent quality can be described by radius of gyration (that give dimensions of a polymer chain) using Flory's mean field approach [Kleman2003]. Thus, $R_g \sim \mathrm{n}^{\nu}$, where R_g is the radius of gyration of the polymer, n is the number segments (equal to degree of polymerization) of the chain. For good solvent the chain of neutral linear polymer is more expanded (ν=3/5) while for bad solvent the chain segments stay close to each other (ν=1/3). At low temperature, the water molecules surrounding an apolar solute form strong hydrogen bonds (ordered water structure and low enthalpy), cf. Fig. 2.4. And therefore, polyelectrolyte conformation is influenced by water structure and more water can be bound to a monomer pair. By heating solution this water structure breaks and more first-shell water conformations become accessible (higher entropy and higher enthalpy) [Gopinadhan2007b]. Melting the first–shell water allows closer approach of the polymer groups and therefore, short–ranged secondary interaction is more effective. However, the origin of the hydrophobic force is still under debate [Butt2003].

A necessary condition for the action of temperature–dependent secondary forces seems to be that range and amplitude of the electrostatic force are shielded by many ions, which are provided by a high salt concentration in the deposition solution. How large the effect is, depends on the chemical nature of polymers and salt; however, if the polyelectrolyte multilayers are built from pure water, no temperature dependence of the film thickness is found [Tan2003].

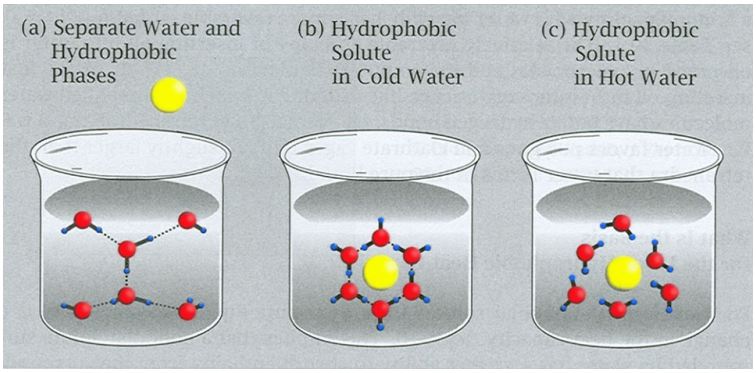

Figure 2.4: The "iceberg" model of the heat capacity, which helps to describe temperature dependence of hydrophobic interaction in water solution: (a) Each water molecule in tetrahedral configuration may participate in three hydrogen bonds. (b) In cold water (near room temperature), water molecules surrounding the non–polar solute form stable hydrogen bonds (low enthalpy) in structured cages (low entropy). (c) In hot water, more first shell water configurations are accessible (higher entropy), but some configurations have weaker or unformed hydrogen bonds and/or van der Waals interactions (higher enthalpy). The picture is adapted from K. A. Dill and S. Bromberg "Molecular Driving Forces" and originally produced by H. S. Frank and M.W. Evans, *J. Chem. Phys.* (1945).

There are also other secondary interactions which may contribute to the increased polyelectrolyte coverage at elevated temperatures. Thus, apolar compounds dissolve in salt solutions to different degrees, depending on the type of salt. In 1888, Franz Hofmeister discovered that different salts have different propensities to precipitate or dissolve proteins in solution [Kunz2004]. The same factors may also influence behaviour of polar polyelectrolytes. Thus, using 0.1 mol/L salt concentrations in the preparation solution of PSS/PDADMA multilayer system, it was found that the thickness of thin (20–90 nm) dry films follows the position of the counteranions in the Hofmeister series. Two parameters describing the interaction of ions with water, the Jones–Dole viscosity coefficient B and the hydration entropy, were used to explain the anion effect on the developing multilayer thickness [Salomäki2004b]. According to [Boström2004], that presented model calculations, performed within a modified ion–specific double layer theory, a detailed theoretical understanding of the Hofmeister effect most likely requires to include hydration forces. Therefore, one can conclude that the multilayer formation is a complex interplay (or balance) between different types of interactions and thus is different from both neutral polymers and electrolyte solutions. To shed some light on the secondary interactions, polyelectrolyte multilayers in this work were prepared at different conditions.

Part II

Materials and Methods

Chapter 3

Materials and Sample Preparation

3.1 Chemicals

Commercial available synthetic polyelectrolytes (PEs) that have been used for multilayer formation are presented in Figure 3.1. By definition PEs are polymers whose repeating units bear an electrolyte group which dissociates in aqueous solutions, making the polymers charged. These flexible macromolecules combine properties of salts and polymers.

In this work, highly branched cationic poly (ethylene imine) (PEI), Mw=75 kDa (Sigma-Aldrich, Taufkirchen, Germany) is used as a primary layer for the substrate charge reversal. Linear polycation poly (allylamine hydrochloride) (PAH), Mw=56 kDa (Sigma-Aldrich, Taufkirchen, Germany) served for the following adsorbing cycles, along with polyanions: protonated and deuterated poly (styrene sulfonate) (PSS and PSS_d) with Mw=77.4 kDa and Mw=83.7 kDa respectively (Polymer Standards Service, Mainz, Germany). All other chemicals used in this work are listed in Table 3.1.

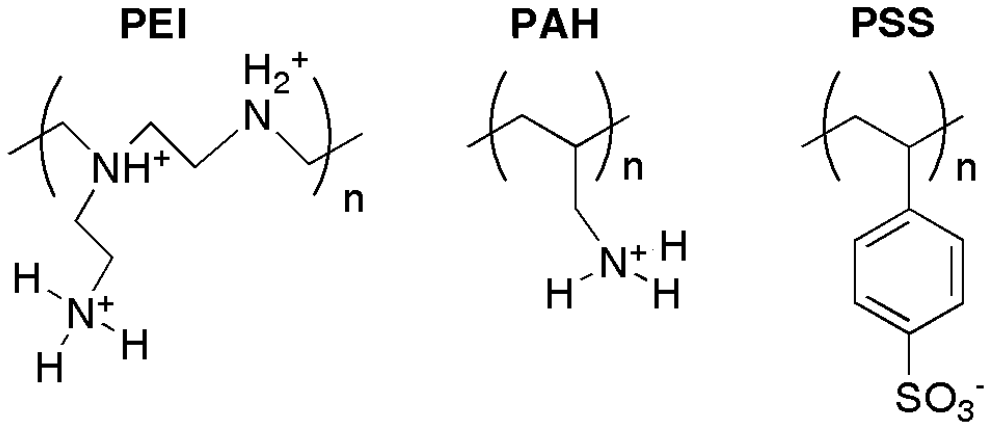

Figure 3.1: Structure formulas of polyelectrolytes applied in this study. From left to right: poly (ethylene imine) or in short form PEI with positively charged amino group NH_3^+, poly (allylamine hydrochloride) or PAH and poly (styrene sulfonate) or PSS with SO_3^- group, where n is degree of polymerization.

Salts (p.a. grade) were either added to the polyelectrolyte dipping solutions (to screen inter- and intramolecular charge repulsion) or used as saturated salt solutions to obtain requisite relative humidity). The relative humidity (respectively water concentration in the gas phase) was obtained by placing Petri dish with unsaturated salt solution into the enclosed experimental chamber under the sample. For given salt and temperature relative humidity (r.h.) value was established after approximately 1 hour. Also, heavy water (D_2O) and phosphorus pentoxide (P_2O_5) were used to obtain 100% D_2O r.h. and 0% r.h., respectively. During X–ray and neutron measurements r.h. and temperature were measured using hydro-thermometer (B+B Thermo–Technik GmbH, Donaueschingen, Germany). X–ray measurements under various humidity conditions were performed inside temperature–humidity chamber (Anton Paar, Graz, Austria).

Formula	Name	Source
NaCl	Sodium chloride	Merck
KCl	Potassium chloride	Merck
CsCl	Cesium chloride	Merck
NaCOOH	Sodium formiate	Merck
NaBr	Sodium bromide	Merck
NaI	Sodium iodide	Merck
$ZnBr_2$	Zinc bromide	Merck
NH_4Cl	Ammonium chloride	Merck
$AgNO_3$	Silver nitrate	Aldrich
$NaBH_4$	Sodium borohydrate	Aldrich
$[-CH_2CHOH-]_n$	Polyvinyl alcohol	Aldrich
NH_4OH	Ammonium hydroxide	Roth
H_2O_2	Hydrogen peroxide	Roth
H_2SO_4	Sulfuric acid	Merck
D_2O	Deuterium oxide	Aldrich
P_2O_5	Phosphorus pentoxide	Merck
C_6H_5Br	Brombenzene	Aldrich
C_3H_5OH	Acetone	Roth
$C_6H_5CH_3$	Toluene	Aldrich

Table 3.1: Nomenclature of chemicals used in this work.

Precise concentrations of the polymer- and salt solutions have been achieved using an laboratory balance Atilon 124-V with an accuracy of ± 0.1 mg (Satorius AG, Göttingen, Germany). All solutions used in this work are prepared with ultra pure deionized water (18.2 $M\Omega \cdot cm$) purified by Milli-Q system from Millipore, Schwalbach, Germany. The chemicals were used as purchased without further purification.

Preparation of Colloidal Silver

Colloidal silver is a homogenous suspension of nanometer–sized silver particles in water. The silver colloidal nanoparticles (NPs) are prepared by chemical reduction of silver nitrate solution (99% purity) according to the description of Lee and Meisel [Lee1982]. This synthesis procedure yields stable (for several months) silver nanoparticles when stored under ambient condition. Procedure can be described as follows: a solution of $5 \cdot 10^{-3}$ M $AgNO_3$, (10 mL)

was added portionwise to freshly prepared ice–cold $3 \cdot 10^{-3}$ M $NaBH_4$ (30 mL). During this process solution was stirred vigorously. Additionally, 1 wt.% PVA solution (5 mL) was added during the reduction to avoid particle aggregation in solution. To eliminate the rest of BH_4^- ions the mixture was heated at 80^0C for ca. 1 h. Clean water was added to compensate for water evaporation and to have a defined concentration. Mechanism of reaction can be expressed as:

$$AgNO_3 \rightarrow \ Ag^+ + NO_3^-$$

$$NaBH_4 + 4H_20 \rightarrow \ NaB(OH)_4 + 4H_2$$

$$2Ag^+ + H_2 \rightarrow \ 2Ag + 2H^+$$

The formation of silver nanoparticles can be observed by a change in color (small nanoparticles of silver appear yellow).[1] After aggregation solution looks muddy. Aggregates can be removed by centrifugation. The prepared Ag colloids obtain mean diameter of 9 ± 2 nm measured by AFM.

3.2 Fabrication of Multilayered Nanofilms

Multilayered structures composed of oppositely charged polyelectrolytes and resulting in polyelectrolyte multilayer (PEM) film with layer thicknesses on the nanoscale are fabricated by layer-by-layer dipping method. As substrates one side polished silicon (100) wafers with surface roughness about 3 Å (Matthias Schmehl, Rostock, Germany) were typically used for the measurements presented in this thesis. For optical measurements, however, quartz glass samples (Crystal GmbH, Berlin, Germany) transparent to the wavelength in the region of investigation ($\lambda > 190$ nm) were employed. One side polished silicon blocks ($8 \times 5 \times 1.5$ cm) with surface roughness < 6 Å (Andrea Holm, Tann, Germany) were used for neutron reflectometry measurements in solid–liquid interface. Sample size varied upon requirement from 1.5×1.5 cm^2 for AFM and 3.8×1.2 cm^2 quartz samples for optical measurements to 5×8 cm^2 silicon wafers for neutron reflection.

To obtain clean hydrophilic surface, substrates were chemically cleaned by using standard RCA procedure (developed by Werner Kern in 1965) that removes organic impurities. This cleaning procedure can be described as following: pure deionized water (H_2O), 27% ammonium hydroxide (NH_4OH) and 30% hydrogen peroxide (H_2O_2) are used in ratio (5:1:1). In the beginning of the procedure water and ammonium hydroxide are mixed in a special quartz beaker (to prevent ion incorporation) and heated to 70 ± 5^0C, then hydrogen peroxide is added. When mixture starts to bubble, substrates are immersed in solution for 15 min, afterwards extensively rinsed with deionized water and kept in pure water afterwards. For substrates that were reused, for example, expensive quartz samples, piranha cleaning procedure was employed [Huff2009]. It involves mixture of concentrated sulphuric acid (H_2SO_4) and hydrogen peroxide (H_2O_2), that is highly oxidative and removes metals and organic contamination. Since the mixing is an exothermic reaction (caution, large amount of heat can be released), H_2SO_4 is added slowly while stirring to H_2O_2 in ratio 1:5. Both oxidizing aqueous cleaning procedures leave 6 – 15 Å of hydroxylated oxide on the Si surface that prevents recontamination [Huff2009]. Such surfaces are hydrophilic in nature and negatively charged in water.

[1] Synthesis of Ag colloids is carried out by Matthis Höhne, Institute of Biochemistry, Greifswald

Cleaned substrates were dipped into the respective polyelectrolyte or colloidal (in case of metal–containing PEMs) solution alternately, forming layer-by-layer (LbL) assembly. The LbL dipping method is based on alternating immersions of oppositely charged substrate in polycation– and polyanion – containing solutions with a rinse in pure water between each adsorption step (cf. Fig. 3.2). Here arrows represent the absorption procedure and beakers – corresponding polyelectrolyte solutions with polycations PEI, PAH and polyanions PSS, PSS_d. First, adsorption of a polycation layer leads to surface charge overcompensation, therefore the sign of net charge is inverse and adsorption of oppositely charged polyanion layer becomes possible (cf. Fig. 3.3). This process is continued until desired number of layers is achieved and polyelectrolyte multilayer film is formed.

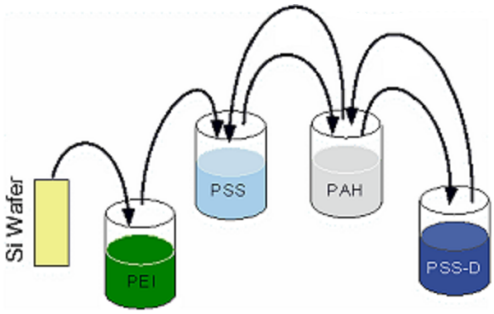

Figure 3.2: Schematic of the film deposition process based on dipping substrate in charged solutions.

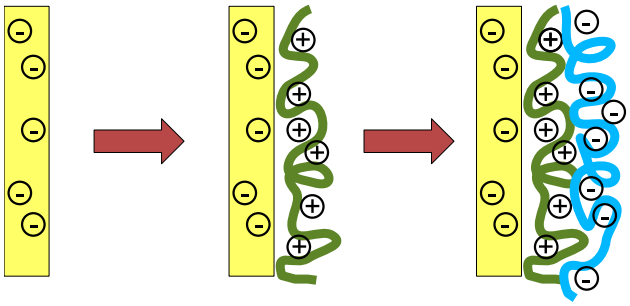

Figure 3.3: Schematic of the first two adsorption steps, starting with a negatively charged substrate.

The initial (precursor) layer for all films was PEI, since PAH doesn't stick very well on silicon wafer [Schmitt1999]. PEI layer was followed by the alternate adsorption of polyelectrolytes or silver nanoparticles. The adsorption times per layer range from minutes in the case of polyelectrolytes to hours in the case of nanoparticles, depending on molar masses, concentrations, and agitation of the solutions. In presented study, each adsorption step took 30 min, except diffusion experiments for silver nanoparticles, were time was varied. Saturation for chosen PAH/PSS system with $3 \cdot 10^{-3}$ mol/L (with respect to the monomer) polyelectrolyte concentration occur after 20 min [Schmitt1996]. Additional excess ensures that the solutions do not become depleted during the fabrication of films composed of several tens of layers. Known minimal value for self assembly process is $3 \cdot 10^{-7}$ mol/L (with respect to the monomer) for salt free PSS solution [Okubo1999]. The polymer concentration in solution doesn't change significantly, accordingly to our UV–Vis measurements of the PSS absorption peak (absorbance remains constant) even after several tens of adsorption steps. Also, it was shown [Marra1983] that up to 1 mg/m^2 PSS can be adsorbed on mica surface in presence of NaCl. The polyelectrolyte films are typically deposited in presence of 1 mol/L salt, except those indicated specially. After the adsorption of each layer substrates were dipped into ultrapure deionized water (three beakers for 1 min each) to avoid contamination of the next adsorption solution and remove loosely bound excess polyelectrolytes and salt ions. The concentration of salt by washing reduces logarithmically and therefore, in the last beaker almost no salt ions are present. Note that salt ions are not incorporated into the bulk of the PEM even in strongly dissociated polyanion/ polycation pair, as shown by radiochemical methods [Schlenoff1998].

In case of few number of layers and room temperature conditions, samples, especially small (3.8×1.2×0.1 cm) quartz samples were prepared manually. Otherwise, robot system (Riegler & Kirstein, Germany) was applied. This system allow to obtain multilayered films with highly reproducible preparation cycle (resulting in layer homogeneity), provides constant velocity, precise positioning of the substrate holder and simultaneous preparation of up to 4 samples. All beakers (solutions and water) were kept at the same temperature that was adjusted externally by a thermostat (Haake, Germany) and varied in the range of 5 to 60°C, except the first PEI layer. It turned out to be more rough at higher temperatures and therefore, has always been prepared at room temperature separately. After preparation, samples were dried with a gentle stream of dry air and stored at ambient conditions. The films were first examined latest two weeks after preparation to avoid aging effects.

Since combination of polycation/polyanion layers is called polyelectrolyte pair or bilayer (BL), resulting multilayer structure consists of number N of BL, where N refers to the bilayer number and varies in this work from 1 to 19. To avoid large names of resulting polyelectrolyte multilayer architectures, following abbreviations were introduces: p – for protonated and d – for deuterated slabs. It allows us to rewrite, for example PEI/$(PSS/PAH)_N$/$(PSS_d/PAH)_{K-1}$/PSS_d structure as $p_N d_K$ (PSS_d has been employed to get the scattering contrast for neutron measurements). Mainly, PEM architectures presented in this work terminated with polyanions, i.e. consist of integer number of BL.

Chapter 4

Characterization Methods

In order to characterize prepared samples, following independent and complimentary techniques are used:

- X–ray reflectivity (XRR) diagnostic, which is sensitive to the overall film structure (parallel to the surface normal) like thickness, electron density and roughness.
- Neutron reflectivity, which provides information on internal vertical film structure (internal roughness and amount of water bound to the layers) due to large contrast between ^{1}H and ^{2}H, as well as total film thickness.
- UV–Vis absorption spectroscopy, which allows to probe aggregation of metallic nanoparticles by measuring their absorption spectra (imaginary part of the refraction index).
- Atomic Force Microscopy (AFM), which is used to obtain nano–scale topological images of lateral film structure (up to 10^4 times better resolution than the optical diffraction limit) by using the forces between the sample surface and a probe.

Thus, methods which measure in-plane structure within the surface plane (or, in case of buried interfaces, within the interface plane) and methods which measure out-of-plane structure, i.e. segment density profiles are discussed below.

4.1 X-ray and Neutron Reflectivity

To obtain structural information on Å – length scales along the substrate normal, non–destructive and non–contact reflectivity techniques involving X–ray and neutron radiation are used. X–ray and neutron reflectivity are based on the interference of beams reflected from different interfaces (substrate and film in a simple case), while diffraction results from the interference from periodic lattice planes. The advantage of the reflection is that not only crystalline film material, but also amorphous and even liquid samples can be examined. Since the underlying principles of reflection are identical for these methods, they are discussed below together. Both, X–rays and neutrons possess wave characteristics and can be reflected from substrate. While X-rays interact with electrons of an atom and neutrons with its nucleus, reflectivity measurements are sensitive to inhomogeneities of the electron or nuclear scattering length density, respectively.

Unlike AFM, that probes surface locally, low angle X–ray and neutron reflectivity provide information averaged over a large volume (illuminated area). X–ray reflectivity (XRR) is sensitive to the total film thickness, surface (outer) roughness, average electron density (per $Å^3$) and its gradient normal to the surface. Neutron reflectivity enables enhanced contrast between two chemically equivalent species due to the pronounced differences in the scattering length density of different isotopes (that describes interaction between neutron and nucleus) and offers a possibility to label molecules [Penfold2000].

The neutron scattering length b is a nuclear property describing the interaction between the neutrons and the atomic nucleus. The value of b varies across the periodic table of elements and also between isotopes of the same element not only in magnitude, but also in sign unlike the electron density which varies with atomic number. The sign of the scattering length depends on the isotope and the nuclear spin state of the element. Therefore, in contrast to X–rays neutrons can distinguish between atoms of the same atomic number. Isotopes of the same element have different atomic masses since they differ in neutron numbers (neutrons are scattered by the nucleus of an atom). Thus, neutron reflectivity is sensitive to the internal order of the multilayers consisting of organic materials, where neutrons are strongly scattered by light atoms like H, C, O and N. The large difference in scattering lengths for hydrogen ^{1}H (or H) and deuterium ^{2}H (or D) provides contrast between structural features by selective replacement of H by D and therefore have a big advantage over X–rays [Fragnetto-Cusani2001]. However, neutron reflectivity is expensive and not easy accessible.

Both of these techniques are sensitive to the distribution of the refractive index of the sample and widely used for probing surface structure of polymers in solution, adsorbed polymers, organic (bio-) molecules and multilayered systems [Jones1999], [Torikai2007]. Due to similar index of refraction of the investigated PAH/PSS system and H_2O, X–ray reflectivity cannot access the buried interfaces and therefore, cannot determine the film composition, i.e. determine the hydration degree of the film. Therefore, X–ray and neutron reflectivity are used to provide complementary information by varying contrast within the sample.

Source of Rays

X–rays are typically produced by fast acceleration of charged particles (bremsstrahlung) or high energy transition between electron shells of atoms or molecules [Demtröder2005]. Both of these effects are used in X–ray tubes, where emitted electrons accelerate under the influence of electric potential difference between cathode and anode (where acceleration is too small for X–rays emission) and hit anode, where they are jammed (in this case X–rays are emitted due to bremsstrahlung) and at the same time electrons are ejected from the inner shells of the atoms of the metal target (anode). Those vacancies are filled by electrons dropping down from higher levels, creating a photon of an energy which corresponds to the energy difference between the states concerned. Thus, X–rays with characteristic frequencies are emitted (the most intense line is K_α doublet). After reflecting from the substrate, X–rays are detected. Since the main part of the kinetic energy of the electrons striking the target is converted into heat, less than 1% being transformed into X–rays, and therefore water–cooling of the anode is needed. Measurements were performed using Cu K_α radiation with wavelength of 1.54 Å and corresponding energy of 8.8 keV.

The production of free neutrons requires either a nuclear reactor, where a continuous beam is produced by nuclear fusion, or a synchrotron source, where a pulsed neutron beam

is obtained. Neutrons used in present study are produced by nuclear fission of Uranium 235 in a research reactor. Small liquid–deuterium vessels in the reactor tank decrease the average neutron velocity (neutrons are produced with a thermal velocity distribution) and yield cold (slow) neutrons with wavelengths in the range of 4 to 20 Å, which are useful for characterization of organic materials.

Interaction with Matter

The main reason for all X–ray – atom interactions can be described as the acceleration experienced by an atom–bound electron from the oscillating electric field of X–ray electromagnetic wave. While the probability of the interaction is approximately proportional to λ^3, short wavelength photons are very penetrating and nearly no absorption occurs [Lifshin1999]. There are several types of interactions of X–ray with matter that include: photoelectric effect, Compton scattering (also called incoherent scattering), absorption, pair production and Thomson scattering. The latter mechanism of X–ray interaction with matter (Thomson scattering) leads to phenomenon of reflection. Thomson scattering is coherent and analogous to a perfectly elastic collision between a photon and electron (scattered photon changes direction, but keeps its phase and energy, $\lambda = \lambda'$). X–rays with energies around (≈ 10 keV) lie far above the binding energy of the most electrons of an atom. Because of the energy transfer is small compared to the incident energy of the photon, inelastic effects are negligible for X–rays. Neutrons, being uncharged particles, interact with matter by collisions with atoms nuclear. There are two main types of neutron – nuclear reactions: elastic and inelastic scattering. However, the probability of inelastic scattering is generally lower than elastic and can be neglected in the small angle range [Lifshin1999]. Therefore, analogous to X–ray reflection, elastic scattering process ($\lambda = \lambda'$) are supposed. The interaction between neutrons and atoms for nonmagnetic systems and elastic scattering is described by the scattering length b of the corresponding nucleus. Because of the short wavelength (1.54 Å for X–rays and 4.66 Å for neutrons), X–ray and neutron reflectivity measurements have resolution of a fraction of nanometer, in contrast to light reflectivity which is sensitive to interfacial features at the length scale of about 100 nm. Thus, information can be gained at the molecular level.

4.1.1 Basic Principles of X–ray and Neutron Reflection

By analogy with geometric optics [Born1999], the interaction of X–rays or neutrons with matter can be described by index of refraction n. Unlike visible light, phase velocity of X–rays and neutrons in medium is generally higher than in vacuum, therefore the refractive index $n < 1$ (apart from light water and compounds that are heavily hydrogenous) [Daillant2009]. For X–rays and neutrons with wavelength λ of the order of Å the complex refractive index is given by

$$n = 1 - \delta + i \cdot \beta \tag{4.1}$$

where the real part of n is less than 1 and small parameters $\delta(\lambda)$ and $\beta(\lambda)$ describe the dispersion and absorption terms [Chason 1997]. The real part of 1–δ is associated with the phase–lag of the propagation wave, while imaginary part β corresponds to the decrease of

the wave amplitude. The dispersion term δ can be expressed as:

$$\text{for X} - \text{rays}: \ \delta = \left(\frac{\lambda^2}{2\pi}\right) r_e \, \rho_e \tag{4.2}$$

$$\text{for neutrons}: \ \delta = \left(\frac{\lambda^2}{2\pi}\right) \rho \tag{4.3}$$

where ρ_e is electron density of the material, $\mathrm{r_e} = \mathrm{e}^2/\mathrm{mc}^2 = 2.82 \cdot 10^{-15}\mathrm{m}$ – classical electron (Thompson) radius, ρ - scattering length density.

The absorbtion term β is positive and for X–rays is related to the linear mass adsorption coefficient μ for the energies far from X–ray threshold:

$$\beta = \frac{\mu}{4\pi}\lambda \tag{4.4}$$

For neutrons imaginary part β is zero except for few elements (Gd, Sm, B, Cd) where nuclear resonance increases absorption. The magnitudes of $\delta(\lambda)$ and $\beta(\lambda)$ for Cu Kα radiation and materials used are on the order of 10^{-6} and 10^{-8}, respectively. In case of neutrons: $\delta(\lambda) \approx 10^{-6}$ and $\beta(\lambda) = 0$.

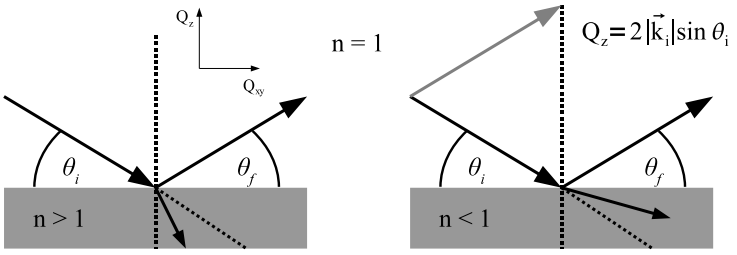

Figure 4.1: Schematic of an incident beam of visible light (left) and X–ray or neutron beam (right) on a flat interface between air (n=1) and material with an optical refractive index n. An incident angle θ_i with respect to the interface, together with refracted portion of the beam θ' (angle is not indicated, shown only refracted beam) and radiation reflected at an angle θ_f are shown.

Well known from the optics Snell's law [Born1999] holds also for X–rays and neutrons. In Fig. 4.1 is shown difference between refraction of visible light (left) and X–rays or neutrons (right) in matter. At the boundary between air and the medium, Snell's law for incident angle θ_i defined as the angle between the incident ray and the surface, can written as:

$$\cos(\theta_\mathrm{i}) = n\cos(\theta') \tag{4.5}$$

where θ' is the angle between the sample surface and the refracted beam. Since in most of the cases $n < 1$, the X–rays and neutrons are refracted away from the normal to the surface when they enter the matter (cf. Fig. 4.1, right).

By radiation the surface below a certain critical incident angle ($\theta_i = \theta_c$) total external reflection occurs ($\theta' = 0$) at small grazing angles (fraction of a degree) and only an evanescent wave propagates along the interface. Above the critical angle (which depends on sample composition) both, X–rays and neutrons penetrate inside the film. The penetration depth rapidly increases for $\theta_i > \theta_c$ and is limited only by absorption β of the material [Tolan1999].

The reflectivity of an incident beam on an infinitely sharp interface is defined as the ratio of the reflected to incident beam energies (intensities) for each θ. On increasing the incident angle the reflectivity is unity and drops rapidly on further increase ($\theta > \theta_c$). The absorption β is significant only around critical angle, resulting in an rounding of the reflectivity curve. When the absorption can be neglected ($n = 1 - \delta$), the critical angle θ_c can be written as:

$$cos(\theta_c) = 1 - \delta \tag{4.6}$$

using $1 - \frac{\theta_c^2}{2}$ expansion for the cosine, one obtains:

$$\theta_c = \sqrt{2\delta} \tag{4.7}$$

Thus, the density of the material can be determined from the critical angle:

$$\text{for X} - \text{rays}: \ \theta_c = \frac{\sqrt{2\pi\rho_e r_e}}{k} \tag{4.8}$$

$$\text{for neutrons}: \ \theta_c = \frac{\sqrt{4\pi\rho}}{k} \tag{4.9}$$

where $k = \frac{2\pi}{\lambda}$ is the wave number. Typical values of θ_c for X–ray and neutron radiation with wavelengths λ=0.15–0.45 nm are θ_c=0.1–0.5^0 [Biesalski2002]. In the case of Cu K_α radiation, the critical angle θ_c is 0.22^0 for bulk silicon, 0.42^0 for nickel, and 0.57^0 for gold.

Measured reflectivity is often characterized by parameter Q_z corresponding to vertical scattering vector, so–called momentum or wave vector transfer (cf. Fig. 4.1, right). The momentum transfer is given by [Daillant2009]:

$$|\overrightarrow{Q_z}| = |\overrightarrow{k_f} - \overrightarrow{k_i}| = \frac{2\pi}{\lambda} sin(\theta_f) + \frac{2\pi}{\lambda} sin(\theta_i) = \frac{2\pi}{\lambda}(sin\theta_f + sin\theta_i)$$

Variation of the incident angle can be achieved either by changing θ_i or by tilting the surface. In case of θ_f=θ_i, the beam reflected from the surface is called specular (wave vectors k_i and k_f define the scattering plane, which is perpendicular to the surface of the material). Specular or mirror like reflection yields averaged information in the direction perpendicular to the surface of the film, off–specular diffuse reflection ($\theta_i \neq \theta_f$) is sensitive to the lateral structure of rough interfaces. To gain information about density profiles, specular set–up was chosen. Thus, for $\theta_f = \theta_i$:

$$Q_z = \frac{4\pi}{\lambda}\sin(\theta_i) \tag{4.10}$$

where k_i and k_f are the incoming and outgoing wave vectors, respectively.

4.1.2 Reflection from Ideally Smooth & Rough Interfaces

Specular reflection from an ideally smooth interface can be described using classical optical theory (Fresnel equations). The Fresnel reflectivity R_F from an ideally smooth surface is given by [Daillant2009]:

$$R_F(Q_z) = \left| \frac{Q_z - \sqrt{Q_z^2 - Q_c^2 + 2i\,(2k)^2\beta}}{Q_z + \sqrt{Q_z^2 - Q_c^2 + 2i\,(2k)^2\beta}} \right|^2 \tag{4.11}$$

where Q_c is the critical value of momentum transfer for total reflection:

$$Q_c = \frac{4\pi}{\lambda}\sqrt{1-\cos^2(\theta_c)} \tag{4.12}$$

For angles of incidence ($\theta_i > \theta_c$) the Fresnel reflectivity decreases rapidly and for $\theta_i > 3\,\theta_c$ and neglectful absorption it may be well approximated by:

$$R_F(Q_z) \approx \left(\frac{Q_c}{2Q_z}\right)^4 \propto \frac{1}{Q_z^4} \tag{4.13}$$

This shows that above 3 critical angles reflected intensity decreases like $1/Q_z^4$ on increasing the Q_z. To record the reflected intensity over several orders of magnitude, highly intensive X–ray and neutron sources and detectors with low noise are needed.

In reality, interfaces between two media are not mathematically sharp, but rough on atomic or molecular level (order of magnitude of nm), see Fig. 4.2. Here a rough surface with the mean height z_j and fluctuations $z(x, y)$ around this value is shown. For an ideally smooth interface, the change of electron density takes place abruptly, i.e. constant index of refraction n_j jumps to another constant value n_{j+1} at the boundary between layer j and $j + 1$. Therefore, profile of the electron (or scattering length) density perpendicular to the surface is just a step function. For a rough surface this sharp step is replaced by a continuous variation of the refractive index, i.e. by continuous electron density. The roughness σ of a real surface can be described by normalized gaussian distribution for the gradient of the electron density perpendicular to the surface [Tolan1999]:

$$\rho_e'(z) = \frac{1}{\sigma\sqrt{2\pi}}\, e^{-\frac{z^2}{2\sigma^2}} \tag{4.14}$$

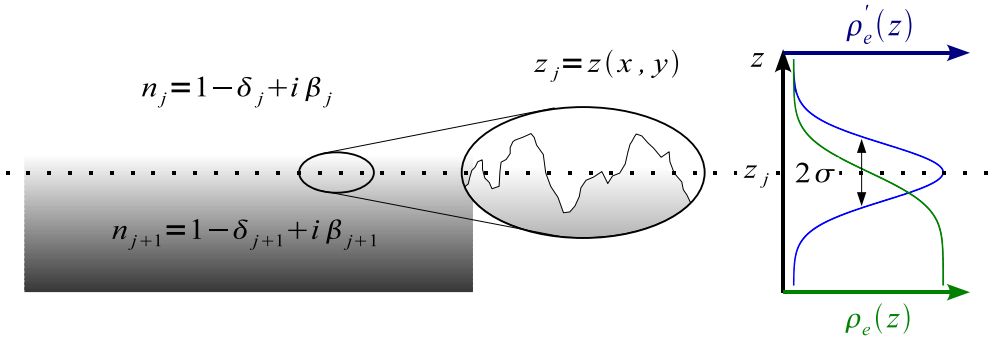

Figure 4.2: Schematic of rough interface with the mean height z_j and fluctuations $z(x, y)$ around this value. Surface roughness σ, electron density profile ρ_e and its gradient are shown.

The measured reflectivity R can be described as the Fresnel reflectivity R_F of an infinitely sharp interface modulated by interference effects from a thin surface layer [Als-Nielsen1985]. The deviation of the measured reflectivity from the Fresnel reflectivity gives information about the electron (scattering length) density profile perpendicular to the interface. Below critical value of momentum transfer for total reflection Q_c, reflectivity is unity and

reflectivity profile contains no structural information about vertical properties of the film. The interference between the the rays reflected from the top and the bottom of the film surfaces (in a simple case) results in interference fringes, which are angle dependent. In Fig. 4.3 the data show finite–size fringes that arise due to the density changes at the film/air and film/substrate interfaces (normal to the sample surface), where constructive interference results in intensity maxima. The periodicity in Q_z of these intensity oscillations in the reflectivity, so-called Kiessig–fringes is related to the thickness of the film l and can be estimated for large Q_z, i.e. for $Q_z > 3Q_c$ using

$$l = \frac{2\pi}{\Delta Q_z} \tag{4.15}$$

However, higher accuracy for the thickness as well as density and roughness can be obtained by fitting the experimental reflectivity curve. Fitting analysis is discussed in details below (cf. section 5.1). An example of reflectivity data from real surface normalized to the Fresnel reflectivity is shown in Fig. 4.4 (here features of the reflectivity curve become visible).

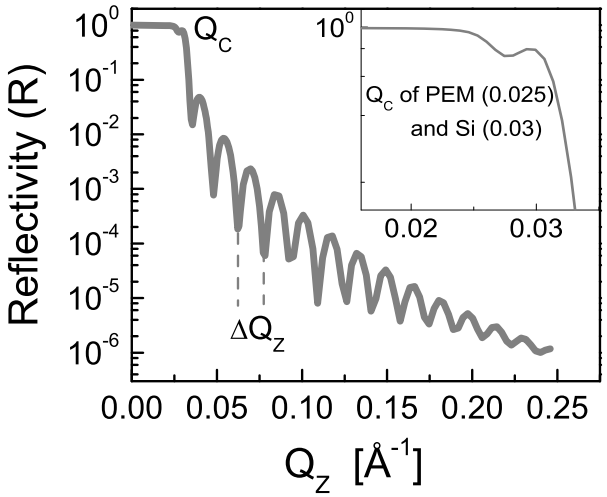

Figure 4.3: Modeled X–ray reflectivity of a polyelectrolyte multilayer adsorbed on silicon substrate. The film consists of PAH/PSS layers adsorbed on PEI (in total 10 BL) at room temperature with 1 mol/L NaCl and measured at room conditions. As one can see, the reflectivity decays over several orders of magnitude for $Q_z > Q_c$, where Q_c is a property of the material. Note that two critical angles (for thicker films with $\beta > 0$) can be observed.

Influence of surface roughness on reflectivity signal is shown in Fig. 4.6, where the amplitude of the oscillation decay on increase of Q_z. The electron density profiles of the PEMs (see Fig. 4.5, 4.7) have been determined from fits to the measured reflectivity curves. As one can see, film/air interface is smoothed by the surface roughness (Fig. 4.7). The neutron reflectivity measurements and corresponding scattering length density profiles can be presented in much the same way.

Reflectivity is an indirect method. Direct inversion of the data is given by analytical kinematic approximation, based on the Born approximation [Als-Nielsen1985] that doesn't take into account the effects around critical angle (absorption and refraction). The intensity of specular reflected radiation and the density profile are related by a Fourier transform of the first derivative of the electron (scattering length) density in the direction perpendicular to the interface, therefore detailed information about the interface and the substrate can be

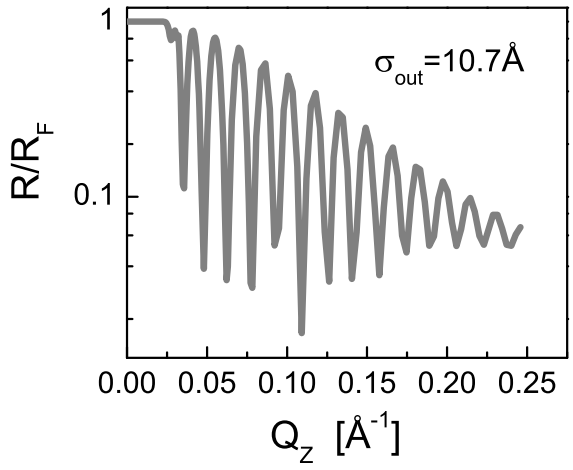

Figure 4.4: Normalized X–ray reflectivity (R/R_F) is plotted against Q_z. To make the features of the reflectivity curve shown in Fig. 4.3 more evident, $R(Q_z)$ is divided by $R_F(Q_z)$. The corresponding electron density profile is shown in Fig. 4.5.

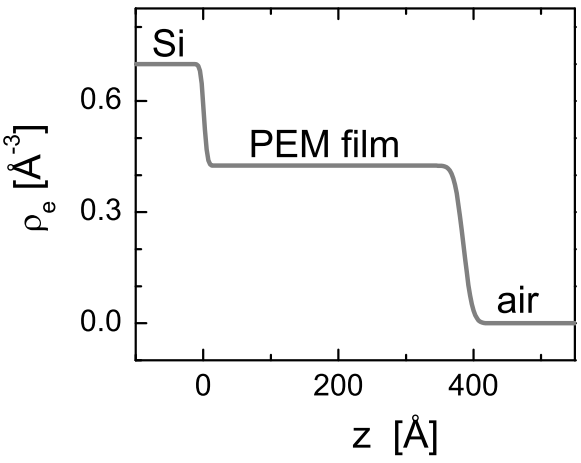

Figure 4.5: The electron density profile corresponding to the reflectivity in Fig. 4.4 is plotted against z–axis. Here left to right: electron density of silicon, polyelectrolyte multilayer film and air. Effect of surface roughness can be seen in Fig. 4.6, 4.7.

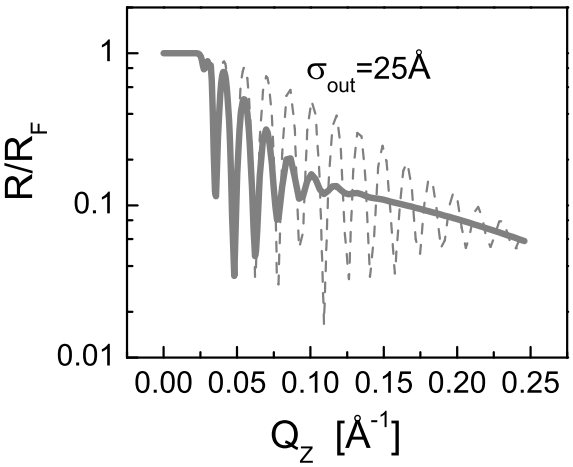

Figure 4.6: Normalized X–ray reflectivity with increased film/air roughness (σ_{out} =25 Å in comparison with 10.7 Å in Fig. 4.4, shown by dashed line here). The corresponding electron density profiles are shown in Fig. 4.7.

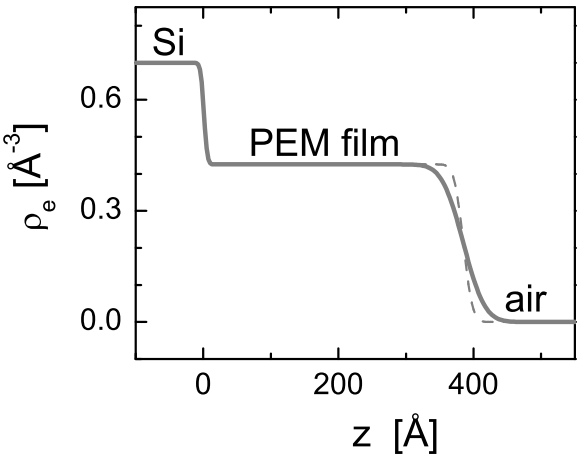

Figure 4.7: The electron density profiles corresponding to reflectivities in Fig. 4.6 are plotted against z–axis. ED profile of interface with lower roughness is shown by dashed line. Left to right: silicon, PEM with adjacent film/air interface.

obtained. Above 3 critical angles of total external reflection, $\theta_i \gg \theta_c$, the reflectivity R is

proportional to the absolute square of the Fourier transform of the density gradient:

$$\text{for X} - \text{rays}: \quad \frac{\mathrm{R}}{\mathrm{R_F}} = \left| \frac{1}{\rho_{e,\,\mathrm{sub}}} \int \rho'_e(z)\, e^{iQ_z\, z} dz \right|^2 \tag{4.16}$$

$$\text{for neutrons}: \quad \frac{\mathrm{R}}{\mathrm{R_F}} = \left| \frac{1}{\rho_{\mathrm{sub}}} \int \rho'(z)\, e^{iQ_z\, z} dz \right|^2 \tag{4.17}$$

where $\rho_{\mathrm{e,\,sub}}$ is the electron density and ρ_{sub} is the scattering length density of the substrate, $\rho'_e(z)$ is the gradient of the electron density ($\rho'(z)$ is the gradient of the scattering length density) along the surface normal.

The above expressions are known as Master formulas and describe the reflectivity of a given density profile in the kinematic approximation. The kinematic approximation to specular reflectivity is very useful for understanding X–ray and neutron reflectivity data. With above given analytical equations, it is possible to find correlations between properties of the measured reflectivity (peak height and periodicity of oscillations) and multilayer properties (layer thickness, water content and internal roughness), see chapter Data analysis, section 5.1.2. However, kinematical theory is an approximation that breaks down at small angles for systems with large density variations [Pedersen1994]. Therefore, dynamical theories analogous to methods in optics are widely used for data analysis. The exact dynamical theory is usually employed in the form derived by Parratt [Parratt1954] that takes into account multiple reflection effects, if the sample has more than one interface. A comparison of different methods for X–ray and neutron specular reflectivity data analysis is presented in [Hamley1994], [van der Lee2007]. The details of analysis employed in this study can be found in chapter 5. Here only a brief description of the theory of reflection is presented, since it has been covered extensively in the literature [Tolan1999], [Daillant2009], where also the derivation of the presented formulas can be found.

4.1.3 Refractivity Set–up

During the measurements sample is illuminated by an incident beam striking the sample surface under a define angle of incidence θ_i. After interaction with the sample, the reflected beam intensity is recorded. In specular geometry employed in this study (θ_f=θ_i), reflectivity (ratio of the reflected to incident intensities) is measured as function of the θ angle and is characterized by momentum transfer $\mathrm{Q_z}$ according to eq. 4.10. The measurement can be done by varying either the angle of incidence θ_i at constant wavelength or by measuring the reflectivity at constant θ_i and varying wavelength. In our case, incident angle is varied and intensity of the reflected beam is measured as a function of 2θ, where 2θ is the angular position of the detector measured with respect to the incident beam direction. Both θ_i and the exit angle $\theta_f = 2\theta - \theta_i$ vary simultaneously by the same amount.

X–ray reflectivity is measured with Seifert XRD 3003 TT diffractometer (with wavelength of 1.54 Å), which is used as reflectometer in this case (Seifert, now GE Inspection Technologies, Ahrensburg, Germany). Neutron reflectivity measurements are carried out on the V6 refractometer (with wavelength of 4.66 Å) in the neutron guide hall NL 4 at the Helmholtz Centre for Materials and Energy, former Hahn-Meitner-Institute (HMI), Berlin, Germany. Owing to the rapid fall–off in intensity with increasing angle (cf. eq. 4.10, 4.13), the available wave vector transfer $\mathrm{Q_z}$ is small. The X–rays provide better resolution at higher

angles (wider Q_z range) in comparison with neutrons (the neutron flux is about 3 orders of magnitude smaller than for X–rays). Fig. 4.8 shows schematically the experimental X–ray reflectivity equipment, where both the X–ray tube and the scintillation detector (that measures ionizing radiation) are mounted on the goniometer arms, as well as metallic slits, which are used to shape the beam. In case of neutrons, the angle of incidence is varied by precise tilting of the sample surface relative to the fixed collimated neutron beam (cf. Fig. 4.9). For neutron detection ^{3}He isotope is used. In both cases, monochromatic and collimated beam of a wavelength λ irradiates a sample at an angle θ and intensity of the beam reflected from the surface is measured. After subtraction of the off–specular background, these data are fitted to obtain profile of electron density (in case of X–rays) or scattering length density (in case of neutrons).

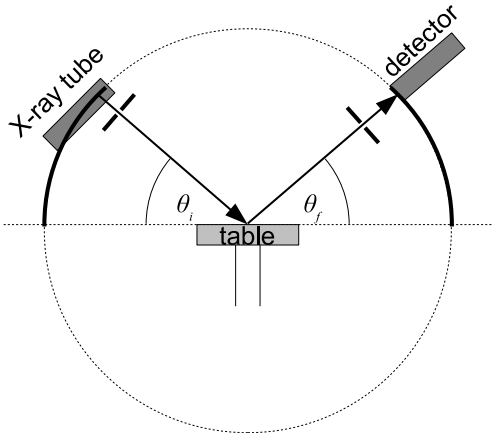

Figure 4.8: Schematic set–up of an X–ray reflectometer. Here source (X–ray tube), slits and detector are mounted on the movable goniometer arms.

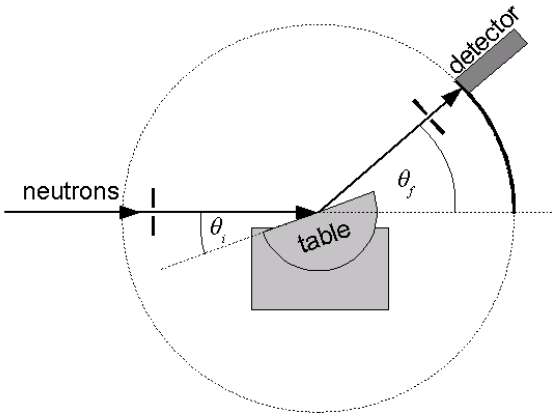

Figure 4.9: Schematic set–up of an neutron reflectometer. Here the angle of incidence is varied by tilting of the sample surface relative to the fixed neutron beam. Slits and detector are indicated.

Small angle reflectivity technique is very sensitive to any change in a layered structure; on the other hand, the alignment of the sample is critical to the quality of the data. Note that sample size should be taken into account to avoid large errors due to footprint, which is responsible for deviation of measured reflectivity for $\theta < \theta_c$ from unity. For small angles the illuminated area is bigger than a sample. To minimize this effect one can use bigger samples and/or smaller beam size, which is regulated by slit system, however counting time in latter case should be increased. The required angular resolution depends on the total thickness of the film. The thickness is often determined with a precision better than 1 Å for measurements exhibiting interference fringes in a bigger angular range. A typical data acquisition time for X–ray reflectivity measurement is 4 to 8 hours and about 8 hours for neutron measurements. The reproducibility of reflectivity data is obtained by repeating the measurement of the first fringes. In all cases, the simulated reflectivity is convoluted with the angular divergence of the respective reflectometer (for X–rays: 0.012^0; for neutrons: 0.017^0).

4.2 UV-Vis Absorption Spectroscopy

Quantitative analysis by means of spectroscopy has been widely used for more than a century and still remains attractive due to its simplicity. Absorption spectroscopy measures amount of light on a particular wavelength (colour) absorbed by homogeneous or complex substance of solid, liquid or gas. This type of experiment does not measure the amount of light that might be scattered in the sample, the emission properties of the sample, nor the reflection losses at the surfaces of the sample, which can be compensated by background correction measurements.

In this thesis, optical absorption measurements have been performed using double beam Lambda 900 spectrometer (Perkin-Elmer, Rodgau, Germany), where deuterium and halogen lamps are used as a source for ultraviolet (UV) and visible light (Vis), respectively. The wavelength region from 200 to 800 nm is chosen, since the investigated PSS polyelectrolyte solution exhibits UV absorption at approximately $\lambda \approx 260$ nm (due to the benzene rings) and at $\lambda \approx 400$ nm for spherical Ag colloids. Intensity of the transmitted light is measured as a function of wavelength λ and compared to the intensity of the reference at the same λ (the sample and reference are measured simultaneously), resulting in absorbance quantity A as a function of λ for a particular compound (absorption spectrum). A photomultiplier used as a detector in UV-Vis range, where a rotating mirror (chopper) allows to detect alternately the beam from the reference or the sample. Samples and references are measured within special cuvettes which are optically polished on the light path and therefore reduce reflection from the cuvette/air interface [Schmidt2005]. Mostly used cuvettes are made of polystyrene and borosilicate. However, presented measurements have been done with quartz glass cells which are transparent for the used UV-range.

4.2.1 Interaction of Light with Matter

When light interacts with a matter (Fig. 4.10), it can be absorbed, transmitted, reflected, scattered or can excite fluorescence (absorbed photons are re-emitted, this case will not be discussed here).

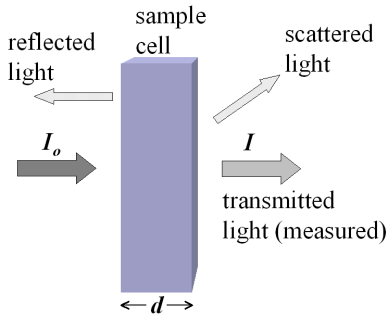

Figure 4.10: Schematic of the absorption measurement. Attenuation of the incident beam intensity I_0 due to various mechanisms (absorption, reflection and scattering) is indicated.

In case of negligible reflection and scattering, intensity of the light decreases as a result of energy transformation into internal energy of the absorber. Since ultraviolet and visible

light are energetic enough (1–5 eV) to promote outer electrons to higher energy levels, UV-Vis radiation corresponds to the electronic excitation and usually applied to molecules or inorganic complexes in a solution. The wavelength at which the incident photon is absorbed is determined by the separation of the energy levels of the different substances present in the sample. It is the selectivity of absorbance spectroscopy - the ability to generate photon (light) sources that are absorbed by only some of the components in a sample - that gives absorbance spectroscopy much of its utility [Hollas2004]. The plot of amount of radiation absorbed versus wavelength for a particular compound is referred to as the absorption spectrum. The absorption spectrum normalized to the concentration is a characteristic of the analyte compound.

4.2.2 Beer-Lambert Law

It was empirically found that the absorption contribution over the path length d in the studied medium yields the well known Beer–Lambert law [Drake2006]:

$$I(\lambda) = I_0(\lambda)e^{-\gamma(\lambda)\cdot d} \tag{4.18}$$

where the measured intensity I of the light transmitted through the sample is related to the incident intensity I_0 and an exponential damping factor. This factor is the product of extinction coefficient γ (or absorption coefficient in case of negligible reflection and scattering for small nanoparticles) and the pathlength through the medium d. This is valid for highly monochromatic and collimated (parallel) radiation in optically homogenous (isotropic) media [Sommer1989].

The absorbance of the medium, defined as decimal logarithm of the ratio between the incident and transmitted intensities, is directly proportional to the properties of the material through which the light is passing:

$$A \equiv log_{10}\left(\frac{I_0}{I}\right) \tag{4.19}$$

However, the decadic absorbance is turned out to be more convenient for analytical practice [Sommer1989]:

$$A = \frac{1}{ln(10)} \cdot \gamma \cdot d \tag{4.20}$$

For a solution of a molar concentration c extinction coefficient γ can be written as,

$$\gamma = \gamma_c \cdot c \tag{4.21}$$

where c is the concentration of the absorbing species in the material (measured in moles per liter) and γ_c is the molar absorption or molar extinction coefficient ($\mathrm{L \cdot mol^{-1} \cdot cm^{-1}}$). Molar extinction is a fundamental molecular property in a given solvent at a particular temperature and pressure, usually in optics denoted by ε and renamed here to avoid confusion, since ε in this thesis is reserved for the dielectric constant.

4.2.3 Optical Properties of Metallic Nanoparticles

One application of UV-Vis spectroscopy is measurement of the imaginary part of the refractive index that provide a useful tool for a wide range of samples including metallic nanoparticles. In contrast to the bulk matter, metallic nanoparticles exhibit strong

ultraviolet–visible absorption band in the near UV–Vis region as a result of interaction of light with confined mobile electrons. An example for the silver can be seen in Fig. 4.11, where pronounced absorption peak (red curve) corresponds to the Ag spherical nanoparticles and wide absorption band (black curve) for bulk silver.

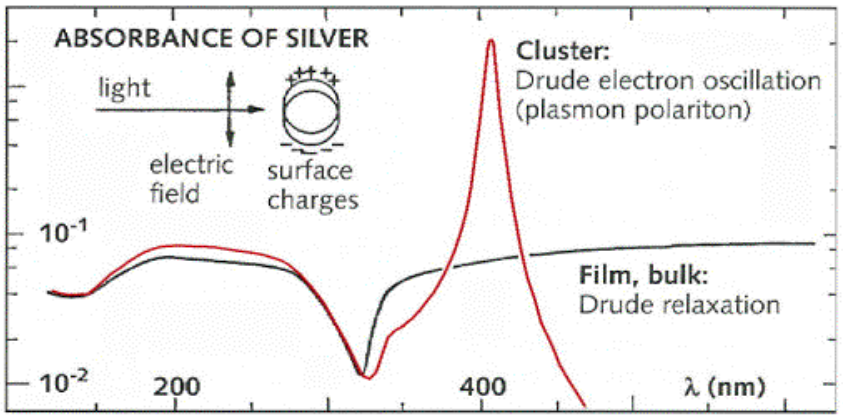

Figure 4.11: Absorbance of spherical Ag nanoparticle (red curve) and bulk (black curve). Polarization of the nanoparticles takes place at the particle surface under influence of the electric field. The picture is adopted from U. Kreibig and M. Vollmer "Optical Properties of Metal Clusters" (1995).

Generally, coherent oscillations of the free electrons are driven by the change in electric field of the external electromagnetic field. If the field frequency corresponds to the eigen frequency of the electrons, surface plasmon resonance (SPR) occurs. Localized surface plasmon is an oscillation of mobile electrons in a nanoparticle, whose resonance frequency is the plasma frequency (ω_p) adjusted by the size and shape of the particle. The conductive electrons in a metallic particle act like an oscillating system, whereas in bulk they behave like a relaxation system (the plasma frequency is not excited by light in the bulk [Kreibig1995]). The displacement of the negative charges due to external electric field gives rise to polarization charges (Fig. 4.11, top). The positive charges in the particles assumed to be immobile.

In case of spherical geometry, the polarization of the nanoparticles exhibits dipole properties. Using the boundary conditions at the sphere surface [Kreibig1995], the resulting polarization of the sphere is calculated as a whole due to the external field. The internal field is

$$E_i = E_0 \frac{3\varepsilon_m}{\varepsilon + 2\varepsilon_m} \tag{4.22}$$

where E_0 - amplitude of the electric field, ε_m is the dielectric constant of the embedding (surrounding) medium and ε is the dielectric constant of the particle (which assumed to be the same as that of bulk silver).

The localized SPR in metallic nanospheres can be described in terms of Mie's theory, based on the study of optical properties of gold particles with sizes below the resolution limit of light microscopes [Mie1908]. The Mie theory accounts for the interaction between an electromagnetic wave and a single metallic sphere in a uniform transparent medium. In order to describe composite materials, several effective medium theories have been developed [Kreibig1995]. The main assumption of the theoretical approach for optical response of metal

nanoparticles is based on the small size of the nanoparticles with radius R_p relative to the wavelength of the visible light ($2R_p << \lambda$). This leads to the use of a quasi–static theory: static, with respect to the particle interaction interaction with light, and dynamic, with respect to the dielectric properties of the free electrons in the metallic spheres [Schmitt1999].

Small spherical particles in a static electric field have polarizability α given by the following formula [Kreibig1995]:

$$\alpha = 4\pi\varepsilon_0 R_p^3 \cdot \frac{\varepsilon - \varepsilon_m}{\varepsilon + 2\varepsilon_m} \tag{4.23}$$

The optical properties of metallic clusters differ from those of polarizable organic molecules in two ways: (i) there is no oscillator strength limiting light absorption and (ii) their interaction leads to a change in the absorption properties. The wavelength corresponding to the maximum value of the absorbance (λ_{max}) is determined by the particle properties (dielectric constant ε) and by its local environment (dielectric constant of the surrounding medium ε_m) [Kreibig1995]. For metals, the dielectric function ε is complex quantity and related to refractive index n through the following expression:

$$\varepsilon(\lambda) = \varepsilon_1(\lambda) + i\varepsilon_2(\lambda) = (n + i\kappa)^2 \tag{4.24}$$

where ε_1 and ε_2 are real and imaginary parts of the dielectric function of the metallic clusters, κ is imaginary part of the refractive index.

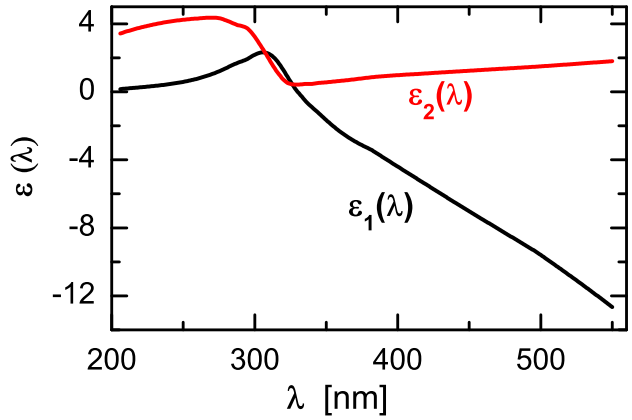

Figure 4.12: Calculated real (ε_1) and imaginary (ε_2) parts of the complex dielectric constant of Ag in UV–Vis part of the spectrum as a function of the wavelength of the incident light.

In optical spectra, excitation of the surface plasmon can be found as the absorption maximum, where the measured extinction coefficient is the imaginary part of the complex refractive index of the material of the nanoparticle. The imaginary part of the refractive index is related to the extinction coefficient γ and therefore to the optical properties of the material (see eq. 4.18):

$$\gamma(\lambda) = \frac{4\pi\kappa}{\lambda} = \frac{1}{d} \cdot ln\frac{I_0}{I} \tag{4.25}$$

As follows from quasi–static assumption, for spherical metal particles surface plasmon resonance is independent of the particle diameter and occurs when α reaches maximum:

$$|\varepsilon + 2\varepsilon_m| = min \tag{4.26}$$

thus

$$(\varepsilon_1 + 2\varepsilon_m)^2 + \varepsilon_2^2 = min \tag{4.27}$$

This means that ε_1 should be negative ($\varepsilon_1 = -2\varepsilon_m$), which guarantees the proper phase relation between field and nanoparticle polarization.

An example for silver can be seen in Fig. 4.12. Here the real part of the complex dielectric function, which goes to negative values at the absorption band and the imaginary part (which is always positive) are plotted against wavelength. Consequently, with a change in the complex dielectric function and therefore in refractive index of the surrounding medium will change the wavelength of the plasmon peak (cf. eq. 4.24). From the resonance condition (formula 4.27) the spectral position of the plasma resonance absorption can be calculated in two ways: first, using the particle polarizability α and comparing to the experimental spectra and second, by introducing an effective dielectric function [Heilmann2003].

If the particles are well separated, i.e. volume fraction of nanoparticles or filling factor $f \ll 1$, and quasi-static approximation is fulfilled, the sample may be replaced formally by an effective medium. An effective medium acts approximately like homogeneous material and can be described by an effective dielectric function of the whole composite sample: $\varepsilon(\lambda) \longrightarrow \varepsilon_{\text{eff}}(\lambda) = \varepsilon_{\text{eff},1}(\lambda) + i\varepsilon_{\text{eff},2}(\lambda)$. However, the formulas for ε_{eff} shown below are commonly applied beyond this latter limit, justified by experiment [Kreibig1995].

In case of interacting neighboring nanoparticles, dielectric function can be written accordingly to an effective medium theory and called Maxwell–Garnett formula (Clausius–Mossotti formula, if applied for atoms):

$$\varepsilon_{\text{eff}} = \varepsilon_m \frac{1 + 2f\Lambda}{1 - f\Lambda} \tag{4.28}$$

where [Kreibig1995]:

$$\Lambda = \frac{1}{\varepsilon_m} \frac{\varepsilon - \varepsilon_m}{\varepsilon + 2\varepsilon_m} = \frac{\alpha}{3\varepsilon_0 \varepsilon_m V} \tag{4.29}$$

with the polarizability α of spherical individuals (cf. eq. 4.23) and volume $V = \frac{4}{3}\pi R_p^3$ for spherical geometry. The filling factor f can be defined as a function of the particle density N_d suggesting spherical particles:

$$f = \frac{4}{3}\pi R_p^3 N_d \tag{4.30}$$

In case of aggregating nanoparticles, Λ in eq. 4.29 can be exchanged by

$$\Lambda = \frac{1}{2} \frac{(\varepsilon - \varepsilon_m)}{(\varepsilon + 2\varepsilon_m)} \left(\frac{1}{1 - 2\left(\frac{R_p}{D}\right)^3 \frac{\varepsilon - \varepsilon_m}{\varepsilon + 2\varepsilon_m}} + \frac{1}{1 + \left(\frac{R_p}{D}\right)^3 \frac{\varepsilon - \varepsilon_m}{\varepsilon + 2\varepsilon_m}} \right) \tag{4.31}$$

for 2–dimensional aggregation (all particles lie within the surface plane), where D is the center to center separation distance between particles (see Fig. 8.14). In [Kreibig1995] one can find a formula for 3–dimensional aggregates.
The imaginary part of the refractive index of interacting particles can be written as:

$$\kappa = \sqrt{-\frac{\varepsilon_{\text{eff},1}}{2} + \frac{\sqrt{\varepsilon_{\text{eff},1}^2 + \varepsilon_{\text{eff},2}^2}}{2}} \tag{4.32}$$

In case of non–interacting particles previous equation can be written in form proposed by Gustav Mie in 1908 [Mie1908]:

$$\kappa = \frac{9}{2} f \varepsilon_m^{3/2} \frac{\varepsilon_2}{(\varepsilon_1 + 2\varepsilon_m)^2 + \varepsilon_2^2} \tag{4.33}$$

where the absorption on the metallic clusters depend on the dielectric constant of the surrounding medium ε_m. Thus, measured extinction (absorption) spectra of nanoparticles can be calculated if dielectric function of the sample is known.

4.3 Atomic Force Microscopy

Atomic force microscopy (AFM), also known as Scanning Force Microscopy (SFM) is a surface imaging technique that provides direct visualization of the structural features down to the atomic scale [Binnig1986]. An image is constructed through the detection of an interaction between the probe and the surface features at small separation distances (cf. Fig. 4.13). Unlike other microscope techniques, AFM is able to record detailed information without any sample pre-treatment and provide imaging either in ambient atmosphere or in liquid environment. Choice of materials that can be investigated is not limited, therefore this technique can be used for soft materials like polymers [Giessibl2003].

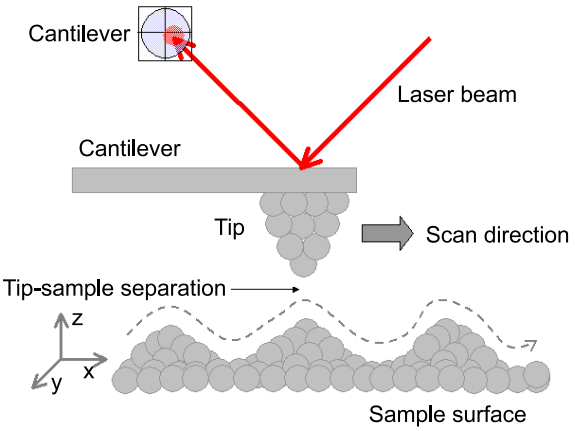

Figure 4.13: Schematic illustration of AFM principle. A very sharp tip attached to micro-cantilever probes the sample surface. An optical system senses the bending of the cantilever and thereby the distance dependent tip-sample interaction force.

AFM has two measures of resolution: in-plane of the measurement or horizontal and out-of-plane (vertical resolution). The in-plane resolution is limited by the geometry of the probe. Therefore, knowledge about geometry of the force–sensing probe is essential for evaluation of a surface image (see section 4.3.2). The vertical resolution is affected by mechanical vibrations, acoustic noise and thermal drift. To avoid external vibrations the measuring head of AFM is placed on an elastic suspension. Nanoscope IIIa Multimode system (Digital Instruments, now Veeco Instruments, Santa Barbara, USA) is used to visualize surface topography of polyelectrolyte multilayered films and metallic nanoparticles in air (ambient conditions).

To obtain images with different dimensions JV scanner is used (scan up to 125 μm laterally and 5 μm vertically). The topographic data obtained in intermittent contact operating mode at the highest possible resolution of 512×512 data points per image. Standard Si cantilevers are used (cantilever length 125 μm, resonance frequency about 300 kHz and spring constant of 40 N/m) with tip curvature radius $<$ 10 nm, either NCH-W (Veeco, Paris, France) or Sting (Mikromasch, Tallinn, Estonia). Image processing and analysis are performed with the Digital Instruments nanoscope software and Scanning Probe Image Processor (Image Metrology, Lingby, Denmark).

4.3.1 Basic Principles

The principle of AFM based on the use of an atomically sharp probe, so–called tip, placed at the free end of a force–sensing cantilever that raster scans across the sample and thereby produce a three-dimentional image of the surface. When tip approaches the surface, it is affected by the intermolecular forces acting between the atoms on the tip apex and the atoms on the sample surface (cf. Fig. 4.13). At tip–sample separations of the order of several tens of Å the major interaction is the van der Waals force and in the presence of thin water layer often found in an ambient enviroment, the interaction is influenced much by capillary and adhesion forces. Assuming that the tip–surface interaction can be described by Lennard-Jones potential [Jean1999], which consists of long-range attractive and short-range repulsive forces, tip–surface separation during the scanning can be presented in a way of probe–surface interaction potential (cf. Fig. 4.14).

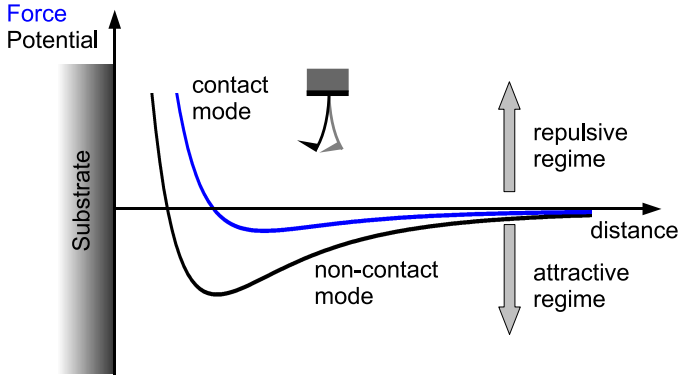

Figure 4.14: Schematic plot of forces involved in AFM as a function of tip–sample separation distance. When tip is far away from the sample the surface forces do not act (flat region). By approaching the surface, tip enters the range of attractive surface forces (net force below the line of zero force is attractive) and is deflected downwards. In contact with the surface net force is attractive and tip deflected upwards.

The potential energy V between the tip and the sample causes a z–component of the tip–sample force: $F = -\partial V/\partial z$. The Lennard–Jones potential has an attractive term $\propto r^{-6}$ originating from the van der Waals interaction and a repulsive term $\propto r^{-12}$ at short ranges [Israelachvili1992]:

$$V_{LJ} = -E_{bond}\left(2\left(\frac{z_{min}}{z}\right)^{6} - \left(\frac{z_{min}}{z}\right)^{12}\right)$$

where E_{bond} is the bonding energy and z_{min} is the distance at the minimum of the potential.

Depending on the tip–sample separation during the scanning, three modes of atomic force microscopy are available: contact and non-contact and intermittent contact (patented by Veeco Instruments as TappingMode and commonly used as tapping mode). The distance regimes are labeled on the Figure 4.14: In case of contact mode forces are repulsive and lie in the range of 10^{-7}–10^{-6} N and separation distance in order of few Å; for non-contact mode force is attractive ($\approx 10^{-12}$ N) with separation about 10–100 Å and intermittent contact mode (periodically experience short range repulsive forces) lies between [Bhushan2004].

Contact mode imaging is the most common method of AFM operation. The force is kept constant using a feedback circuit and tip scans the sample in close contact with the surface. By scanning across the surface, the sharp tip follows the hills and valleys formed by the atoms on the surface. The force between the tip and the sample causes the cantilever to deflect in accordance with Hooke's Law: $F = -kz$, where F is the force, k is the stiffness of the cantilever (spring constant) and z is the distance the cantilever is deflected. Measuring the cantilever deflection, it is possible to evaluate the tip-surface interactive force. Note that deflection should be significantly larger than the deformation of the tip and sample [Giessibl2003]. Deflection of the cantilever is monitored using a laser beam which reflects off the backside of the cantilever and registered by position–senstive four–section photodiode (cf. Fig. 4.13). As the tip traces the various surface features, its upward and downward movement shifts the beam between upper and lower photodiode components, creating voltage difference which is electronically rendered into height information. Because the cantilever-to-detector distance (several cm) is much larger then the cantilever length ($100 - 200$ μm), the optical lever greatly magnifies motions of the tip. This allow to determine small (< 1Å) angular deflection of the cantilever (position of the beam on photodiode), which is proportional to the bending force affecting it [Mironov2004]. The feedback mechanism controls piezoelectric elements that hold the sample and move it in all three axes relative to the tip. The z–movement is used for maintaining the force at the right level, while the x- and y–movements are used for the raster–scanning the tip over the sample. During imaging, the sample is moved by piezo–electric high precision scanner fist along a line in x–direction, then slightly shifted in the y–direction and the same procedure is repeated until 2d–image is obtained. The resulting map of the tip–surface distance at different x-y values of the scan can be used to form 3d–image of the scanned area. With AFM operating in the contact mode, topographic images with a vertical resolution of less than 0.1 nm and a lateral resolution of about 0.2 nm have been obtained [Bhushan2004].

A drawback of the contact mode is vertical and lateral forces that appear on the sample and pull the scanning tip toward the surface. Although these forces are only of the order of 0.1 – 1 nN (most contact mode cantilevers have a spring constant of < 1 N/m), the pressure applied to the sample can easily reach 1000 bar because of the small contact area. This may lead to structure damages, especially on soft surfaces and result in deformed images.

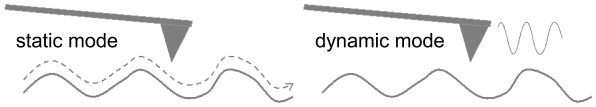

Figure 4.15: AFM operating modes.

To avoid shearing sample deformation that occur in the contact mode and enable detection of the small attractive forces, dynamic or oscillatory modes are introduced (cf. Fig. 4.15).

In dynamic modes, a piezoelement positioned close to the probe is used to excite the cantilever oscillation at its resonant frequency that gives a reasonable amplitude and provides phase information. The resonant frequency of the cantilever depends on its mass and spring constant; stiffer cantilevers have higher resonant frequencies. Approaching the surface, the vibration amplitude of the cantilever decreases, since the interaction force with the surface shifts the resonance frequency. Instead of scanning the sample at constant deflection, the surface is scanned at constant reduction of the oscillation amplitude. The changes in oscillation usually involve a decrease in resonant frequency, a decrease in amplitude, and a phase shift. These parameters can be used to characterize the surface of the sample and can be recorded simultaneously with topographic data. For instance, amplitude modulation provide information about the topography of the sample; phase shifts (between the tip oscillation and the driving force) is used to distinguish different surface materials from each other; frequency modulation can be used to get information about the properties of the sample. In non–contact mode probe–sample separation is kept constant (few nm), i.e. the probe does not contact the sample surface, but oscillates above the adsorbed fluid layer on the surface during scanning. Using a feedback loop to monitor the variation in the amplitude of oscillation the surface topography can be measured. To reduce the tendency for the tip to be pulled down to the surface by attractive forces between the tip and the sample stiff cantilevers are used (spring constants of the order of 10 - 50 N/m). The combination of weak forces affecting feedback circuit and large spring constant of the cantilever result in a small signal, which requires slower scan speeds than either contact mode or intermittent contact mode [Bhushan2004]. Furthermore, the lateral resolution in non–contact mode is limited by the tip–sample separation and is normally lower than in other modes except true non–contact imaging in ultra–high vacuum. Unlike non–contact mode, in intermittent contact mode the AFM tip slightly taps the sample surface. Because the contact time is a small (fraction of its oscillation period), shear forces which can damage soft samples and reduce resolution are eliminated. To minimize contact with the surface stiff crystal silicon cantilevers are used (exerted forces are in the pN range). Analytical descriptions of the intermittent contact (or tapping) mode AFM can be found in [Paulo2002], [Giessibl2003].

Tapping mode enables to provide high resolution and to avoid dragging the tip across the surface. Another advantage of the tapping mode technique is its large operating range that makes the vertical feedback system highly stable, allowing routine reproducible sample measurements. Therefore, tapping mode is preferred to image samples with structures that are weakly bound to the surface or samples that are soft, like polymers and thin films investigated in this thesis.

4.3.2 Tip Convolution and Surface Reconstruction

Due to imaging mechanism, an AFM image is a convolution of the surface features and the tip geometry. If neither of them is known, there is no way to find out on an unknown sample if the image is dominated by the surface features or the tip effect. The tip curvature radius determines the size and shape of the in-plane features that can be resolved and its shape (usually pyramidal or conical) determines the geometry of 3d surface features [Sharpe2008]. The true dimensions of features with known geometry can be determined by tip shape deconvolution, which requires knowledge of the tip geometry and its curvature radius. Figures 4.16 and 4.17 illustrate the effect of profile broadening caused by the shape

of the tip under the approximation of an almost spherical objects. When the tip diameter is larger then the distance between the features $2R > d - 2r$, the AFM tip will penetrate into the narrow cavities between them only by ΔH (cf. Fig. 4.17) decreasing their apparent depth and width. In this case, the object broadening value is $(r_c - d/2)$. When the tip is much sharper than the surface features, the height of the feature will be measured correctly and its shape will be broader than the actual by $2(r_c - r)$. However, images collected using a contaminated or damaged tip can be dominated by the geometry of the AFM tip itself (i.e., self–imaging of the tip). To ensure that the tip is good enough for imaging the surface and has a constant shape, reference samples with known surface features are used.

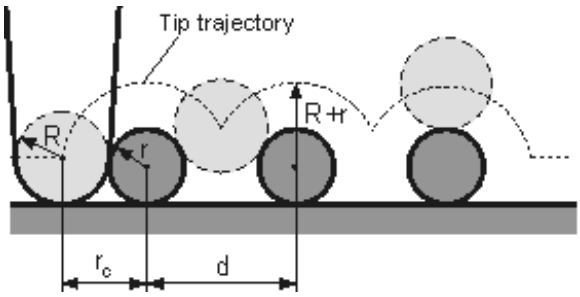

Figure 4.16: Schematic of the spherical particles (with radius r) investigated by the conical AFM tip with radius $R \approx r$. Dotted line represents the tip path.

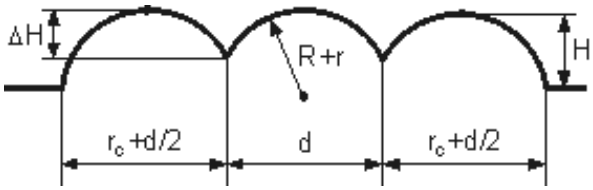

Figure 4.17: Image profile of the spherical objects shown in Fig. 4.16. The pictures are adapted from NT-MDT (www.ntmdt.com).

Since the surface features investigated in this thesis are rather small (about 10 nm), a "NioProbe" standard grating (Micromash, Spain) that consists of random orientated sharp peaks (5–12 nm) is used as a reference sample every time before imaging. In order to exclude tip apex contaminations "TipCheck" sample is used. Using tip modeling (SPIP software) most of the tips with simple geometries can be simulated. The tip characterization algorithm is based on a widely used blind reconstruction algorithm described by J. S. Villarrubia [Villarrubia1994] and P. M. Williams [Williams1996]. This algorithm iterates over all the surface and at each position it tries to refine each tip point according to steepest slope in the direction between the considered tip point and tip apex. Thus, sharper features on the sample surface act as the probe to image and calibrate the AFM tip. Once the tip geometry is known, the sample surface can be reconstructed.

Chapter 5

Data analysis

5.1 Reflectivity Data Analysis

Reflectivity data presented in this thesis were analyzed using the Parratt recursive algorithm [Parratt1954]. The main advantages of the Parratt formalism is its freedom from approximations. In addition, it takes into account the absorption, and can deal with an infinite number of layers [Zabel1994].

5.1.1 Dynamic Approximation (Parratt Algorithm)

The electron (or scattering length) density profile along the z–direction of multilayered system can be described by the so–called box model that may be represented by a series of parallel, homogeneous layers, each having a uniform density. Each layer (slab) is characterized by a electron or scattering length density (represented by ρ_e or ρ, respectively), thickness l, interfacial roughness σ_{int} and outer roughness σ_{out}, which are used to calculate a modeled reflectivity profile using the Parratt dynamical formalism.

The calculated reflectivity $\mathrm{R_{j,\,fit}}$ is compared to the measured curve $\mathrm{R_{j,\,meas}}$ and the quality of the fit is assessed by using χ^2 in the least–squares method:

$$\chi^2 = \frac{1}{\mathrm{J}} \sum_{\mathrm{j}=1}^{\mathrm{J}} (\mathrm{R_{j,\,meas}} - \mathrm{R_{j,\,fit}})^2 \tag{5.1}$$

A minimization of the deviations from the actual data is then achieved by variation of the individual parameters like thickness, electron density and roughness. Variation in the parameters of the constructed profile leads to a change in the calculated reflection, which is usually named fit. Important to note, that for the fitting of the model profiles to the data one needs a good initial guess for the density profile, since modeled profile doesn't provide an unique solution. As one can see from the Master formula (eq. 4.16, 4.17) the phase information during reflection on the sample gets lost. Although the characteristic density profile of a sample cannot be determined unambiguously from the reflectivity data, a model of the profile of the system can be created with known parameters. The known parameters could be, for example, the surface roughness or the characteristic density of the blank substrate. The unknown characteristic densities of the layer can be inferred from the bulk densities.

By selective deuteration of the layers, accurate modeling of the composition variation can be achieved. Reflectivity data from multilayer samples consisting of fully protonated layers or samples consisting of big protonated/deuterated blocks (so-called block samples) are typically analyzed using one or two box model. For complex structures, like samples with partially deuterated layers, many box model is used, where parameters of different boxes are coupled.

Mainly, a model for electron (scattering length) density profile that consist of two slabs sandwiched between substrate and air (so–called solid/air interface) is discussed. Each slab is characterized by a constant density throughout its thickness. The density of a slab is smeared out at the slab borders representing interfacial roughness σ. The electron density (ED) or scattering length density (SLD) of the film, denoted by ρ_e and ρ, are determined by fitting the slab model profile by a function based on expectations about film structure, since the density of substrate is given. The data are normalized to the calculated Fresnel reflectivity for the substrate below the critical angle for total external reflection and fitted with a box model using the dynamical formalism of Parratt implemented in self-made software written by Hubert Baltes (1992). In addition to the density profile, the effective footprint and a correction for absorption are fitted to the data. The reflectivity profile calculated from the fitted model is smeared using an empirical model for the instrumental resolution (all data points are convoluted with the resolution of spectrometer). The parameters of the polyelectrolyte multilayer films obtained by fitting reflectivity data are collected in parameter tables.

Molecule	Volume V [Å^3]	Number of electrons N_e	Electron density (ED) ρ_e [Å^{-3}]	Scattering length b [10^{-5} Å]	Scattering length density (SLD) ρ [10^{-6} Å^{-2}]
H_2O	29.98	10	0.334	-1.675	-0.559
D_2O	29.98	10	0.334	19.145	6.386
PSS	200	95	0.473	47.203	2.36
PSS_d	200	95	0.473	120.07	6.004
PAH	97	33	0.340	-0.614	-0.063
Si	20.016	14	0.699	4.149	2.073
PAH + PSS	297	128	0.429	119.46	4.022
PAH + PSS_d	297	128	0.429	46.589	1.569

Table 5.1: List of material constants used to interpret SLD and ED profiles from reflectivity measurements. For polyelectrolytes (PSS, PSS_d, PAH) all quantities are given with respect to one monomer, for bulk silicon (Si) the values are normalized to one atom and for light and heavy water (H_2O and D_2O) to one molecule. Significant difference between scattering length b of hydrogen and deuterium (H_2O and D_2O), PSS and PSS_d leads to high contrast between the compounds.

Analysis and interpretation of the data are made with the parameters presented in Table 5.1. The molecular volume of PAH, $V_{PAH} = 97$ Å^3 given here, is calculated from the standard mass density of the polymer (1 g/cm^3). To the best of our knowledge, there is one more value for $V_{PAH} = 67$ Å^3 reported in the literature [Lösche1998] that is obtained from the dynamic calculations with van der Waals radius. However, this value leads to the much to high polymer density of 1.438 g/cm^3. As one can see, substitution of hydrogen by

deuterium provides contrast enhancement and yields detailed information about the internal structure of the interfaces. The scattering length density of a compound, denoted by ρ is the ratio of the scattering length b and the volume of a molecule V and defined as:

$$\rho = \frac{\sum_i n_{s,\,i}\, b_i}{\sum_i n_{s,\,i}\, V_i} \tag{5.2}$$

where $n_{s,\,i}$ is amount of substance. List of scattering lengths and cross sections can be found on NIST (National Institute of Standards and Technology) web–site. Electron density ρ_e of a compound is simply defined as a number of electrons N_e divided by the volume V of the given molecule:

$$\rho_e = \frac{N_e}{V} \tag{5.3}$$

5.1.2 Kinematic Approximation for Superlattice PEM Structure

While the dynamic optical matrix formalism is exact, the results are not easy to understand. The Bragg peaks that arise in addition to Kiessig fringes (interference pattern caused by a homogeneous thin film) when the reflection from each interface is in phase can be described by kinematic approximation. The period of the Bragg peaks is the measure of the spacing between the deuterated layers in neutron reflectometry. In case of superstructure samples consisting of selectively deuterated PSS layers (cf. Fig. 5.1), the scattering length density (SLD), denoted by ρ can be described as a sum of two contributions (assuming ideally flat interfaces):

$$\rho(\mathrm{z}) = \rho_{\mathrm{p}}(\mathrm{z}) + \rho_{\mathrm{d}}(\mathrm{z}) \tag{5.4}$$

where $\rho_{\mathrm{p}}(\mathrm{z})$ describes a homogenous protonated slab and $\rho_{\mathrm{d}}(\mathrm{z})$ – the additional scattering length density of the deuterated layers.

The average scattering length density of protonated part can be calculated from the volume V and the scattering length b of water molecules and monomeric segments (cf. Table 5.1), respectively:

$$\rho_{\mathrm{p}} = \frac{b_{\mathrm{PSS}} + b_{\mathrm{PAH}} + n_{\mathrm{H_2O}}\, b_{\mathrm{H_2O}}}{V_{\mathrm{PSS}} + V_{\mathrm{PAH}} + n_{\mathrm{H_2O}}\, V_{\mathrm{H_2O}}} \tag{5.5}$$

where $n_{\mathrm{H_2O}}$ is amount of tightly bound light water molecules per PAH/PSS monomer pair. In this study it is assumed that polyelectrolyte multilayer film consists of polyelectrolytes and water molecules only (no voids). Since the adjacent polyelectrolyte layers are not ideally flat on molecular scale, the derivative of ρ can be approximated with an Gaussian distribution [Bronstein2000]:

$$\rho'_{\mathrm{p}}(\mathrm{z}) = \frac{(\rho_{\mathrm{p},\,0} - \rho_{\mathrm{Si}})}{\sigma_{\mathrm{Si}}\sqrt{2\pi}} \cdot \mathrm{e}^{-\dfrac{\mathrm{z}^2}{2\,\sigma_{\mathrm{Si}}^2}} \tag{5.6}$$

Integrating leads to

$$\rho_{\mathrm{p}} = \frac{(\rho_{\mathrm{p},\,0} - \rho_{Si})}{\sigma_{Si}\sqrt{2\pi}} \cdot \int_{-\infty}^{z} e^{-\left(\dfrac{l^2}{2\,\sigma_{Si}^2}\right)}\, dl \tag{5.7}$$

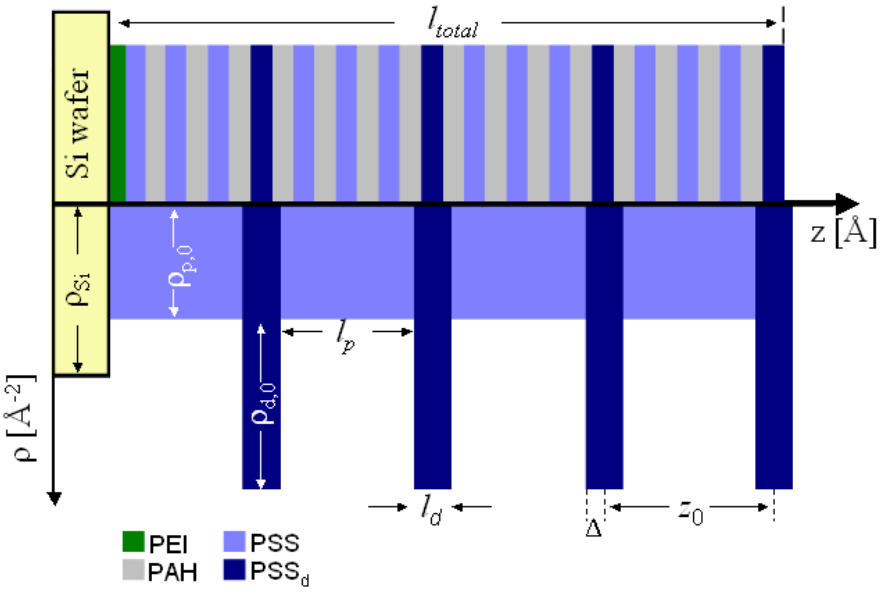

Figure 5.1: Slab model of superstructure sample consisting of 16 BL, where each 4$^{\text{th}}$ PSS layer is deuterated (PSS$_\text{d}$). Upper part shows the multilayer build–up, bottom: the SLD profile - map of the multilayer structure in z–direction (perpendicular to the substrate surface). Here protonated part consist of 3 PAH/PSS bilayers and deuterated - of one PAH/PSS$_\text{d}$ bilayer. Roughness at the interfaces is neglected for clarity.

where ρ_{Si} and σ_{Si} are scattering length density and roughness of the silicon wafer respectively. The standard error function [Bronstein2000] is given by

$$\varphi\left(\frac{z}{\sigma}\right) = \frac{1}{\sigma\sqrt{2\pi}} \cdot \int_{-\infty}^{z} e^{-\left(\frac{l^2}{2\,\sigma^2}\right)}\, dl \tag{5.8}$$

Therefore one can rewrite the parametrization of the protonated part as:

$$\rho_\text{p}(z) = \rho_{Si} + (\rho_{\text{p},0} - \rho_{Si})\,\varphi\left(\frac{z}{\sigma_{Si}}\right) - \rho_{\text{p},0} \cdot \varphi\left(\frac{z - l_{total}}{\sigma_{air}}\right) \tag{5.9}$$

where $l_{total} = 4N \cdot l_\text{d}$ and N is number of repeat units. Since every 4$^{\text{th}}$ PSS layer is deuterated, its thickness is assumed to be 1/4 of the thickness of repeating unit l_d (l_p+l_d=4 l_d). To make the parametrization unambiguous, thickness of the deuterated layer l_d is assumed to be larger than the internal roughness σ_{int}: $l_\text{d} \geq 2\sigma_{int}$.

In analogy to the protonated part, the deuterated part can be written as sum over the standard error function, which defines the internal interfaces between protonated and deuterated parts of the multilayer:

$$\rho_{\text{d,j}}(z) = \rho_{\text{d},0} \sum_{j=1}^{N} \varphi\left(\frac{z - (z_j - \Delta)}{\sigma_{int}}\right) - \varphi\left(\frac{z - (z_j + \Delta)}{\sigma_{int}}\right) \tag{5.10}$$

where $\Delta = \frac{1}{2} l_\text{d}$. Note that in difference to the paper [Gopinadhan2007b], the deuterated layer is parameterized here directly by error function.

Using Master formula (eq. 4.17) the normalized reflectivity can be calculated from the derivative of the scattering length density ρ:

$$\frac{\mathrm{R}}{\mathrm{R_F}} = \left| \frac{1}{\rho_{\mathrm{Si}}} \int \rho'(\mathrm{z})\, \mathrm{e}^{\mathrm{iQ_z\, z}} \mathrm{dz} \right|^2 \tag{5.11}$$

The reflected signal from the protonated part is then:

$$\begin{aligned} \frac{\mathrm{R_{Kiessig}(Q_z)}}{\mathrm{R_F(Q_z)}} &= \left| \frac{1}{\rho_{Si}} \int \rho'_{\mathrm{p}}(z)\, e^{\mathrm{i\, Q_z\, z}} dz \right|^2 = \\ &= \frac{(\rho_{\mathrm{p,0}} - \rho_{Si})^2}{\rho_{Si}^2} e^{-\sigma_{\mathrm{Si}}^2\, \mathrm{Q_z^2}} + \frac{\rho_{\mathrm{p}}^2}{\rho_{Si}^2} e^{-\sigma_{\mathrm{air}}^2 \mathrm{Q_z^2}} - \\ &- 2\, \frac{\rho_{\mathrm{p,0}}(\rho_{\mathrm{p,0}} - \rho_{Si})}{\rho_{Si}^2} e^{-\mathrm{Q_z^2}\, (\sigma_{\mathrm{Si}}^2 + \sigma_{\mathrm{air}}^2)/2}\, \cos(\mathrm{Q_z\, l_{total}}) \end{aligned} \tag{5.12}$$

where the last term describes Kiessig oscillations that yield direct information on the total thickness of the film (cf. eq. 4.15). For deuterated part, using equations 5.8 and 5.10 one can write:

$$\int \rho'_{\mathrm{d}}(z)\, e^{\mathrm{iQ_z\, z}} dz = \frac{\rho_{\mathrm{d,0}}}{\sigma_{int}\sqrt{2\pi}} \left(\sum_{j=1}^{N} k_{1,j} - k_{2,j} \right) \tag{5.13}$$

Here

$$k_{1,j} = \int e^{-\frac{(z - (z_j - \Delta))^2}{\sigma_{int}^2}} e^{\mathrm{iQ_z z}} dz$$

$$k_{2,j} = \int e^{-\frac{(z - (z_j + \Delta))^2}{\sigma_{int}^2}} e^{\mathrm{iQ_z z}} dz$$

Integration leads to:

$$\int \rho'_{\mathrm{d}}(z)\, e^{\mathrm{iQ_z\, z}} dz = \rho_{\mathrm{d,0}} \sum_{j=1}^{N} e^{-\sigma_{\mathrm{int}}^2\, \mathrm{Q_z^2}/2} \left(e^{-\mathrm{iQ_z(z_j - \Delta)}} - e^{-\mathrm{iQ_z(z_j + \Delta)}} \right) \tag{5.14}$$

By simplifying

$$\sum_{j=1}^{N} e^{-\mathrm{iQ_z\, z_j}} \left(e^{-\mathrm{iQ_z \Delta}} - e^{\mathrm{iQ_z \Delta}} \right) = \sum_{j=1}^{N} e^{-\mathrm{iQ_z\, z_j}} \left(-2i\, \sin(\mathrm{Q_z \Delta}) \right) \tag{5.15}$$

and using a serie expansion, one obtains:

$$\begin{aligned} \frac{\mathrm{R(Q_z)}}{\mathrm{R_F(Q_z)}} &= \left| \frac{1}{\rho_{Si}} \int \rho'_{\mathrm{d}}(z)\, e^{\mathrm{iQ_z\, z}} dz \right|^2 = \\ &= 4\, \frac{\rho_{\mathrm{d,0}}^2}{\rho_{Si}^2} e^{-\sigma_{\mathrm{int}}^2 \mathrm{Q_z^2}}\, \sin^2(Q_z \Delta) \frac{\sin^2(Q_z z_0 N/2)}{\sin^2(Q_z z_0/2)} \end{aligned} \tag{5.16}$$

For Bragg condition $\mathrm{Q_z} = (2\pi\,\mathrm{k})/\mathrm{z_0}$, where $z_0 = 2\Delta + l_p$ is the constant distance between the deuterated layers of the superlattice, previous formula yields to:

$$\frac{\mathrm{R_{Bragg}(Q_z,\,k)}}{\mathrm{R_F(Q_z,\,k)}} = 4\,\frac{\rho_{\mathrm{d},0}^2}{\rho_{Si}^2}\,e^{-\left(\frac{2\pi\,\sigma_{\mathrm{int}}\,\mathrm{k}}{\mathrm{z_0}}\right)^2}\,\sin^2\left(\frac{\pi\mathrm{k}}{4}\right)N^2 \tag{5.17}$$

Here k is the order of the Bragg peak ($1^{\mathrm{st}}, 2^{\mathrm{nd}}$ and so on). Since at least two Bragg peaks can be observed in our measurements, the comparison of the reflectivity leads directly to the estimation of internal roughness. By dividing intensity of the first and the second Bragg peaks by each other and for N=4, the kinematic approach yields to:

$$\sigma_{int} = \sqrt{\frac{\mathrm{z_0^2}}{12\pi^2}\,ln\left(2\,\frac{\mathrm{R_{Bragg}(Q_{z,1})}}{\mathrm{R_F(Q_{z,1})}}\,\frac{\mathrm{R_F(Q_{z,2})}}{\mathrm{R_{Bragg}(Q_{z,2})}}\right)} \tag{5.18}$$

Assumptions used in this model: distance between deuterated layers z_0 is constant, as well as internal roughness σ_{int}. Due to these strong assumptions the calculated value for σ_{int} gives only an upper limit for the value that smears out the interfaces between adjacent layers.

Part III

Results

Chapter 6

Immobile Light Water and Proton–Deuterium Exchange in PAH/PSS multilayers

6.1 Introduction

As mentioned in chapter 2, the secondary short–ranged forces between polyelectrolytes play a very important role for physical processes in the studied polyelectrolyte multilayer (PEM) system, when the electrostatic force during the multilayer buildup is decreased in range and amplitude by high salt concentration in the deposition solution. In this chapter, the focus is on the swelling of PEMs prepared from 1 mol/L NaCl solution. To describe the swelling on a molecular scale and to gain a better understanding of the secondary intermolecular forces, the amount of water bound to polyelectrolytes is quantified. Here the term "bound water" is used for water molecules surrounding the non–polar solute (i.e., the polyelectrolyte backbone and some of the functional groups) that form stable hydrogen bonds and remain at 0% relative humidity (r.h.).

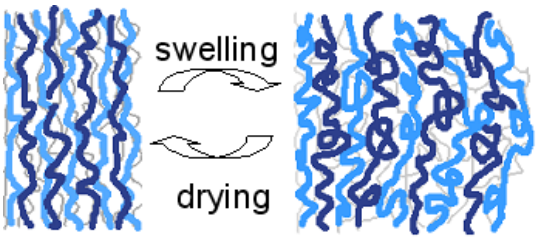

Figure 6.1: Schematic of reversible swelling of polyelectrolyte multilayer film.

It is known that for flat PEMs immersed in water or exposed to 100% r.h. the thickness increases by about 30% through deposition of water molecules into polymer layer (in contrast to the capsules) [Steitz2000], [Ahrens2004]. In Fig. 6.1 reversible swelling and drying (vertical shrinking) of polyelectrolyte multilayer film is schematically shown. Reversibility of the swelling process and therefore, thickness changes as well as determination of tightly bound water are discussed here in terms of length or thickness of the film and density changes. These changes are first estimated from X–ray reflectivity measurements and then compared with complementary neutron reflectivity results.

Neutrons are essential to address these questions because they are sensitive to the scattering length density (SLD) changes of internal interfaces. Using selectively deuterated polyanion layers (PSS_d) the contrast in neutron reflectivity experiments is enhanced and it is possible quantify the amount of incorporated water directly from SLD value along with the thickness changes. Initially the same amount of water in protonated and deuterated parts is assumed, but in some neutron reflectivity studies, more bound water has been observed in deuterated polyanion layers sandwiched between polycation/polyanion bilayers (the quantitative data vary by about a factor of 3 [Decher1997], [Klitzing2006]). Therefore number of water molecules is quantified here separately for protonated and deuterated parts.

To make the data explanation as clear as possible and to have a possibility to determine amount of water in protonated and deuterated parts of the film independently, so–called lego approach is used. Four different film architectures were chosen for experiments presented in this chapter: either ten protonated polyelectrolyte pairs $(PAH/PSS)_{10}$ denoted as p_{10}, ten deuterated – $(PAH/PSS_d)_{10}$ denoted as d_{10}, or of two different blocks, p_5d_5 and d_5p_5, respectively (see Fig. 6.2).

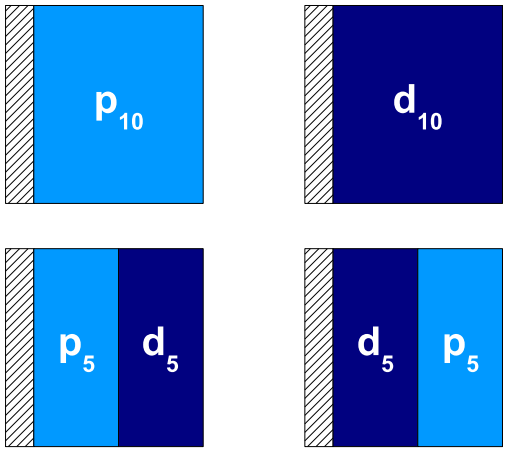

Figure 6.2: Schematic of the block architectures used in the experiments presented in this chapter. Here shaded area indicate silicon substrate, symbols p_N and d_N - protonated and deuterated parts, respectively. N is the number of bilayers (polyelectrolyte pairs).

Block film architecture is selected to obtain as many independent parameters as possible (such as, length and scattering length density of each block, internal and outer roughness, respectively). Thick deuterated blocks (thickness exceeds the roughness of the each adjacent interface) allow to determine the amount of water bound to deuterated layers, without the influence of adjacent protonated layers and to monitor changes in the internal interfaces. The obtained SLD profiles provide insight into the exchange rates of the constituent molecules.

6.2 Swelling of Polyelectrolyte Multilayers

The swelling dynamic of polyelectrolyte multilayer sample consisting of 10 PAH/PSS bilayers (in short form p_{10}) prepared at 25^0 C from 3 mmol/L polyelectrolyte solution with 1 mol/L NaCl salt was investigated by means of X–ray specular reflectivity in enclosed humidity chamber. The degree of swelling was studied as a function of the relative humidity:

first, a reflectivity scan of the sample was recorded at ambient room conditions (21% r.h. in this case), then, the sample was dried in presence of P_2O_5 and investigated by X–rays at 2% r.h.; afterwards, the sample was exposed to the water vapor over a number of saturated salt solutions and water itself. The humidity environment was established using different chemicals listed in Table 6.1 and the system was equilibrated for 2 hours. With the exception of 0% r.h., 21% r.h. and 100% r.h., saturated salt solutions have been used to regulate relative humidity. The corresponding salt solutions (prepared from the ultra pure distilled water) were placed into enclosed chamber in unsaturated condition to obtain an expected relative humidity value at the given temperature [Lide2003]. The humidity inside the chamber as well as temperature was monitored during the X–ray reflectivity measurements and it was made sure it remained constant within 2%.

expected r.h. [%]	measured r.h. [%]	Chemicals
0	2	P_2O_5
8	8	$ZnBr_2$
-	21	ambient conditions
40	35	NaI
58	58	NaBr
75	75	NaCl
100	99	H_2O

Table 6.1: Relative humidity at 20^0C: expected according to the literature and measured.

The reflectivity data obtained during the measurements are Fresnel normalized and shown in Figure 6.3. Here one can observe an interference pattern which can be attributed to the distance of the electron gradients between the Si/PEM and PEM/air interfaces. Obviously the minima of the same order shift to the lower Q_z values with increasing relative humidity, which is indicated by dotted lines. An increase in the frequency of Kiessig fringes yields to swelling of the film. This increase of the thickness can be attributed to the incorporation of water in the PEM. The corresponding electron density profiles are shown in Figure 6.4, where the length of the box (step) corresponds to the thickness of the film and the height – to the electron density of the PAH/PSS film. Intriguing, that the outer roughness of the film is fairly constant (9 – 11 Å) over the relative humidity increase. Reversibility of the swelling was indirectly observed by the sequence of the experiments: the initial measurement in ambient conditions fits into the linear increase of the thickness.

The resulting film thickness as function of relative humidity is shown in Fig. 6.5. Some swelling studies for the same system with slightly different preparation conditions show a non–linear thickness increase [Wong2004], [Kügler2002], using voids conception to explain such behaviour. The presented data show a very good linear thickness increase versus the relative humidity and indicate a dense PEM without voids. Relative thickness increase of the polyelectrolyte film swollen in different humidities is shown in Fig. 6.6. However, the electron density is hardly useful to determine the water content, due to the similar values of PEM and water (see Table 5.1). For example, an electron density of $\rho_e = 0.43 \pm 3\%$ [$Å^{-3}$] yields to 1.5 ± 1.5 H_2O molecules in PEM. Therefore, neutron reflectivity measurements are necessary to determine water amount in the layers.

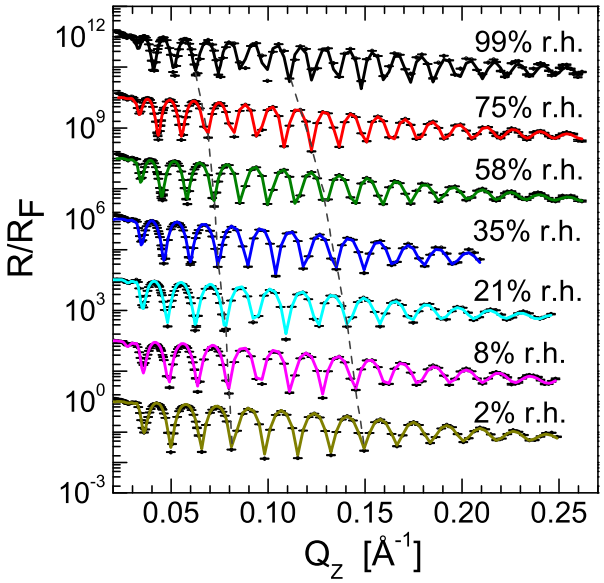

Figure 6.3: Complete set of normalized X-ray reflectivity measurements for p_{10} film prepared at 25^0 C from 3 mmol/L polyelectrolyte solution with 1 mol/L NaCl varying the relative humidity (r.h.). For clarity, data sets have been multiplied by 10^2 for 8% r.h., 10^4 for 21% r.h. and so on. Straight lines are fits; points with error bars are measured data. The humidity inside the chamber was monitored during the measurements. To ensure equilibrium, all measurements were repeated immediately.

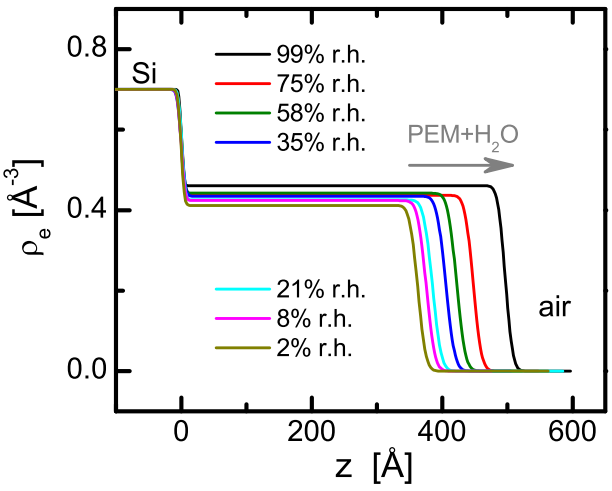

Figure 6.4: The electron density profiles deduced from the fits to measurements in Fig. 6.3. Left to right: silicon, polyelectrolyte film with adjacent film/air interface.

Since no voids are found in the film, one can assume that additionally incorporated water yields to the thickness increase. With this assumption one can quantify the water uptake by

$$\frac{l_{\text{swell}}}{l_{\text{dry}}} = \frac{V_{\text{PAH}} + V_{\text{PSS}} + n_{\text{water, swell}}\, V_{\text{H}_2\text{O}}}{V_{\text{PAH}} + V_{\text{PSS}} + n_{\text{H}_2\text{O, dry}}\, V_{\text{H}_2\text{O}}} \tag{6.1}$$

where the thickness of the dry and the swollen slab are denominated by l_{dry} and l_{swell}. Here $n_{\mathrm{H_2O,\,dry}}$ is amount of tightly bound water found at 0% r.h., $n_{\mathrm{water,\,swell}}$ is a number of water molecules incorporated into the film due to swelling. The observed swelling of about 30% (cf. Fig. 6.6) agrees with a literature value [Steitz2000]. In Figure 6.7 additional amount of water that incorporates into the layer due to swelling in higher relative humidity is shown. Assuming 0 to 3 tightly bound water molecules in a dry state (these values are well known from the literature), one gets additionally 3 to 5 H_2O molecules per PAH/PSS monomer pair during swelling up to 100% r.h.

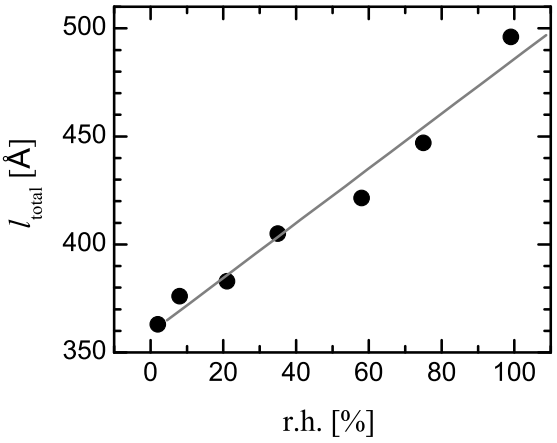

Figure 6.5: Total thickness vs. relative humidity for p_{10} sample deduced from X-ray reflectivity measurements.

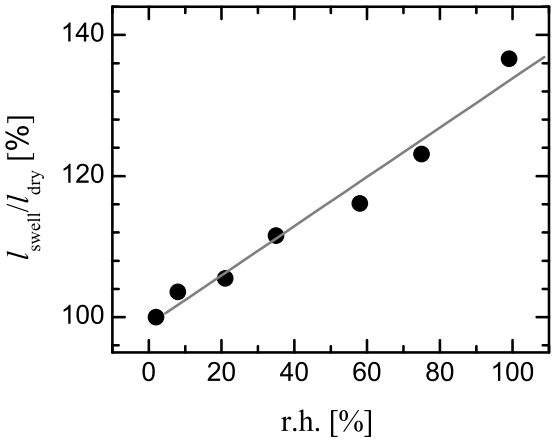

Figure 6.6: Relative thickness over relative humidity for p_{10} sample deduced from X-ray reflectivity measurements.

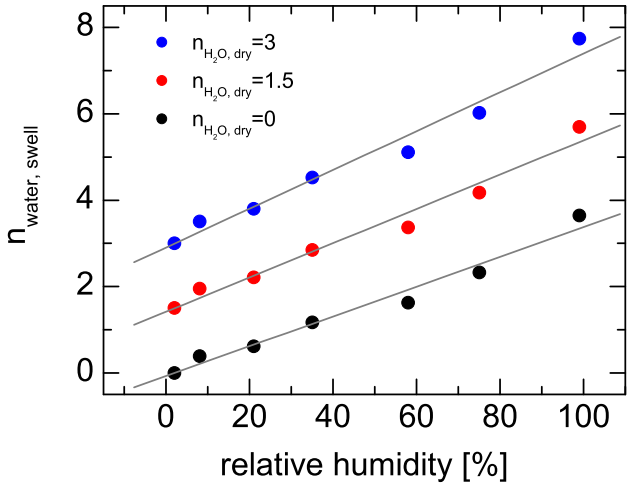

Figure 6.7: Additional number of water molecules $n_{\mathrm{water,\,swell}}$ incorporated into the film due to swelling and calculated for the different number of tightly bound water molecules in a dry state over the relative humidity.

6.3 Determination of Tightly Bound Immobile Water

To determine the amount of tightly bound water we used neutron reflectivity. For the example in the previous paragraph, one gets for neutrons the scattering length density $\rho = 1.28 \cdot 10^{-6} \pm 3\%$ [Å^{-2}] which corresponds to 1.5 ± 0.25 water molecules. This means that the accuracy of this method is an order of magnitude higher, then X-ray reflectivity, if one assume the same error bar for the scattering length density.

It is well known that water amount is inhomogeneous over the polyelectrolyte film [Klitzing2006]. Using neutron reflectivity measurements, one can deduce water amount in protonated and deuterated part of the multilayer film separately and monitor changes of internal interfaces.

Deuterated – protonated d_5p_5 polyelectrolyte film prepared at 15^0 C.

The normalized neutron reflectivity curves of the deuterated–protonated film (d_5p_5) prepared at 15^0 C from 3 mmol/L polyelectrolyte solution with 1 mol/L NaCl salt and measured at different humidity conditions are shown in Fig. 6.8 according to the sequence of the experiment. The samples presented here were first measured in dry conditions, then in swollen state (obtained in saturated water vapour atmosphere) and once more dry. Note that prior to the exposure to 100% relative humidity D_2O or H_2O, the PEM was first immersed for at least 30 min in liquid D_2O or H_2O, respectively to ensure equilibrium.

For reflectivity curves presented in Fig. 6.8 two superimposed interference patterns can be observed. The interference with the shortest periodicity is caused by the largest distance in the sample, which corresponds to the thickness of the whole film. Accordingly, the longer periodicities can be attributed to slabs (blocks) which are about half as thick as the film, and appear due to a superposition of the reflectivities of the protonated and deuterated blocks. For freshly prepared film measured at 0% r.h. (Fig. 6.8, curve 1) the long period is about 0.037 Å^{-1} and the short one half as much, i.e. 0.0185 Å^{-1}. In a next step, the changes of the thickness are measured at 100% r.h. D_2O (Fig. 6.8, curve 2). Here one sees that both periods are shorter, but the interferometric pattern is essentially the same. Increased periodicity of the reflectivity curves (curve 1 to curve 2) indicates swelling of the PEM in heavy water and is shown by dashed lines. Also, compared to the initial measurement at 0% r.h. (curve 1), the 2^{nd} curve shows a larger intensity due to the high scattering length density of deuterium (see Fig. 6.9 for SLD profiles). To make sure that an equilibrium is obtained, the experiment was repeated immediately. The resulting neutron reflectivity curves are identical, and the repeated curve is shown in the Fig. 6.10, curve 2a. On drying the film (curve 3 in Fig. 6.8), the thickness is decreased again and the periods are the same as obtained for the freshly prepared, dried film (curve 1 in Fig. 6.8). Therefore, one can suggest that no additional water is incorporated into the film. However, the contrast remains larger and reversibility of the swelling is not complete.

To show reversibility of the swelling, sample was immersed in liquid H_2O for 6 hours and subsequently dried for 20 hours. By comparing obtained curve 4 and initial curve 1 in Figure 6.8, one can see that they are similar. Thus, the original reflectivity curve can be obtained by immersing the sample in H_2O and by drying the film afterwards. To explain this fact we suggest that dipping the dried film into light water causes a deuterium–proton exchange.

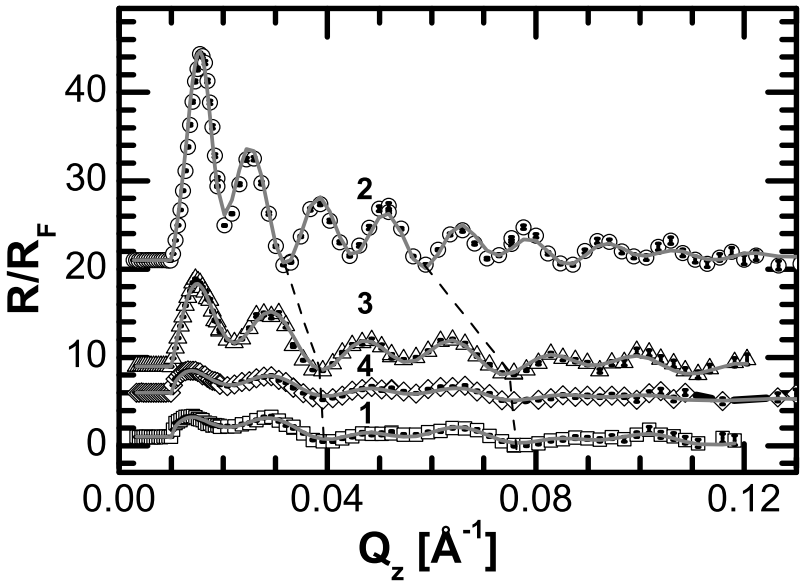

Figure 6.8: Normalized neutron reflectivity curves of d_5p_5 architecture prepared at 15^0 C and 1 mol/L NaCl. Here numbers above the curves represent the sequence of the experiments: (1) 0% r.h., (2) 100% r.h D_2O, (3) 0% r.h directly after drying, (4) 0% r.h after immersing in H_2O and subsequent drying. Straight lines are fits; dashed lines connect interference minima of the same order.

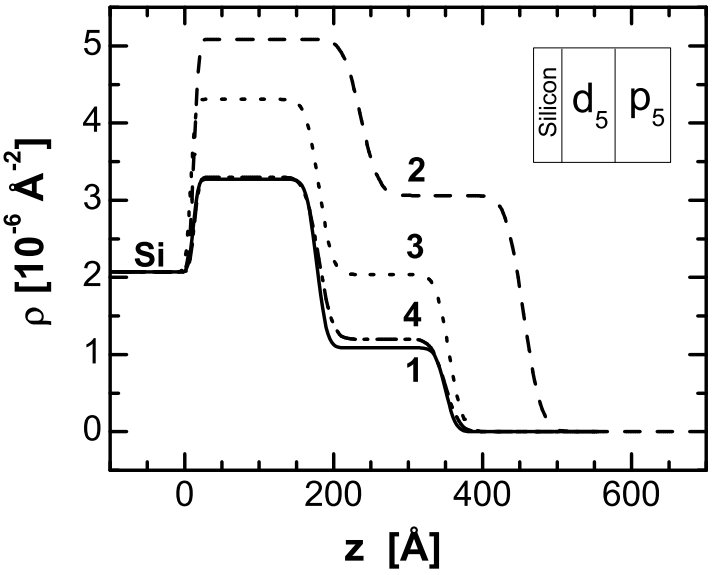

Figure 6.9: The SLD profiles derived from the measurements in Fig. 6.8. Left to right: silicon, d_5 block smeared out by internal roughness and p_5 block with adjacent film/air interface.

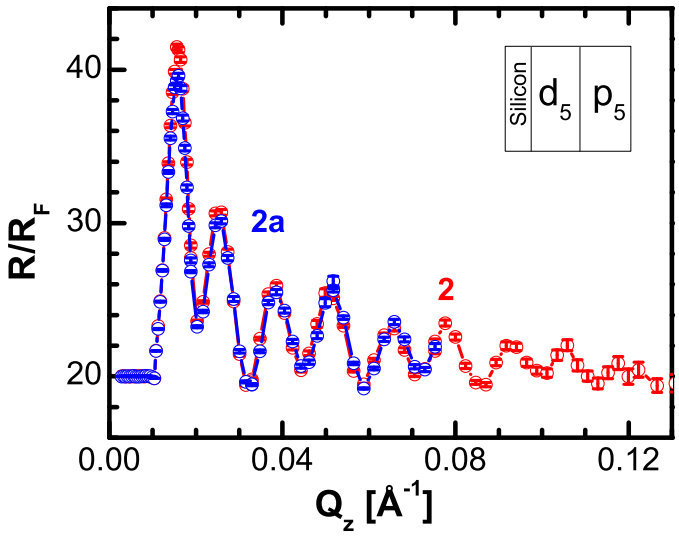

Figure 6.10: Normalized neutron reflectivity measurements of d_5p_5 film prepared at 15^0 C from 1 mol/L NaCl solution: after immersion for 30 min in D_2O - 100% r.h. (curve 2) and reproducibility check (curve 2a). Measurement points are connected for clarity.

To quantify the results, the measurements are fitted with a model consisting of two slabs: one for the deuterated and one for the protonated block (see section 5.1.1 for detailed information about the slab model). The scattering length densities of the substrate (Si) and air are known and given in the table 5.1, sec. 5.1.1. Based on the numerous X–ray reflectivity measurements, the roughness at the film/substrate interface is set to 5 Å. Thus, the obtained reflectivity curves, the respective thickness of the deuterated and protonated slabs (l_d and l_p), the corresponding SLD denoted by ρ_d and ρ_p, and the roughness at the film/air interface σ_{air} are described by five free parameters. Initially, our fits included an additional, sixth parameter: the internal roughness σ_{int} between the protonated and the deuterated block. Yet, it was found that σ_{int} is within 10% identical to σ_{air}. Therefore, condition $\sigma_{int} = \sigma_{air}$ guarantees for no loss of information or quality of the fits.

The corresponding scattering length density profiles of the block architecture in different relative humidity conditions are obtained by fitting normalized reflectivity curves with the slab model and the matrix formalism (dynamic approach). At the beginning of the experiment, the definition of the scattering length density ρ of each block (cf. Table 5.1 and eq. 5.5) is used to calculate $n_{\mathrm{H_2O}}$, i.e., the amount of H_2O molecules per PAH/PSS monomer pair:

$$\rho = \frac{b_\mathrm{PAH} + b_\mathrm{PSS} + n_{\mathrm{H_2O}}\, b_{\mathrm{H_2O}}}{V_\mathrm{PAH} + V_\mathrm{PSS} + n_{\mathrm{H_2O}}\, V_{\mathrm{H_2O}}} \tag{6.2}$$

where b – scattering length of the monomers or water, $V_{\mathrm{H_2O}}$ – volume of the water molecules and V_PAH, V_PSS – molecular volume of the corresponding monomer. Based on the previous equation, the water content $n_{\mathrm{H_2O}}$ at 0% r.h. (cf. Fig. 6.9, curve 1) can be expressed as:

$$n_{\mathrm{H_2O}} = \frac{b_\mathrm{PAH} + b_\mathrm{PSS} - \rho\,(V_\mathrm{PAH} + V_\mathrm{PSS})}{\rho\, V_{\mathrm{H_2O}} - b_{\mathrm{H_2O}}} \tag{6.3}$$

For the initial measurement in dry state $n_{\mathrm{H_2O}}$ is defined as $n_{\mathrm{H_2O,\,dry}}$. Since the volume of H_2O and D_2O molecules is the same (cf. Table 5.1), the amount of water per PAH/PSS

monomer pair in a swollen state $n_{\mathrm{water,\,swell}}$ is then given by the ratio of the length of the swollen and dry slabs, amount of water in dry conditions ($n_{\mathrm{H_2O,\,dry}}$), volume of the water molecules and PAH/PSS monomer:

$$n_{\mathrm{water,\,swell}} = \frac{1}{V_{\mathrm{H_2O}}}\left(\frac{l_{\mathrm{swell}}}{l_{\mathrm{dry}}}(V_{\mathrm{PAH}} + V_{\mathrm{PSS}} + n_{\mathrm{H_2O,\,dry}}\,V_{\mathrm{H_2O}}) - (V_{\mathrm{PAH}} + V_{\mathrm{PSS}})\right) \tag{6.4}$$

While our measurements are performed in 100% r.h. H_2O and 100% r.h. D_2O, a fixed amount of water $n_{\mathrm{water,\,swell}}$ is composed of H_2O and D_2O:

$$n_{\mathrm{water,\,swell}} = m_{\mathrm{H_2O}} + m_{\mathrm{D_2O}} \tag{6.5}$$

After the sample has been dried, the periodicity increases and the height of the peak decreases (cf. Fig. 6.8, curve 3). This observation suggests that loosely bound water, i.e. D_2O, is evaporated. Thus, what remains are basically the tightly bound water molecules which are not exchanged during exposure to liquid D_2O, and we expect an identical or slightly decreased value for $m_{\mathrm{H_2O}}$ for the dried film compared to the value obtained at 100% r.h. D_2O (cf. Table 6.2). Large intensities of the reflectivity curve can be explained either by incorporation of D_2O molecules (but thickness is the same as at 0% r.h. H_2O) or by exchange of protons by deuterium ions in the amino group of PAH monomer (cf. Fig. 6.11).

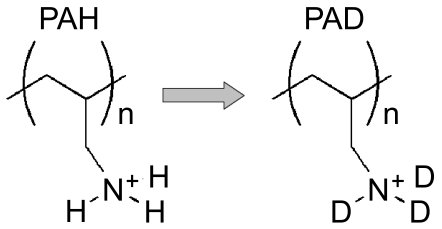

Figure 6.11: Sketch of the PAH – $PAH_{3-i}D_i$ exchange, shown for the case i = 3.

For the freshly prepared film at 0% r.h the parameters for the protonated block are in almost perfect agreement with the values reported previously for identical preparation conditions: the thickness per polycation/polyanion bilayer is $l_{\mathrm{BL,\,p}}$=34.6 Å, and the number of H_2O molecules for a pair of monomers is $n_{\mathrm{H_2O,\,dry}}$=3.4 (expected from the literature: l_{BL}=35±1 Å and $n_{\mathrm{H_2O,\,dry}}$=3.5) [Gopinadhan2007b]. Note that $n_{\mathrm{water,\,swell}}$=$n_{\mathrm{H20,\,dry}}$ for the initial measurement at 0% r.h. The thickness of the deuterated block is slightly smaller: $l_{\mathrm{BL,\,d}}$=33 Å, and the H_2O content is decreased by a factor of 2 ($n_{\mathrm{H_2O,\,dry}}$=1.9). Furthermore, protonated and deuterated blocks swell in a different way: $l_{\mathrm{p,\,100\%\ r.h.}}/l_{\mathrm{p,\,0\%\ r.h.}} = 1.26$ and $l_{\mathrm{d,\,100\%\ r.h.}}/l_{\mathrm{d,\,0\%\ r.h.}} = 1.36$, i.e. film thickness increases by 26% and 36% correspondingly (cf. Table 6.2). The six water molecules per monomer pair as derived from the increase of thickness consist of 4.9 D_2O and 1.1 H_2O molecules per monomer pair. This results in the following expression: $m_{\mathrm{H_2O}}$=1.1 $\leq$ $n_{\mathrm{H_2O,\,dry}}$=1.3 and $m_{\mathrm{D_2O}}$=4.9 and is consistent with $n_{\mathrm{water,\,swell}}$=6. Assuming the polycations in the dried film consist of PAD_3, we obtain $m_{\mathrm{H_2O}}$=1.7, which is higher than the value observed at 100% r.h. D_2O ($m_{\mathrm{H_2O}}$=1.1). This deviation is presumably within error. Finally, the thin film is immersed in H_2O and dried. The thickness of the pristine film is found again, and the deuterium ions and the heavy water molecules are removed.

d_5p_5	0% r.h.	100% r.h. (D_2O) m for PAD_3	back to 0% r.h. no H_2O contact m for PAH_1D_2	back to 0% r.h. after H_2O contact m for PAD_3
d_5p_5	curve 1	curve 2	curve 3	curve 4, Fig. 6.8
protonated block				
l_p [Å]	173.2	218.4≈173.2x1.26	174.6	170.0
$\rho_p[10^{-6}\,Å^{-2}]$	1.02	3.06	2.01	1.14
$l_{BL,\,p}$ [Å]	34.6	43.7	34.9	34.0
$n_{water,\,swell}$	3.4	6.9	3.5	3.1
m_{H_2O}	3.4	2.7	2.6	3.1
m_{D_2O}	0	4.2	0.9	0.0
deuterated block				
l_d [Å]	165.2	224.2≈165.2x1.36	172.2	167.0
$\rho_d[10^{-6}\,Å^{-2}]$	3.30	5.08	5.35	3.33
$l_{BL,\,d}$ [Å]	33.0	44.8	34.4	33.4
$n_{water,\,swell}$	1.9	6.0	2.4	2.0
m_{H_2O}	1.9	1.1	1.2	1.9
m_{D_2O}	0	4.9	1.2	0.1
σ_{sub} [Å]	5	5	5	5
$\sigma_{air} = \sigma_{int}$ [Å]	10.9	18.7	14.3	15.0

Table 6.2: Parameters of the d_5p_5 film deduced from the fits to the measurements shown in Fig. 6.8 and the corresponding SLD profiles in Fig. 6.9. Here is given length or thickness of each block (l), scattering length density (ρ), average bilayer thickness (l_{BL}), amount of water per PAH/PSS monomer ($n_{water,\,swell}$), amount of H_20 (m_{H_2O}) and amount of D_2O (m_{D_2O}), roughness of silicon substrate (σ_{sub}), internal (σ_{int}) and outer film/air roughness (σ_{out}).

Swelling experiments in 100% r.h. D_2O performed with films dried in vacuum show that one proton of each allylamine hydrochloride monomer changes position with one deuterium ion [Klitzing2003]. Since the film shown in Figure 6.8 is not only exposed to 100% r.h. D_2O atmosphere, but first immersed in liquid D_2O, one can imagine that not only one, but three of the protons of the PAH monomers are replaced by deuterium ions. Also, before first drying (Fig. 6.8, curve 3) sample was in contact with D_2O only.

Thus, deuterium incorporation has to be understood on a molecular basis: the number of water molecules per PAH/PSS monomer pair ($n_{water,\,swell}$) is determined by the increase in thickness. But even if we assume that all incorporated molecules are D_2O, the reflected intensity is too low, the fits do not show each maximum, and every second maximum is akin to a shoulder; especially the scattering length density of the deuterated block (ρ_d) is too small (cf. Table 6.3).

To explain the magnitude of ρ_d, a certain number of protons and deuterium ions are required, which are distributed between the water molecules and the amino groups of the polycation. Because of the fast proton–deuterium exchange found for protein NMR in D_2O, one can suggest that all three D are bound to each amino group and call the polycation PAD_3. Then, for deuterated block at 100% r.h. D_2O the numbers for deuterium atoms and protons are 12.8D ($2 \cdot 4.9 + 3$) and 2.2 H, respectively (cf. Table 6.3, top right).

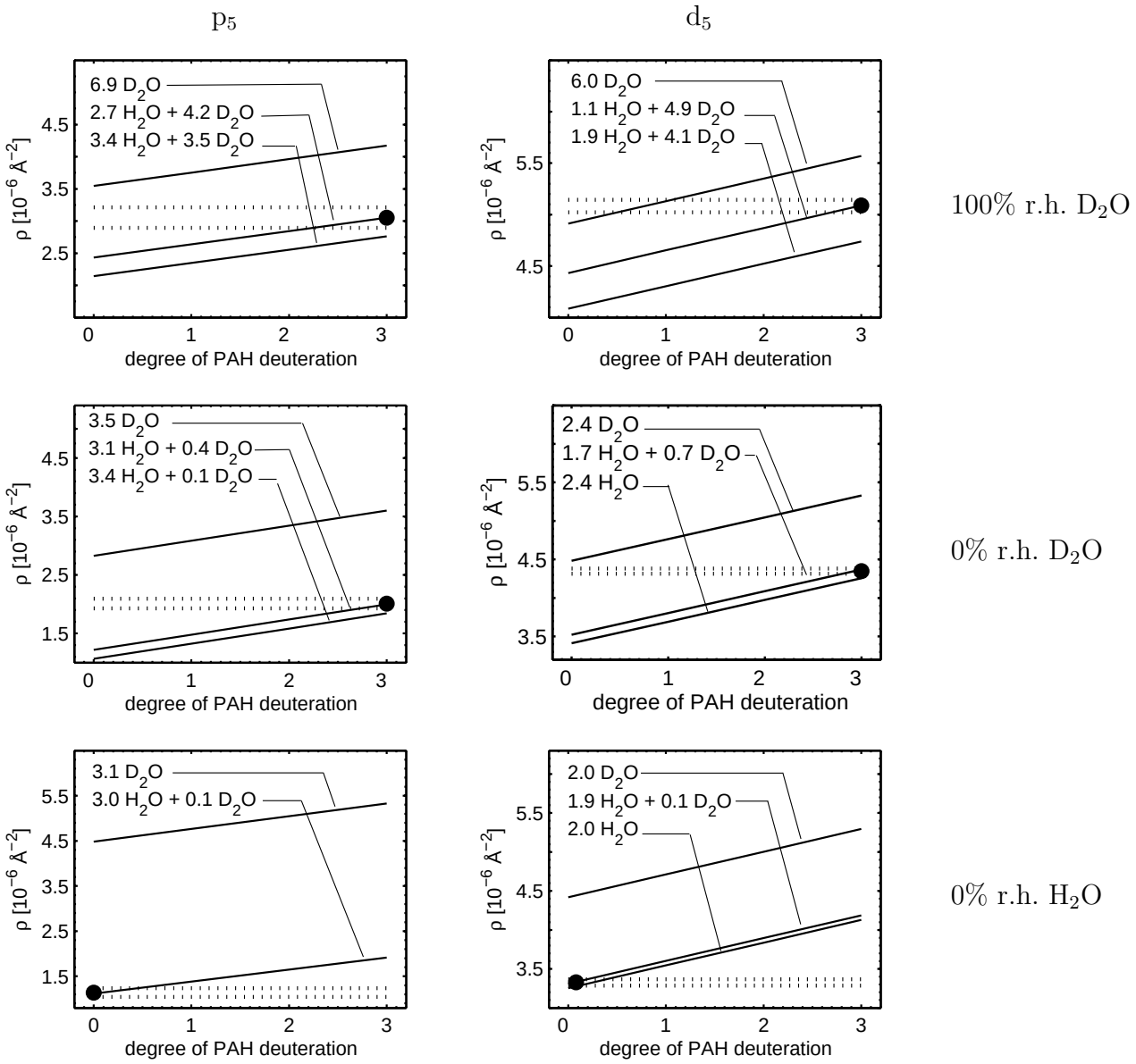

Table 6.3: Calculation of the SLD composition for the d_5p_5 film shown in Fig. 6.8. Here left colomn: SLD of protonated part (ρ_p) and right colomn: SLD of deuterated part (ρ_d) measured at 100% r.h. D_2O (top); at 0% r.h. directly after D_2O contact (middle); at 0% r.h. after immersion for 6 h in H_2O and subsequent 20 h of drying (bottom). The x–axis gives the degree of PAH deuteration ($PAH_{3-i}D_i$, with $0 < i < 3$); the straight lines are calculated for different values of light water amount m_{H_2O} from the thickness change of the film; the dotted lines show the confidential region of SLD (10% χ^2 variation) determined by the fits.

In summary, this experiment is reversible in terms of proton–deuterium exchange and swelling. The results are consistent with a complete replacement of three H^+ in the polycation monomers by three D^+ after submerging the film for half an hour in liquid D_2O. Most of the tightly bound water molecules found at the beginning of the experiment remain in the film. To find out whether this behaviour is general, other block architectures are investigated.

Fully protonated p_{10} polyelectrolyte film prepared at 15^0 C.

To determine the swelling of the fully protonated p_{10} film prepared at 15^0 C, the same experimental procedure is used as for d_5p_5 architecture: reflectivity measurements were performed at 100% r.h. D_2O after having dipped it into liquid D_2O for half an hour (cf. Fig. 6.12). Fit quality for curve 2 can be improved by using 2 box model, but leads to counterintuitive parameters which are not independent.

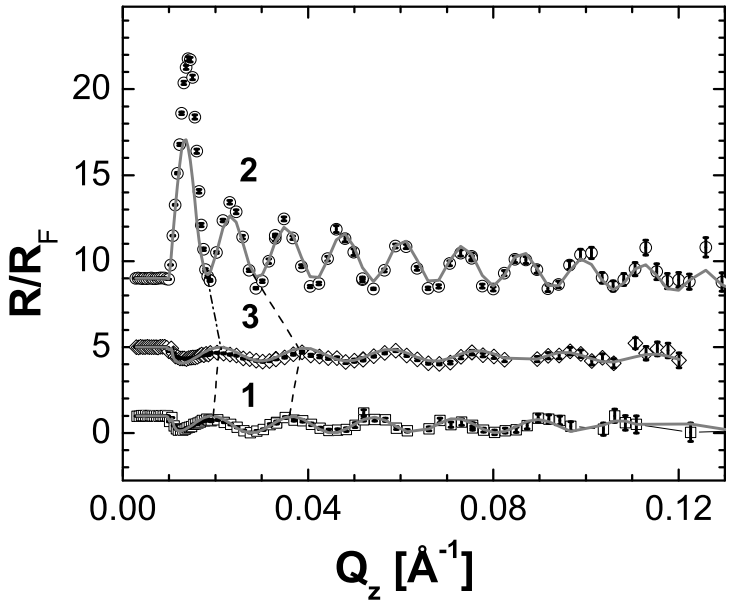

Figure 6.12: Normalized neutron reflectivity curves of p_{10} architecture prepared at 15^0 C and 1 mol/L NaCl. Here numbers above the curves represent the sequence of the experiments: (1) - 0% r.h., (2) - 100% r.h D_2O (after immersion for 30 min in liquid D_2O), (3) - back to 0% r.h. (after immersion for 34 h in H_2O and 86 h of drying). Straight lines are fits; dashed lines connect interference extrema of the same order.

Note that at 100% r.h. D_2O (cf. Fig. 6.12) a contrast inversion at the substrate/film interface occurs, causing a 180^0 shift in the reflected intensity. Therefore, minima of curve 2 are connected with maxima of curves 1 and 3. To ensure reversibility, the measurement at 100% r.h. D_2O is repeated three times; curve 3 is also repeated once (not shown). The corresponding scattering length density profiles can be seen in Fig. 6.13.

The water uptake in this case is very intriguing: the increase in thickness results in $n_{water,\,swell}$=7.9 (cf. Table 6.4). At 0% r.h. the parameters of a p_{10} film are in the expected range of a film built at 15^0 C from an aqueous polyelectrolyte solution (3 mmol/L) containing 1 mol/L NaCl. The thickness of the bilayer is l_{BL}=35.1 Å and $n_{\mathrm{water,\,dry}}$=3.2 (expected: l_{BL}=35±1 Å and $n_{\mathrm{water,\,dry}}$=3.5 [Gopinadhan2007b].

The data are consistent with full deuteration of PAH monomer (PAD_3), see Fig. 6.11 and Tables 6.4, 6.5. Here 4.9 D_2O molecules are incorporated, and almost all tightly bound H_2O molecules remain in the film. After immersing p_{10} film for 30 min in H_2O and 86 h of drying the water removal was more thorough than in a freshly prepared film, which was dried for 1

or 2 h only. This experiment also shows that the removal of deuterium is less effective than originally assumed (0.5 tightly bound D_2O molecules per PAH/PSS monomer are found). A possible interpretation is a deuterium migration from PAD_3 to the tightly bound almost immobile H_2O molecules.

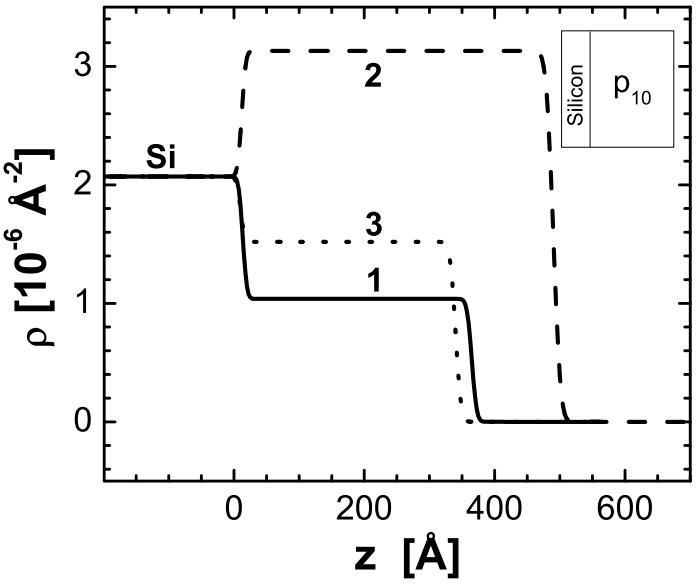

Figure 6.13: The SLD profiles derived from the measurements shown in Fig. 6.12. SLD of protonated block for curve 2 is increased due to incorporation of deuterium ions. Here left to right: silicon, p_{10} block with adjacent film/air interface.

p_{10}	0% r.h.	100% r.h. (D_2O) m for PAD_3	back to 0% r.h. after H_2O contact m for PAD_3
protonated block			
l_p [Å]	351.3	475.2≈351.3x1.35	329.8
$\rho_p[10^{-6}$ Å$^{-2}]$	1.04	3.10	1.52
$l_{BL,p}$ [Å]	35.1	47.5	33.0
$n_{water,swell}$	3.2	7.9	2.5
m_{H_2O}	3.2	3.0	2.0
m_{D_2O}	0	4.9	0.5
σ_{sub} [Å]	5	5	5
$\sigma_{air} = \sigma_{int}$ [Å]	6.0	13.4	6.7

Table 6.4: Parameters of the p_{10} film deduced from the measurements and fits shown in Fig. 6.12 and corresponding SLD profiles in Fig. 6.13. Here is given length of protonated block (l_p), scattering length density (ρ_p), average bilayer thickness ($l_{BL,p}$), amount of water per PAH/PSS monomer ($n_{water,swell}$), amount of H_20 (m_{H_2O}) and amount of D_2O (m_{D_2O}), roughness of silicon substrate (σ_{sub}) and outer roughness (σ_{out}).

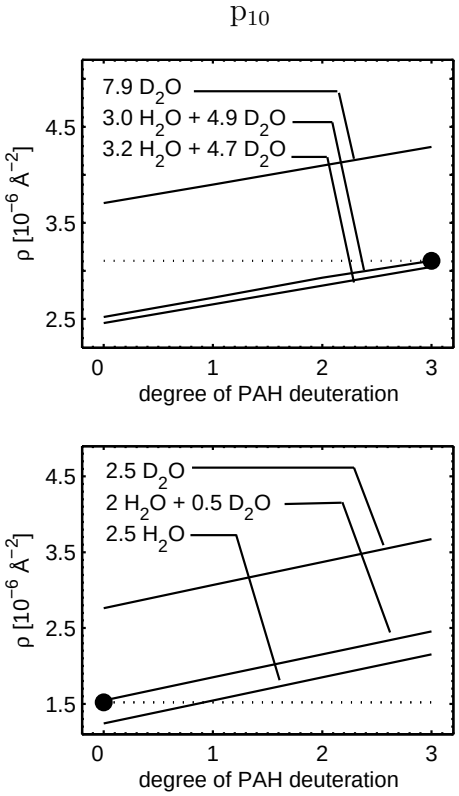

100% r.h. D_2O

0% r.h. H_2O

Table 6.5: Calculation of the SLD composition for the p_{10} film shown in Fig. 6.12, Fig. 6.13: at 100% r.h. D_2O (top) and at 0% r.h. after immersion in H_2O and subsequent drying (bottom). The x–axis gives the degree of PAH deuteration ($PAH_{3-i}D_i$, with $0 < i < 3$); the straight lines are calculated for different values of m_{H_2O} from the thickness change of the film; the dotted lines show SLD determined from the fits.

Protonated – deuterated p_5d_5 polyelectrolyte film prepared at 35^0 C.

A film architecture complementary to the one shown in Figure 6.8 is p_5d_5 prepared at 35^0 C and only the initial PEI layer was adsorbed at room temperature (cf. Fig. 6.14 and Fig. 6.15). This film is used to confirm the emerging picture (substitution of all protons of the polycation by deuterium ions on immersion into heavy water, most of the tightly bound water found in the films at 0% r.h. remains in the film and is not replaced by D_2O molecules) and to address some related questions such as (i) whether we can calculate the H_2O incorporation from the thickness change only (to confirm eq. 6.1) and (ii) does heavy water induces more swelling than light water.

As one can see, at 0% r.h. D_2O the substrate and the protonated block have almost the same scattering length density; thus, contrast is reduced (cf. Fig. 6.15). Also, at 100% r.h. D_2O the contrast is inverted at this interface (interference minima and maxima of the same order are connected with dotted lines), cf. Fig. 6.14. To ensure reversibility, the measurements at 100% r.h. H_2O and 100% r.h. D_2O were repeated.

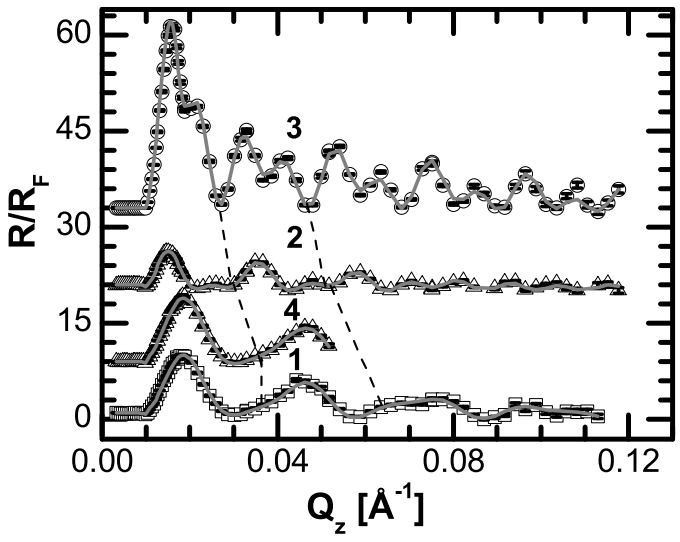

Figure 6.14: Normalized neutron reflectivity curves of p_5d_5 architecture prepared at 35^0 C and 1 mol/L NaCl. Here numbers above the curves represent the sequence of the experiments: (1) - 0% r.h., (2) - 100% r.h H_2O (after immersion for 30 min in liquid H_2O), (3) - 100% r.h D_2O (after immersion for 30 min in liquid D_2O), (4) - back to 0% r.h. (after reimmersion in H_2O for 8 h and 8 h of drying). Straight lines are fits; dashed lines connect interference extrema of the same order.

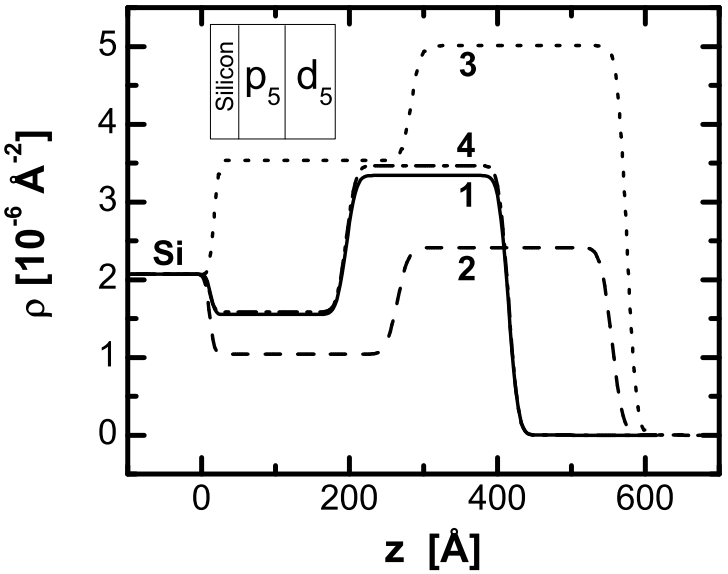

Figure 6.15: The SLD profiles derived from the measurements in Fig. 6.14. Left to right: silicon, p_5 block smeared out by internal roughness and d_5 block with adjacent film/air interface.

p_5d_5	0% r.h.	100% r.h. (H_2O) m for PAD_3	100% r.h. (D_2O) m for PAD_3	back to 0% r.h. after H_2O contact m for PAH_3
protonated block				
l_{p} [Å]	183.5	254.0≈183.5x1.38	266.6≈183.5x1.45	184.3
$\rho_{\mathrm{p}}[10^{-6}\,\text{Å}^{-2}]$	1.55	1.04	3.54	1.59
$l_{\mathrm{BL,\,p}}$ [Å]	36.7	50.8	53.3	36.9
$n_{\mathrm{water,\,swell}}$	0.1	3.9	4.6	0.1
$m_{\mathrm{H_2O}}$	0.1	3.9	0.6	0.1
$m_{\mathrm{D_2O}}$	0	0	4.0	0.0
deuterated block				
l_{d} [Å]	219.3	290.2≈219.3x1.32	291.7≈219.3x1.33	219.4
$\rho_{\mathrm{d}}[10^{-6}\,\text{Å}^{-2}]$	3.34	1.59	5.00	3.47
$l_{\mathrm{BL,\,d}}$ [Å]	43.9	58.0	58.3	43.9
$n_{\mathrm{water,\,swell}}$	1.7	5.5	5.6	1.7
$m_{\mathrm{H_2O}}$	1.7	5.5	1.2	1.5
$m_{\mathrm{D_2O}}$	0	0	4.4	0.2
σ_{sub} [Å]	5	5	5	5
$\sigma_{air} = \sigma_{int}$ [Å]	10.5	12.0	10.3	10.3

Table 6.6: Parameters of the p_5d_5 film deduced from the fits to the measurements shown in Fig. 6.14 and the corresponding SLD profiles in Fig. 6.15.

Table 6.6 contains all parameters of the p_5d_5 film obtained under different conditions. Here is hardly any water found in the protonated layer adjacent to the substrate $n_{\mathrm{H_2O,\,dry}}$=0.1 instead of expected from the literature $n_{\mathrm{H_2O,\,dry}}$=3.5 [Gopinadhan2007b]. Furthermore, the thickness per polyelectrolyte bilayer in the protonated block is lower than expected for PEMs prepared at this elevated temperature $l_{\mathrm{BL,\,p}}$=36.7 Å instead of the expected from the literature l_{BL}=44±1 Å [Gopinadhan2007b].

If the standard value of bound water is assumed ($n_{\mathrm{H_2O,\,dry}}$=3.5), the thickness of bilayer is larger than described in literature [Gopinadhan2007b] and leads to a bilayer thickness l_{BL}=49.7 Å instead of the expected 44±1 Å. Thus, one can conclude that the polymer coverage in precursor layers exceeds the coverage in the center of the film, and the water is bound less tightly. The thickness of the bilayer in the deuterated block ($l_{\mathrm{BL,\,d}}$=43.9 Å) is consistent with the expected value of 44±1 Å although the water content is smaller ($n_{\mathrm{H_2O,\,dry}}$=1.7 instead of 3.5) [Gopinadhan2007b].

Exposed to 100% r.h. H_2O the same amount of water is incorporated in both layers $n_{\mathrm{water,\,swell}}$ - $n_{\mathrm{H_2O,\,dry}}$=3.8, as indicated by the changes of the thickness and the decrease in scattering length density. However, with the swelling experiment of p_5d_5 film prepared at 35^0 C and measured in 100% r.h. H_2O, we can also cross-check the validity of our approach to calculate the swelling both from the increase of the thickness (eq. 6.1) and from the change in scattering length density (eq. 6.2). Since, no additional deuterium ions are incorporated, we have two equations and one parameter ($n_{\mathrm{water,\,swell}}$) for both the protonated and the deuterated layer; $n_{\mathrm{water,\,swell}}$ differs by 0.1 water molecule per PAH/PSS monomer pair depending on the equation used.

At 100% r.h. D_2O (after dipping the film in heavy water for half an hour) the thickness of the protonated block increases (at 100% r.h. D_2O $n_{\mathrm{water,\,swell}}$=4.6 instead of 3.8 at

100% r.h. H_2O) while the thickness of the deuterated block remains almost unchanged. As expected, the scattering length densities increase dramatically. At the substrate/film interface there is a contrast inversions the scattering length density of the film is now larger than that of the substrate. As one can see in Fig. 6.14, at 100% r.h. D_2O a phase jump occurs (minima of the 100% r.h. D_2O connected with maxima of the 100% r.h. H_2O). To ensure reproducibility, the measurements at 100% r.h. H_2O and D_2O were immediately repeated (not shown here). Intriguing, that film/air roughness is reversible in terms of swelling and drying.

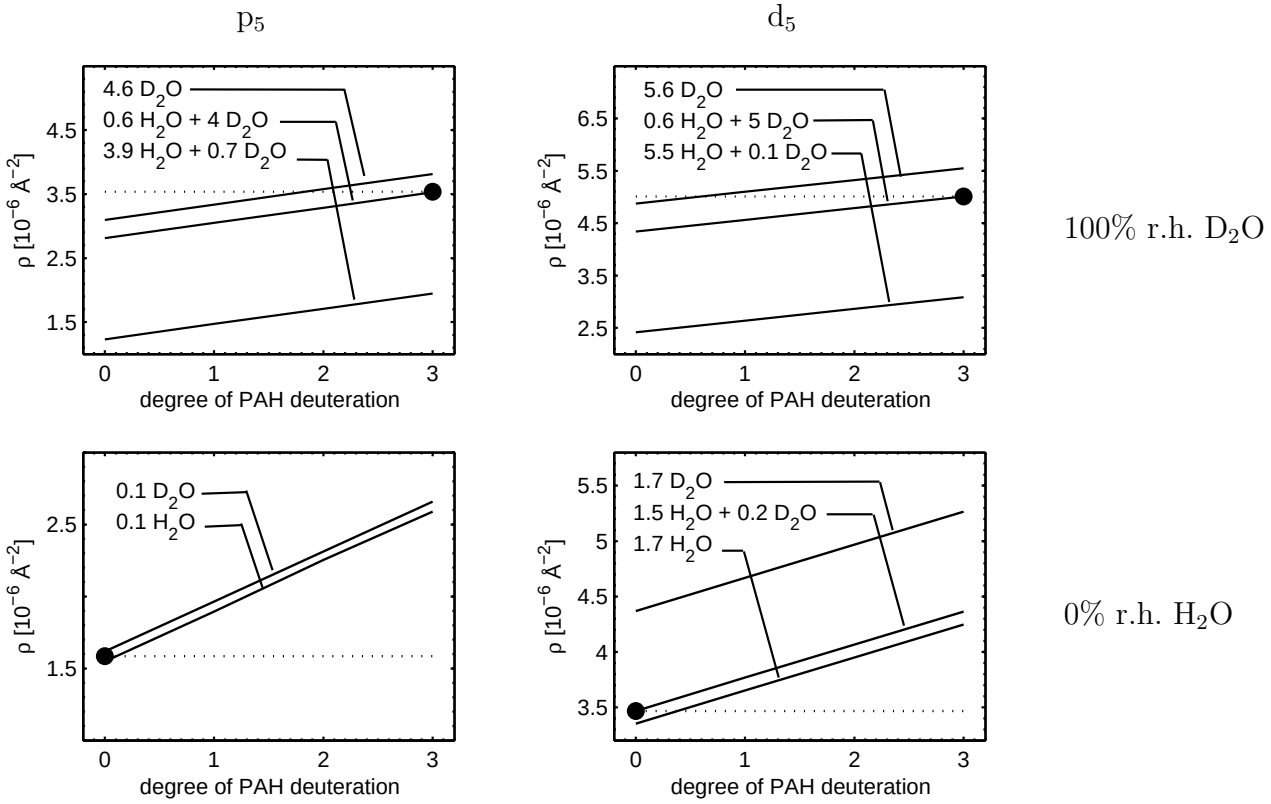

Table 6.7: Calculation of the SLD composition for the p_5d_5 film shown in Fig. 6.14, Fig. 6.15: SLD of protonated (ρ_p) and deuterated parts (ρ_d) at 100% r.h. D_2O (top); at 0% r.h. after immersion for 8 h in H_2O and subsequent 8 h of drying (bottom). The x–axis gives the degree of PAH deuteration ($PAH_{3-i}D_i$, with $0 < i < 3$); the straight lines are calculated for different values of m_{H_2O} from the thickness change of the film; the dotted lines show the SLD from the fits.

The interpretation of the scattering length density in this case is rather unambiguous (cf. Table 6.7): the scattering length density of the protonated block is so large that two or three protons per polycation monomer have to be replaced by deuterium ions; otherwise, amount of light water (m_{H_2O}) would be negative. It is possible to return to the original film composition, yet in the deuterated block a fraction of D_2O molecules remains (m_{D_2O}=0.2 with $n_{H_2O,\,dry}$=1.7).

To confirm the unexpected observation that there is no tightly bound water in the protonated block next to the substrate, another film with p_5d_5 architecture prepared at 15^0 C was investigated.

Protonated – deuterated p_5d_5 polyelectrolyte film prepared at 15^0 C.

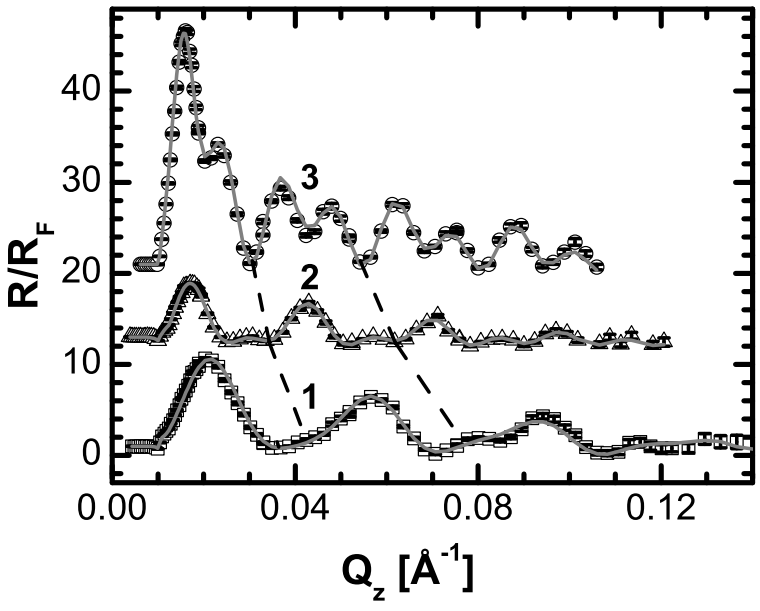

Figure 6.16: Normalized neutron reflectivity curves of p_5d_5 architecture prepared at 15^0 C and 1 mol/L NaCl. Here numbers above the curves represent the sequence of the experiments: (1) - 0% r.h., (2) - 100% r.h H_2O (after immersion for 30 min in liquid H_2O), (3) - 100% r.h D_2O (after immersion for 30 min in liquid D_2O). Straight lines are fits; dashed lines connect interference extrema of the same order.

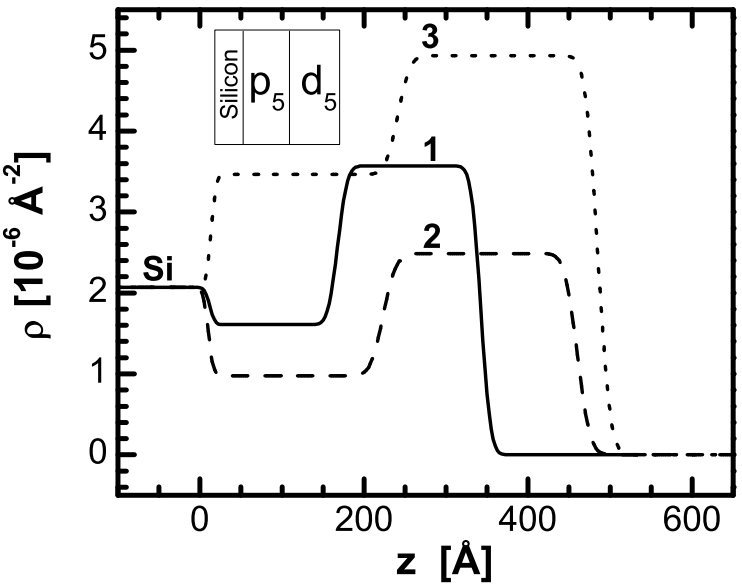

Figure 6.17: The SLD profiles derived from the measurements in Fig. 6.16. Left to right: silicon, p_5 block smeared out by internal roughness and d_5 block with adjacent film/air interface.

The measurements and fits for p_5d_5 architecture prepared at 15^0 C are shown in Fig. 6.16 and the corresponding SLD profiles in Fig. 6.17. As one can from parameter table (cf. Table 6.8), the freshly prepared film shows a similar water content as the p_5d_5 film prepared at 35^0 C ($n_{H_2O,\,dry}$=0 for the protonated and $n_{H_2O,\,dry}$=1.1 for the deuterated block). Note that $n_{water,\,swell}$=$n_{H_20,\,dry}$ for the initial measurement at 0% r.h. Again, the bilayer thickness within the protonated block is lower than expected from the literature, yet the deuterated block is in agreement with the previous results ($l_{BL,\,p}$=31.2 Å and $l_{BL,\,d}$=34.9 Å, respectively). Assuming 3.5 water molecules [Gopinadhan2007b] incorporated by bilayers of the protonated block, the thickness of the bilayer is again larger than expected (n_{H_2O}=3.5 would lead to the bilayer thickness of $l_{BL,p}$=42.2 Å, which exceeds the expected 35±1 Å). Thus, we conclude that the precursor layers next to the substrate show increased polymer coverage and less bound water.

At 100% r.h. H_2O the additional amount of incorporated light water is similar for both blocks (cf. Table 6.8). The deuterated block includes more water because it contains more water in the dried state ($n_{water,\,swell}$=3.8 for the protonated and $n_{water,\,swell}$=5.0 for the deuterated block). Exposed to 100% r.h. D_2O, the swelling is slightly increased for both blocks ($n_{water,\,swell}$=4.5 for the protonated and $n_{water,\,swell}$=5.4 for the deuterated block). To ensure reversibility, the measurement at 100% r.h H_2O and D_2O were repeated. The reversibility check for the dry state (back to 0% r.h.) was not completed and therefore not shown here.

p_5d_5	0% r.h.	100% r.h. (H_2O) m for PAD_3	100% r.h. (D_2O) m for PAD_3
protonated block			
l_p [Å]	155.9	213.6≈155.9x1.37	227.5≈155.9x1.46
$\rho_p[10^{-6}$ Å$^{-2}]$	1.61	0.98	3.46
$l_{BL,\,p}$ [Å]	31.2	42.7	45.5
$n_{water,\,swell}$	0	3.8	4.5
m_{H_2O}	0	3.8	0.7
m_{D_2O}	0	0	3.8
deuterated block			
l_d [Å]	174.7	236.3≈174.7x1.35	243.8≈174.7x1.39
$\rho_d[10^{-6}$ Å$^{-2}]$	3.57	2.49	4.93
$l_{BL,\,d}$ [Å]	34.9	47.3	48.8
$n_{water,\,swell}$	1.1	5.0	5.4
m_{H_2O}	1.1	5.0	1.3
m_{D_2O}	0	0	4.1
σ_{sub} [Å]	5	5	5
$\sigma_{air} = \sigma_{int}$ [Å]	9.3	12.3	11.9

Table 6.8: Parameters of the p_5d_5 film deduced from the fits to the measurements shown in Fig. 6.16 and the corresponding SLD profiles in Fig. 6.17.

The common finding for the samples with p_5d_5 architecture prepared at 15^0 C and 35^0 C is that the thickness increases in 100% r.h. D_2O slightly more than in 100% r.h. H_2O. Averaging over all blocks there is an increase of about 4%.

Fully deuterated d_{10} polyelectrolyte film prepared at 15^0 C.

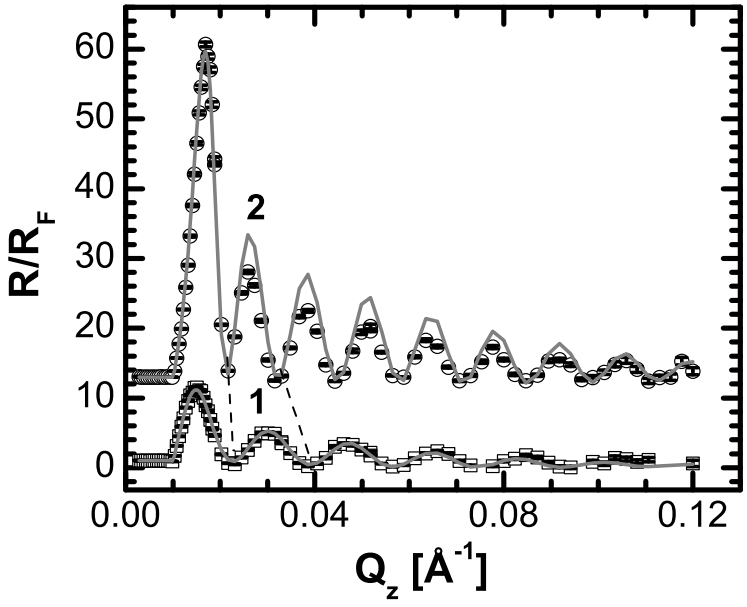

Figure 6.18: Normalized neutron reflectivity curves of d_{10} architecture prepared at 15^0 C and 1 mol/L NaCl. Here numbers above the curves represent the sequence of the experiments: (1) - 0% r.h., (2) - 100% r.h D_2O (after immersion for 30 min in liquid D_2O). Straight lines are fits; dashed lines connect interference minima of the same order.

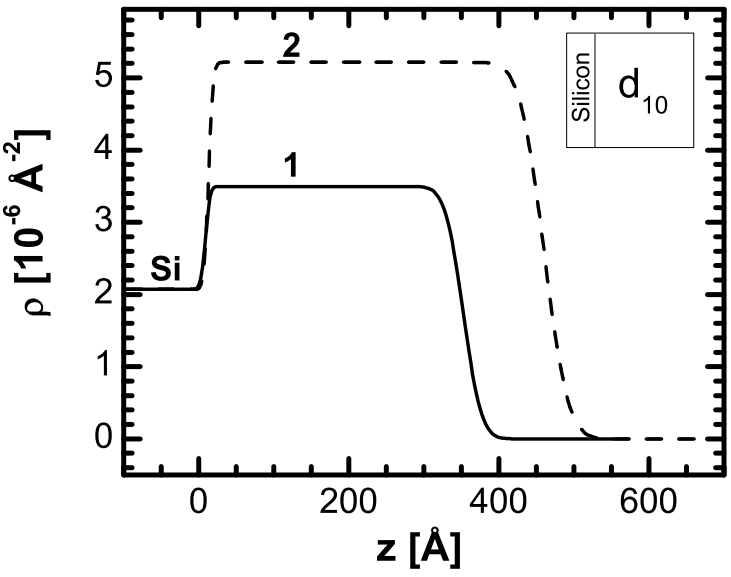

Figure 6.19: The SLD profiles derived from the measurements in Fig. 6.18. Left to right: silicon, d_{10} block with adjacent film/air interface.

The fully deuterated d_{10} film prepared at 15^0 C was investigated in 0% r.h. and 100% r.h. D_2O (cf. Fig. 6.18). To ensure reversibility, the measurement at 100% r.h D_2O was repeated and the resulting combined signal is presented. The corresponding scattering length density profiles are shown in Fig. 6.19.

d_{10}	0% r.h.	100% r.h. (D_2O) m for PAD_3
deuterated block		
l_p [Å]	343.6	451.3≈343.6x1.31
$\rho_d[10^{-6}$ Å$^{-2}]$	3.50	5.23
$l_{BL,d}$ [Å]	34.4	45.1
$n_{water,swell}$	1.3	4.8
m_{H_2O}	1.3	0.6
m_{D_2O}	0	4.2
σ_{sub} [Å]	5	5
$\sigma_{air} = \sigma_{int}$ [Å]	19.1	19.0

Table 6.9: Parameters of the d_{10} film deduced from the fits to the measurements shown in Fig. 6.18 and the corresponding SLD profiles in Fig. 6.19. Note that here $n_{water,swell}$=$n_{H_20,dry}$ for the initial measurement at 0% r.h.

Analyzing parameters of the sample (cf. Table 6.9), one can see that very less water is found in the dry state ($n_{H_2O,dry}$=1.3), although the thickness of the bilayer is very much in the expected range $l_{BL,d}$=34.4 Å according to the literature l_{BL}=35±1 Å [Gopinadhan2007b]. The sample swells by 31% in D_2O (from thickness increase). Assuming the formation of PAD_3, the 0.6 H_2O molecules remain bound after swelling in 100% r.h. D_2O. Since both PAH_3D_0 and PAH_2D_1 (cf. Fig. 6.11) would lead to a negative water content, it has to be that two or three protons per PAH monomer are exchanged by deuterium ions (cf. Table 6.9).

6.4 Proton–Deuterium Exchange in PAH Monomers

The results obtained on the immobile water molecules are shown in Figure 6.20. Here the number of protons attributed to tightly bound water molecules (per monomer pair) is shown for all films investigated under different environmental conditions. Amount of protons is calculated from the thickness increase (eq. 6.1) and the according scattering length density (eq. 6.3).

To verify the hypothesis that the amount of tightly bound water molecules within a film is fairly constant for 0% r.h. H_2O three protons of an amino group in a polycation monomer are subtracted for all examined films. As one can see, all deuterated blocks show a very similar behaviour with 2.8±0.8 protons (or 1.4±0.4 water molecules) bound. Interestingly, two different kinds of protonated blocks exist: the core and/or outer zone with about 6.2 protons per monomer pair (p_{10} and d_5p_5), which is in agreement with the values found in the literature [Gopinadhan2005]. The proton block in the precursor zone contains about 0 protons (or no water) for p_5d_5 architecture prepared at 15^0 C and 35^0 C. There are deviations from a straight line, and a few data points suggest that two, not three, protons are exchanged by deuterium ions per polycation monomer pair.

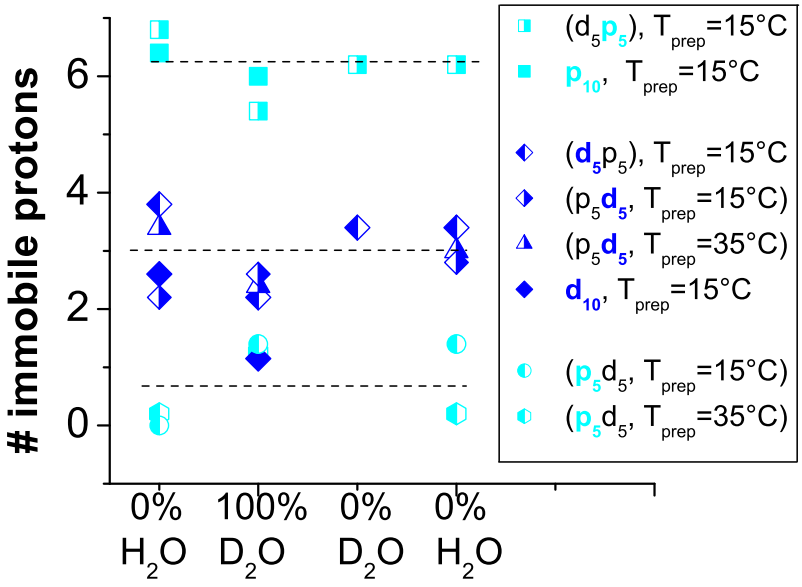

Figure 6.20: Amount of protons attributed to tightly bound water molecules per monomer pair measured at different environmental conditions and the relative humidity (r.h.) given in the x–axis in the sequence of the experiments. Here left to right: 0% r.h. – dry conditions (initial measurements), 100% r.h. D_2O – measured in D_2O atmosphere, 0% r.h. D_2O – performed after measuring sample in D_2O atmosphere and subsequent drying, 0% r.h. H_2O – after measuring sample in H_2O atmosphere and resulting drying. In case of 0% r.h. H_2O film had access only to light water molecules and in case of 0% r.h. D_2O – to heavy water. For each measurement performed in a H_2O atmosphere, three protons are subtracted since they are bound to the amino group. Dotted lines are a guide to the eye and indicate three different sorts of layers containing different amount of tightly bound water molecules. For most measurements, the symbols exceed the size of the error bars. For those protonated layers with many protons, the error from the fits shown in the preceding figures is larger and amounts to 0.6 protons. Position of the blocks (color coded) corresponds to amount of water: top - in protonated core/outer layer ($\approx$ 6.2 protons or 3.1 H_2O molecules), center - in deuterated layers ($\approx$ 3.0 protons or 1.5 H_2O molecules) and bottom - in protonated precursor layers ($\approx$ 0 protons).

6.5 Discussion

In summary, the experiments on p_{10}, d_{10}, d_5p_5, p_5d_5 prepared at 15^0 C and p_5d_5 prepared at 35^0 C are all consistent with the following features:

- After immersion in D_2O all PEM data indicate that three protons in the amino group of each polycation monomer are substituted by deuterium ions.
- The majority of the tightly bound water molecules found in the freshly prepared, dried films remain in the film and are not replaced by D_2O molecules.
- The thickness of deuterated polycation/polyanion bilayers in deuterated PEM or in deuterated blocks is in accordance with previously published results for polyelectrolyte multilayer films consisting of protonated layers [Gopinadhan2007b].

However, there is consistently less bound water in the deuterated films ($n_{\mathrm{H_2O,\,dry}}$=1.1–1.9 instead of $n_{\mathrm{H_2O,\,dry}}$=3.5).

- The thickness and water content of the bilayers in protonated PEM and the protonated blocks adjacent to the air side are consistent with previously reported values with respect to thickness of the bilayer as well as the water content [Gopinadhan2005], [Gopinadhan2007b].

However, protonated layers adjacent to the substrate do not contain any tightly bound water while the polyelectrolyte coverage is higher.

- The internal roughness and the film/air roughness are identical, even though it can increase by a factor of 2 if the film is swollen.

It is well known that the water uptake is almost immediate, while apparently the water release has a longer time scale for the protonated blocks: after 86 h of drying the p_{10} block has only 2.4 water molecules (instead of the original 3.2 obtained after 30 min of drying), and the protonated block of p_5d_5 does not come back to 0.1 water molecules, but still has 1.4 water molecules after 6 h of drying.

Each of the above statements is supported by measurements on at least two different PEMs.

Most measurements show an increased roughness at the film/air interface upon exposure to 100% r.h. After drying, the roughness decreases somewhat but does not necessarily reach the original value (cf. corresponding tables).

The scattering length density of the deuterated blocks is higher than almost all values published for the selectively deuterated layers in PEMs [Lösche1998], [Schönhoff2003b], [Klitzing2003], [Gopinadhan2007b]. The problem of the quoted experiments is the film architecture: for selectively deuterated layers the thickness of the deuterated slab is at best three times the roughness of the internal interfaces above and below the deuterated slab. Therefore, the maximum in the scattering length density profile (which is well described by a Gaussian) is by default smaller than the nominal scattering length density of the deuterated layer. The obtained values are thus an estimate: with an increased scattering length density and increased roughness the same scattering length density profile is obtained. In this context it is helpful to consider that in our experiments the roughness of the internal interface between the protonated and the deuterated block has the same value as the film/air roughness. Helpful, that our deuterated blocks are thicker then roughness by order of magnitude or more.

As described previously, almost all examined films and isolated blocks swell by 30–35%. However, the two p_5d_5 layers behave differently: in 100% r.h. D_2O the thickness of the protonated layer increases by 45% (cf. Table 6.6); at 100% r.h. H_2O the protonated block incorporates just as much water as any protonated PEM ($n_{water,\,swell} - n_{\mathrm{H_2O,\,dry}} \approx 3.9$), although the original water content was lower ($n_{\mathrm{H_2O,\,dry}} \approx 0.1$ instead of $n_{\mathrm{H_2O,\,dry}} \approx 3.5$), and therefore the relative change of thickness is higher.

It appears that about the same amount of water is incorporated, independently of the number of tightly bound water molecules. The slightly increased swelling in 100% r.h. D_2O compared to 100% r.h. H_2O can be explained by the larger enthalpy between the heavy water molecules.

According to the zone model, [Ladam2000], [Salomäki2004a] the multilayer consists of a hard core and a softer precursor layer. The p_5d_5 films obviously have a film architecture with a clearly observable precursor zone. The low amount of bound water at 0% r.h. suggests that the water is mobile and the layer is softer and not in the glassy state like in the central zone of the multilayer [Salomäki2004a]. The blocks adjusted to substrate (p_5 in case of p_5d_5 architecture and d_5 for inverted structure) swell in D_2O by 15% to 27% more then outer blocks (see corresponding parameter tables). One can assume, that the p_{10} and d_{10} films also contain less bound water in the layers closest to the substrate, but it is difficult to resolve unambiguously. Less water in the layers adjacent to the substrate improves the fits, but the assignment of parameter is ambiguous.

At increasing temperatures [Gopinadhan2007b] less water in the films allows for higher polymer coverage. Without a tightly bound hydration shell the polymer chains can get closer to each other, and thus the segment/segment attraction increases and more polymer is adsorbed. This applies to the protonated precursor layer next to the substrate in the p_5d_5 films as well as to the deuterated blocks or films. Both contain less tightly bound water molecules and show higher polymer coverage. Apparently, it is more difficult to form hydration shells around deuterated nonpolar groups.

Finally, the results indicate that proton–deuterium exchange always occurs in the amino groups. We conclude that two or three protons are exchanged by deuterium ions. Furthermore, the water molecules found at 0% r.h. remain in the film even if the film is stored in D_2O. This is due to the fast exchange rate of the protons and the slow exchange rate of hydration water. There is less conclusive evidence of slow proton-deuterium exchange in the tightly bound water molecules. Drying after immersion in light water does not always lead to a complete removal of the deuterium; a small percentage is retained, and the deuterium ions obviously move into the tightly bound hydration water.

6.6 Conclusion

The PEMs investigated either consist of 10 protonated polyelectrolyte bilayers (p_{10}), 10 deuterated bilayers (d_{10}), or of two different blocks, p_5d_5 or d_5p_5. The variation of the PEM architecture leads to a broad variation in the obtained neutron reflectivity curves. If a protonated layer is next to the substrate, contrast inversion occurs after deuterium has been incorporated. If block architecture is used, we observe two different periodicities in the measurement: one from the film thickness, superimposed by the beats from the thinner blocks. The very different results can be explained by the same model which thus provides a robust description of the system. Prior to the exposure to 100% r.h. D_2O or H_2O, PEM is immersed in liquid D_2O or H_2O for at least half an hour.

The obtained scattering length density profiles provide insight into the exchange rates of the constituent molecules: two or three mobile protons of each PAH monomer are replaced by deuterium ions, although most of the H_2O molecules found in PEM at 0% r.h. remain bound at 100% r.h. D_2O. However, in a p_5 precursor block adjacent to the substrate no tightly bound water is found, which indicates a soft layer as it was suggested by the zone model. Tightly bound water molecules are only found in the PEM core zone. In contrast, in the deuterated layers the amount of tightly bound water molecules is constant and independent of the film architecture. The data indicate that three mobile protons of each PAH monomer are replaced by deuterium ions, yet most of the H_2O molecules found in PEM at 0% r.h.

remain bound at 100% r.h. D_2O. This is in consistency with the fact that the core of PEM is in a glassy state (a direct consequence of zone model). At 0% r.h., the amount of bound water in the deuterated layers does not depend on the film architecture, whereas in the protonated layers it does. Also, it was shown that all incorporated water leads to the thickness increase.

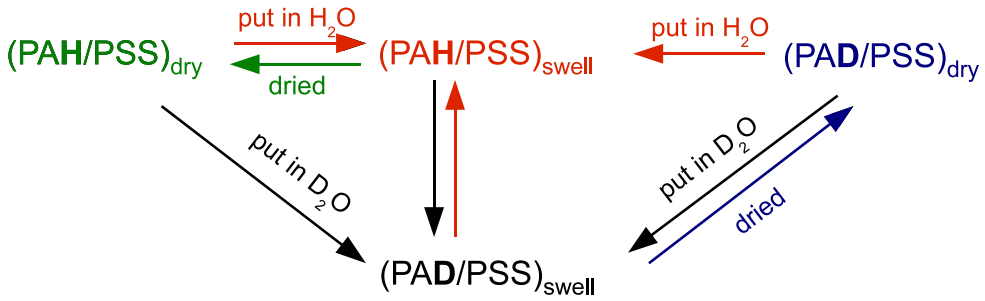

Figure 6.21: Schematic of the proton – deuterium exchange mechanism based on the findings discussed above. As one can see, swelling in light water is reversible process (horizontal line) and proton–deuterium exchange can be obtained either after swelling first in light water (H_2O) and then in heavy water (D_2O), or directly by swelling in D_2O. Note that it is not enough just to dry film after swelling in D_2O to obtain original state (protonated PAH), one has to swell it in light water first.

Chapter 7

Dependence of Thickness and Composition of PEMs on Temperature, Concentration and Type of Salt

7.1 Introduction

In this chapter results of temperature and salt influence on thickness and composition of polyelectrolyte multilayer films are presented. Two different sample architectures are used for these experiments. Initially, sample architecture with selectively deuterated polyanion layers (superlattice structure or simply superstructure) was chosen to improve the contrast in neutron reflectivity experiments. Such an approach is commonly used in neutron reflectometry, since it allows to obtain information about internal PEM structure, interpenetration of the layers and amount of water bound to the polyelectrolytes. On the other hand, new block architecture introduced in the previous chapter makes model assumptions unambiguous due to use of thick (relatively to the roughness of the adjacent interface) protonated and deuterated blocks. In this case, the roughness of an internal interface can be obtained as independent parameter.

The thickness of polyelectrolyte multilayer films and their composition depend on many factors, including preparation temperature, ionic strength of the solutions and kind of salt. The effect of salt concentration on polyelectrolyte build–up has been studied only at room temperature yet [Schmitt1996], [Lösche1998]. Simultaneous variation of temperature and salt concentration gives us a chance to find out at which ion concentration does the short–ranged attractive force between the chain segments overcome the electrostatic repulsion and temperature effect appears. For the latter study PAH/PSS multilayers were investigated with X–ray reflectivity, thus only protonated samples were prepared. The respective influence of preparation temperature and salt concentration in the deposition solution on the formation of PEM is shown in section 7.2.1. The effect of preparation temperature on film thickness and internal roughness was shown for superstructure samples consisting of one deuterated layer sandwiched between several protonated layers [Gopinadhan2005]. However, to confirm these results with block structure, influence of preparation temperature on the internal properties of the film (like amount of water bound to polyelectrolytes and roughness of the protonated–deuterated interface) was studied by means of neutron reflectivity (cf. section 7.2.2).

Intriguing results were obtained by temperature–dependent treatment after the sample preparation. The samples prepared at low temperature were heated in aqueous solutions (with and without salt) and investigated by means of neutron reflectivity (cf. section 7.2.3). Two competing attractive interactions can be distinguished: hydrophobic attraction between the layers that increases with heat and expulsion of water molecules from the multilayers [Jaber2006].

As mentioned in chapter 2, different salts have different propensities to precipitate or dissolve proteins in solution, which is known as Hofmeister effect. Remarkable, that though this effect has been known since 1880s, it is still poorly understood. However, Hofmeister effect is known to play an important role in several biological phenomena [Cacace1997] and attracted increasing interest in the last years [Boström2004], [Salomäki2004b], [Holzmann2007]. Classification of salt ions (presented in solution) according to their ability to change water structure is called Hofmeister series (cf. Fig. 7.1). It is related to the ionic radii of the ions: small monovalent ions strongly interact with the surrounding water molecules, due to a large charge density; large ions leave water undisturbed since distance from the ion center to the hydration shell is larger and hence the electric field is weaker there. The effect of salt counter–ions (cations and anions) in the deposition solution is discussed in section 7.3.

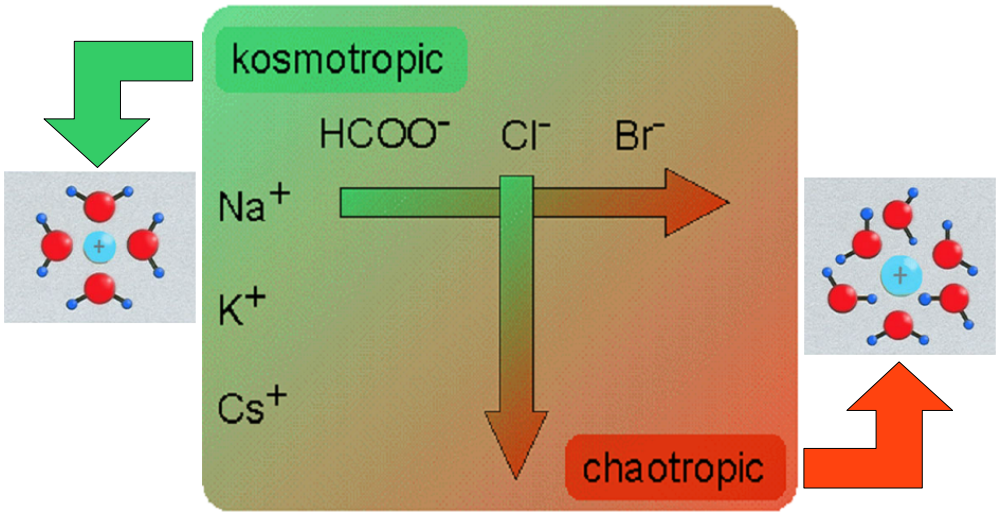

Figure 7.1: Hofmeister series of cations and anions used in this study are presented according to their ability make or break water structure. For anions the solubility of organic compounds changes on adding sodium salts in the order: $HCOO^- < Cl^- < Br^-$. For cations, the Hofmeister effect is usually less pronounced and follows: $Na^+ < K^+ < Cs^+$.

Dissolving a polyelectrolyte in water results in formation of a highly ordered shell of water around the molecule. Owing to its high polarity, the H_2O molecules closest to a dissolved ion are strongly attached to it, forming primary (first) water hydration shell. In Fig 7.2 hydration shell around anion can be seen. The increase in the solubility of organic substrates according to the Hofmeister series interferes with the intermolecular hydrogen bonds of water which cause a decrease of the order in the liquid [Parsegian1995]. One distinguishes kosmotropes (water structure makers) and chaotropes (water structure breakers). The influence of kosmotropic and chaotropic ions on the hydration water (water closest to the ion) can be understood as a balance between the water–water and ion–water interactions, which

varies considerably with the charge density of ions on the solute surface [Holzmann2007]. These interactions are shown schematically in Fig. 7.3.

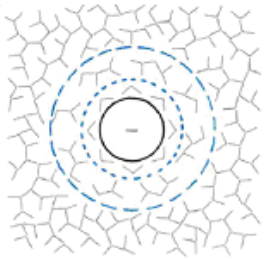

Figure 7.2: Schematic of the water structure, where gray corners represent water molecules. Blue dashed lines depict first and second water shells around anion, respectively.

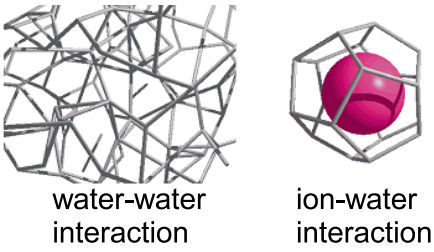

Figure 7.3: 3D schematic representation of the bulk water structure (water–water interaction) and water structure in the vicinity of an ion (ion–water structure). The picture is adapted from the lecture of R. Ludwig "Salt effects - towards understanding the Hofmeister series" (2007).

7.2 Effect of Temperature on PEMs

To find out the necessary conditions at which temperature–dependent secondary forces play major role, influence of temperature on PEM structure during and after multilayer build–up was studied experimentally.

7.2.1 The Onset of the Temperature Effect

Both parameters (temperature and salt concentration of the polyelectrolyte solution) have been varied systematically. Temperature of polyelectrolyte solution was varied from 5^0 C to 45^0 C and salt concentration (ionic strength of the solution) from zero (no additional salt in the polyelectrolyte solution) to 2 mol/L NaCl. Data for 2 mol/L NaCl were obtained by Matthias Cornelsen [Cornelsen2008]. Polyelectrolyte multilayer films were adsorbed on top of a silicon wafer from 3 mmol/L polyelectrolyte solution. Mainly, PEI/$(PSS/PAH)_5$/PSS film architecture consisting of 6 protonated polyelectrolyte pairs or bilayers (in short form p_6) is used for these experiments, except for the samples prepared from 2 mol/L salt having 6.5 bilayers: PEI/$(PSS/PAH)_6$. As example of salt influence on thickness of the PEM, some of Fresnel normalized X–ray reflectivity curves for p_6 samples adsorbed from 15^0 C are shown in Fig. 7.4. An increase of the film thickness for the samples prepared with increasing NaCl concentrations and constant preparation temperature can be seen. With increasing salt concentration in the preparation solution, one observes a narrowing of the oscillations (cf. Fig. 7.4), indicating film thickening accordingly to eq. 4.15 shown in section 4.1. PEM growth at constant temperature can be explained qualitatively by electrostatic interactions, which are tuned by the salt concentration and entropy, neglecting the finite volume of the ions and polymers involved.

As one can see in Fig. 7.5, preparation temperature of the polyelectrolyte solution profoundly affects the resulting polyelectrolyte multilayer thickness. These results were published in [Gopinadhan2007b], where it was pointed out that temperature causes an additional

thickening if the salt concentration exceeds 0.05 mol/L. Additional experiments performed with physiological concentration (0.15 mol/L) of salt solution [Cornelsen2008] indicate that the critical concentration, where temperature starts to influence the film thickness, lies rather between 0.1 mol/L and 0.5 mol/L. There is no temperature–induced difference in bilayer thickness until ≈ 0.1 mol/L (cf. Fig. 7.5) then the behaviour of multilayer growth changes and starts depending on the temperature over linear.

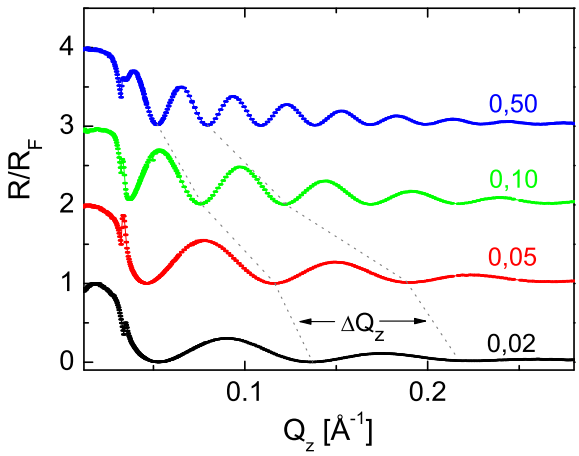

Figure 7.4: Normalized X–Ray reflectivity curves for p_6 films, prepared at 15^0 C from 3 mmol/L polyelectrolyte solution with different concentration of NaCl, indicated in mol/L. For clarity the curves are shifted by one unit vertically. Dotted lines connect same order minima of Kiessig–oscillations and indicate film thickening on increase of salt concentration, since distance between the minima ΔQ_z is inversely proportional to the film thickness.

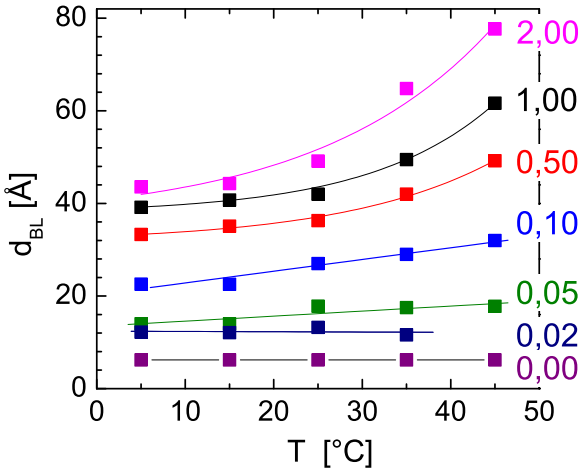

Figure 7.5: Thickness per polyelectrolyte pair (l_{BL}), i.e. total film thickness normalized to the number of bilayers (BL), is plotted as a function of preparation temperature T for different NaCl concentrations in mol/L as indicated. Note that samples prepared from different temperatures and salt concentration may have the same thickness, yet different composition.

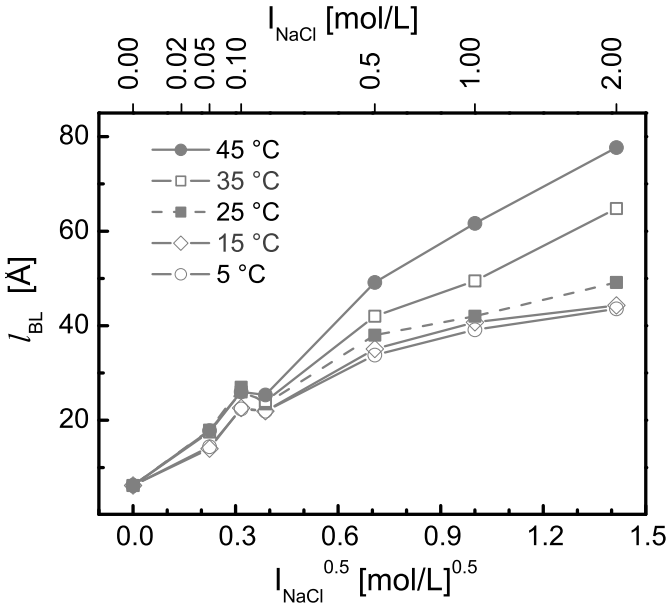

Figure 7.6: Thickness per PAH/PSS pair (l_{BL}) is plotted as a function of square root of NaCl concentration in $(\mathrm{mol/L})^{0.5}$ for the different preparation temperatures as indicated. To avoid confusion, concentration in mol/L is shown above.

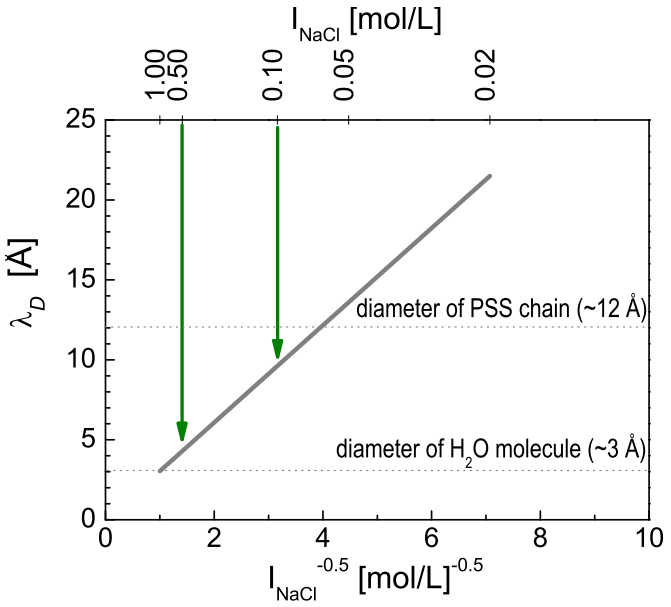

Figure 7.7: Debye screening length λ_D plotted as a function of inverse square root of NaCl concentration. Here dotted lines indicate diameter of PSS chain and water molecule, correspondingly. The green arrows indicate Debye values for 0.1 mol/L and 0.5 mol/L.

If thickness per polyelectrolyte layer pair (l_{BL}), defined as ratio of total film thickness and number of polyelectrolyte bilayers (BL), is plotted as a function of the square root of the salt concentration, which is proportional to the inverse Debye length (cf. Fig. 7.6), one observes

a roughly linear increase of the thickness, which is in agreement with previously published results [Lösche1998], [Steitz2000]. Below 25^0 C, the temperature effect on bilayer thickness of PEMs is rather weak, then it gets more pronounced for higher salt concentration, exceeding 0.1 mol/L.

The latter effect can be explained by using Debye screening length (λ_D). For monovalent ions, like NaCl $\lambda_D = 3\,\text{Å}/\sqrt{\text{I}}$, where I - ionic strength of the polyelectrolyte solution in mol/L [Butt2003]. Without salt the Debye screening length is large and by increasing the salt concentration it decreases, therefore one can assume that more polyelectrolytes adsorb onto the surface. Debye screening length for the solvent conditions of 1 mol/L amounts to 3 Å, a length, which corresponds to the diameter of a water molecule; 0,05 mol/L corresponds to the Debye screening length of 13 Å, a value that is similar to the diameter of a PSS chain (12 Å) [Ahrens1997] (shown by dotted lines in Fig. 7.7). Therefore, one can conclude that the secondary interactions are short–ranged and the characteristic range is of the same order of magnitude as the molecular dimensions.

7.2.2 Influence of Temperature during Formation of PEMs

The block samples with p_5d_5 architecture are used to obtain information about the roughness of the internal interface and amount of water bound to PEMs. The p_5d_5 samples are prepared at 15^0 C, 35^0 C and 50^0 C from 3 mmol/L polyelectrolyte solution in presence of 1 mol/L NaCl (temperature was kept constant during the preparation). The Fresnel normalized reflectivity data, obtained by measuring samples in dry (0% r.h.) conditions are shown in Fig. 7.8. One can see that minima of the same order are shifting to the lower Q_z with increasing temperature of deposition solution that indicates film thickening. This result agrees with the dependence shown earlier in [Büscher2002]. The influence of preparation temperature on internal properties of the film that consists of two blocks is investigated. Here one of the blocks is made of deuterated PSS_d that provides high contrast in reflectivity signal. The scattering length density profiles that arise from Si/p_5, p_5/d_5 and d_5/air interfaces are shown in Fig. 7.9. As one can see, the thickness increase on increase of the deposition temperature is more pronounced for deuterated blocks than for protonated ones, indicating non–linear growth of PAH/PSS system at higher temperatures or at least different growth behaviour of the first five layers. Indeed, thickness ratio of deuterated and protonated blocks is changing from 1.1 for the sample prepared from 15^0 C, to 1.2 for 35^0 C and 1.7 for 50^0 C. This finding is directly correlated to the zone model for polyelectrolyte multilayer film growth first introduced by G. Ladam [Ladam2000].

The amount of H_2O molecules bound to PAH/PSS (PAH/PSS_d) monomer pair at 0% r.h. is calculated from the scattering length density values of protonated and deuterated parts according to eq. 6.3 (introduced in the previous chapter) and is indicated in Fig. 7.9. As one can see, almost no water is found in the protonated part and about 1.5 water molecules in the deuterated one. This finding corresponds to the results shown in previous chapter (cf. Fig. 6.20). It seems that amount of water bound to polyelectrolyte monomer pair is independent on the preparation temperature of polyelectrolyte solution.

The internal roughness σ_{int} between adjacent blocks is getting higher on temperature increase (cf. Fig. 7.9). For the samples prepared at 15^0 C and 35^0 C internal roughness correspond to $\sigma_{int} = 9.3$ Å and 10.5 Å, accordingly. Yet, for 50^0 C σ_{int} is found to be equal to 27 Å. To support these results, additional sample was prepared at 40^0 C (cf. Fig. 7.10).

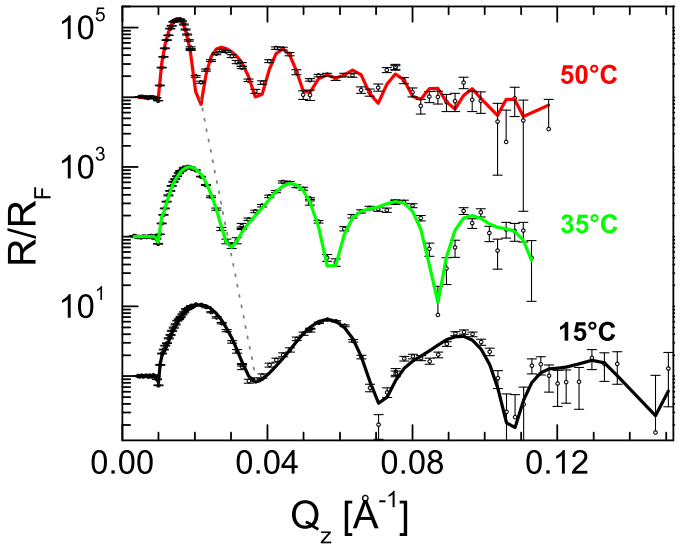

Figure 7.8: Normalized neutron reflectivity curves of p_5d_5 architecture prepared at 15^0 C, 35^0 C and 50^0 C in presence of 1 mol/L NaCl and measured in dry (0% r.h.) conditions. Straight lines are fits; dashed line connect interference minima of the same order and indicate film thickening on temperature increase. For clarity the curves are shifted by 2 orders of magnitude relative to R/R_F axis.

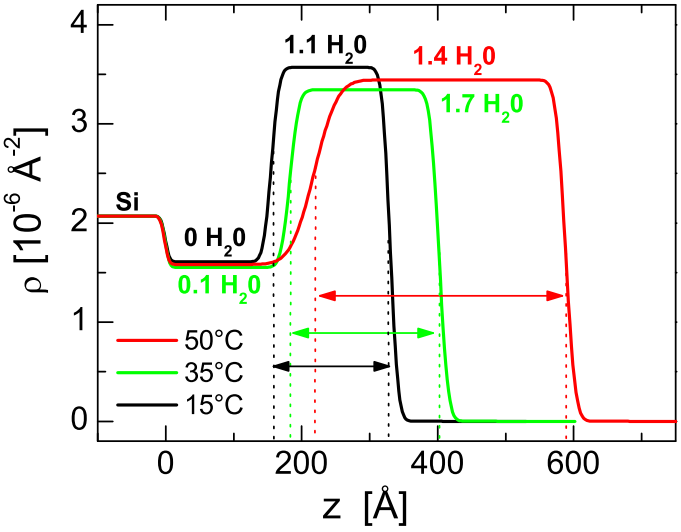

Figure 7.9: The SLD profiles derived from the measurements in Fig. 7.8. Left to right: silicon, p_5 block smeared out by internal roughness and d_5 block with adjacent film/air interface. Amount of H_2O per PAH/PSS (PAH/PSS_d) pair is shown for protonated and deuterated blocks of each sample, respectively. The arrows indicate length (thickness) of the respective deuterated blocks. Note that z – scale is set to zero at Si/p_5 interface, therefore thickness of the protonated block is denoted by the first dotted line of the respective color.

In Fig. 7.10, previously shown reflectivity data for sample adsorbed from 50^0 C is repeated to demonstrate increase of the film thickness on temperature rise.

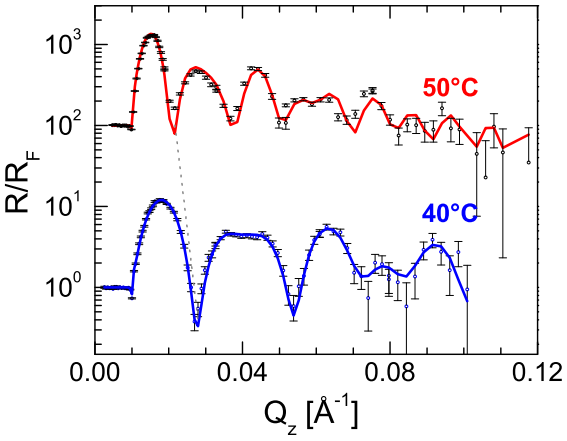

Figure 7.10: Normalized neutron reflectivity curves of p_5d_5 architecture prepared at 40^0 C and 50^0 C in presence of 1 mol/L NaCl and measured at 0% r.h. Straight lines are fits; dashed line connects interference minima of the same order and indicates film thickening on temperature increase. For clarity the curves are shifted by 2 orders of magnitude relative to R/R_F axis.

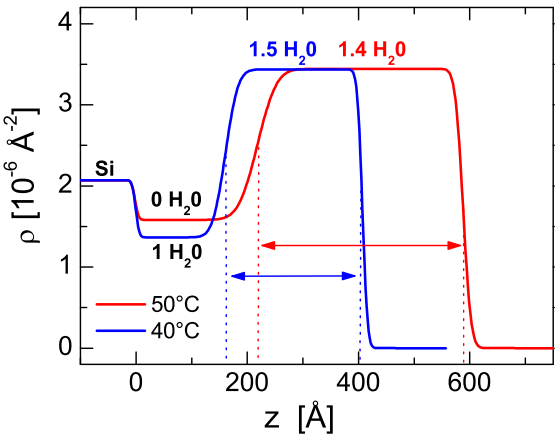

Figure 7.11: The SLD profiles derived from the measurements in Fig. 7.10. Left to right: Si, p_5 block smeared out by internal roughness and d_5 block with adjacent PEM/air interface. Amount of H_2O per monomer pair is shown for p_5 and d_5 blocks of each sample, respectively. The arrows indicate thickness of the respective deuterated blocks. At Si/p_5 interface z – scale is set to zero.

p_5d_5	15^0 C	35^0 C	40^0 C	50^0 C
protonated block				
l_p [Å]	156.9	183.7	161.3	220.1
ρ_p [10^{-6} Å^{-2}]	1.603	1.556	1.366	1.581
$l_{BL,p}$ [Å]	31.4	36.7	32.3	44.0
n_{H_2O}	0	0	1.0	0
deuterated block				
l_d [Å]	174.3	219.3	246.3	369.6
ρ_d [10^{-6} Å^{-2}]	3.572	3.346	3.433	3.441
$l_{BL,d}$ [Å]	34.9	43.9	49.3	73.9
n_{H_2O}	1.1	1.7	1.5	1.4
σ_{sub} [Å]	5.0	5.0	5.0	5.0
σ_{int} [Å]	12.0	12.7	18.0	27.0
σ_{air} [Å]	8.3	9.7	7.3	11.3
$\sigma_{int}/\sigma_{air}$	1.4	1.3	2.5	2.4
$\sigma_{int}/l_{BL,d}$	0.34	0.29	0.36	0.36

Table 7.1: Parameters of the p_5d_5 film prepared in presence of 1 mol/L NaCl at different temperatures indicated. Data are deduced from the fits to the measurements shown in Fig. 7.10 and the corresponding SLD profiles in Fig. 7.9. Here length of the protonated blocks (l_p) and deuterated blocks (l_d), scattering length density (ρ_p and ρ_d), bilayer thickness for each block ($l_{BL,p}$, $l_{BL,d}$) and amount of water (n_{H_2O}) calculated from SLD according to eq. 6.3 are presented.

As one can see (cf. Fig. 7.11), amount of water in protonated part is found to be higher (1 H_2O molecule) for sample adsorbed from 40^0 C however, the value for deuterated part (1.5 H_2O molecules) is similar to the values obtained for the other temperatures. Also, internal roughness of p_5/d_5 interface (σ_{int} = 18.0 Å) is between the values obtained for the samples prepared from 35^0 C and 50^0 C. Table 7.1 contains all parameters of the p_5d_5 films prepared from 1 mol/L NaCl at different temperatures. The behaviour of length (thickness) ratio of deuterated and protonated blocks for all investigated temperatures is presented in Fig. 7.12. The ratio l_d/l_p grows more rapidly with temperature for samples prepared at T> 35^0 C. Concurrently, the interfacial roughness between adjacent blocks σ_{int} increases on temperature rise. Intriguing, that the internal roughness amounts about 34% of the thickness of a PAH/PSS_d layer pair for all preparation temperatures.

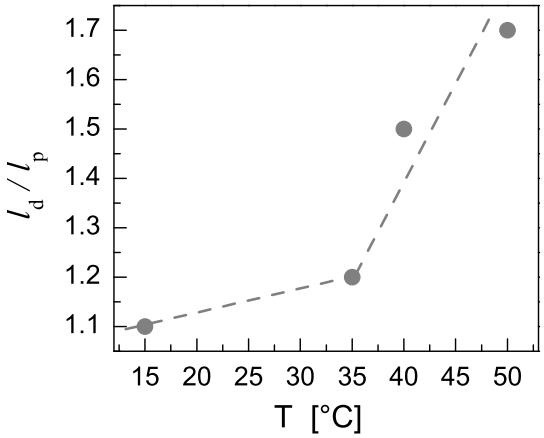

Figure 7.12: Length ratio of deuterated and protonated blocks (outer to inner) for p_5d_5 films prepared in presence of 1 mol/L NaCl is plotted against preparation temperature. Dotted line is guide to the eye.

7.2.3 Influence of Temperature after Preparation of PEMs

To find out if temperature effect on thickness and composition of polyelectrolyte multilayer films is general or influenced by preparation temperature only, temperature–dependent treatment after sample preparation was performed. Two sample architectures (superlattice and block structure) are investigated with neutron reflectivity at solid/air and solid/liquid interfaces.

Temperature–Dependent Post–treatment: Superstructure

The polyelectrolyte multilayer films with superstructure architecture consisting of one deuterated PSS_d layer sandwiched between four protonated PSS layers are used for these experiments. For samples prepared from deposition temperature between 15^0 C and 55^0 C, PEM consist of 19 layer pairs: PEI[(PSS/PAH)$_3$/PSS_d/PAH]$_4$(PSS/PAH)$_3$ or in short form $(p_3d)_4\,p_3$. For samples prepared at 5^0 C and 60^0 C multilayer films consist of 16 bilayers: PEI/(PSS/PAH)$_3$/[PSS_d/(PAH/PSS)$_3$/PAH]$_3$$PSS_d$ or in short form $(p_3d)_4$. All films are adsorbed from 3 mmol/L polyelectrolyte solution and measured in dry conditions (0% r.h.).

To screen electrostatics high salt (1 mol/L) concentrated solutions are used. The Fresnel normalized neutron reflectivity curves of polyelectrolyte multilayers prepared from 1 mol/L NaCl and different preparation temperatures are shown in Fig. 7.13. Here the Kiessig oscillations that measure the over–all film thickness as well as two Bragg peaks (due to an internal superstructure) can be seen. However, special emphasis is given to the analysis of superstructure sample prepared at 5^0 C and heated afterwards. A film prepared at 5^0 C (cf. Fig. 7.13) was immersed for 4 hours in 60^0 C aqueous salt solution same as used for preparation (cf. Fig. 7.13, bottom). As one can see in Fig. 7.13, the Kiessig oscillations are less pronounced for the heated sample and also 2^{nd} Bragg peak disappear. However, the total film thickness is almost the same in both cases. This indicate changes in PEM composition and pronounced interpenetration between the layers in accordance with [Gopinadhan2005].

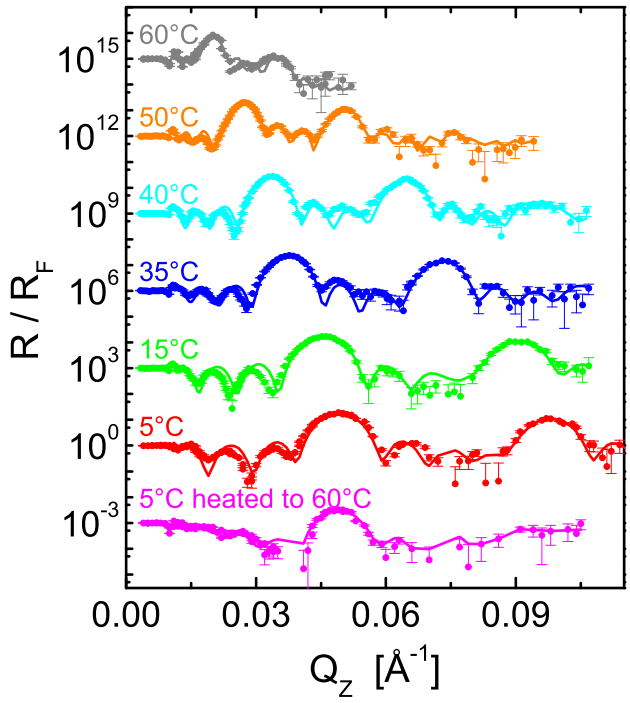

Figure 7.13: Normalized neutron reflectivity curves of PEMs prepared from 1 mol/L NaCl solution at preparation temperatures indicated. For temperature between 15 and 55^0 C the film PEI$[(PSS/PAH)_3/PSS_d/PAH]_4(PSS/PAH)_3$ consists of 19 BL; for 5^0 C and 60^0 C film is ending with PSS_d and consists of 16 BL: PEI$/(PSS/PAH)_3/[PSS_d/(PAH/PSS)_3/PAH]_3PSS_d$. Note that for sample prepared at 5^0 C two measurements are shown: initial (red curve) and after 4 hours heating to 60^0 C in 1 mol/L NaCl solution (magenta curve). For clarity all curves are shifted by three orders of magnitude relative to R/R_F axis.

The changes in PEM composition are directly visualized by scattering length density (SLD) profiles (cf. Fig. 7.14). Using fit assumptions presented in [Gopinadhan2007b] one obtains that less water is incorporated at higher temperature. Since most of the fits shown in Fig. 7.13 are performed by M. Gopinadhan and presented in his doctoral thesis [Gopinadhan2007a], they will not be discussed here in details. Intriguing, that for both samples, initially prepared at 60^0 C and heated to 60^0 C, water amount per PAH/PSS pair is found to

be identical (almost no water in the layer). Decrease in water uptake was also found by heat–treatment of ionomer membranes [Parka2005]. Yet, these results have not been confirmed by the block architecture prepared at higher temperatures (cf. section 7.2.3). Generally, such a low water content can be explained by deterioration of solvent–solute interactions on temperature increase. This may changes PEM in two ways during the buildup: on the mesoscopic scale more polymer is deposited in each adsorption step, and on the molecular scale less water is bound and therefore, adsorbed polymer is less hydrated. Also, one can assume that the observed water removal causes film shrinking. As shown in Fig. 7.15 lateral shrinking upon heating leads to break of PEM structure as evidenced by microscope images. One way to explain this fact is to take into account low ability of polyelectrolytes to rearrange under the stress (heating in salt solution in this case), that leads to structure tension and eventually breaking.

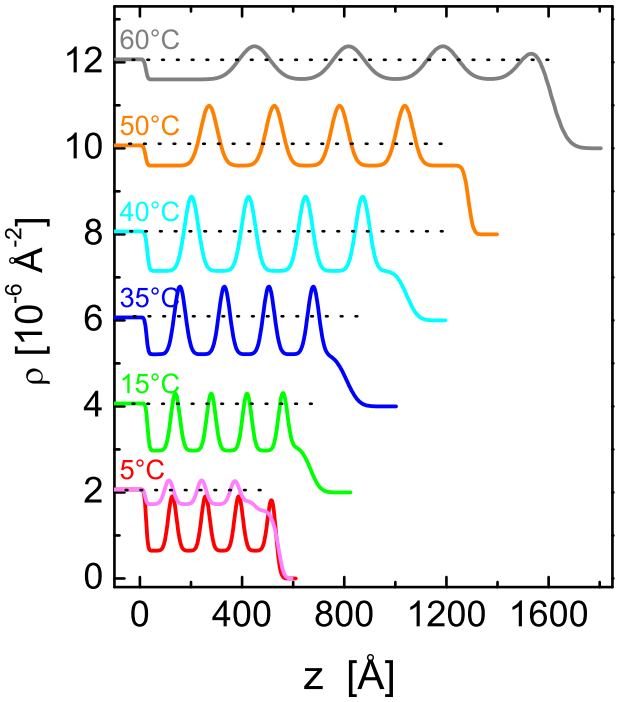

Figure 7.14: The SLD profiles derived from the measurements in Fig. 7.13. For clarity the curves are shifted by two relative to SLD axis. The scattering length density of silicon substrate is indicated (dotted line).

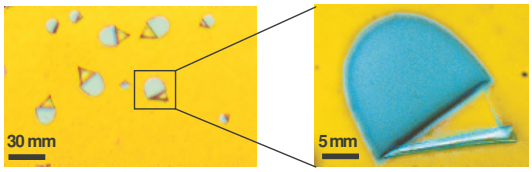

Figure 7.15: Microscope images of the PEI/$(PSS/PAH)_3$/$(PSS_d/(PAH/PSS)_3/PAH)_3PSS_d$ film prepared at 5^0 C and heated afterwards. Due to interference of thin layers the film appears yellow, the silicon substrate – cyan.

Temperature–Dependent Post–treatment: Block Structure

A protonated–deuterated PEI/(PSS/PAH)$_4$/PSS/(PAH/PSS$_d$)$_5$ or in short form p_5d_5 film was adsorbed onto one side polished silicon block ($\sigma_{sub} < 6$Å) at 15^0 C from 3 mmol/L polyelectrolyte solution in presence of 1 mol/L NaCl. Freshly prepared and dried sample was exposed to a close bath filled with liquid D_2O and measured against D_2O (therefore reflectivity curves look different to those shown earlier). Schematic of neutron reflectivity experiment is shown in Fig. 7.16.

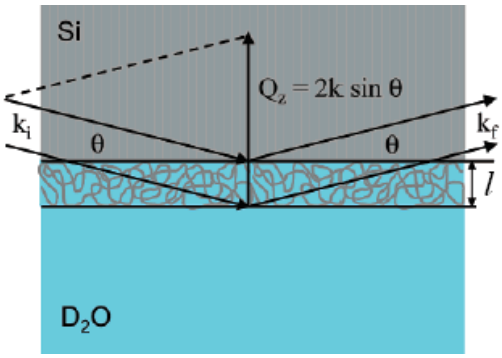

Figure 7.16: Scattering geometry of the neutron reflectivity experiment in solid/liquid interface. Here, in contrast to solid/air interface considered before, the incident neutron beam access the polymer/water interface through the silicon block. The respective reflectivity signal arises from Si/PEM, PEM/D_2O and additional internal interface, due to partial deuteration of the film (not shown here). Thickness l of the PEM is indicated. The picture is adapted from R. Steitz et. al. *Langmuir* (2003).

First, D_2O solution was heated for half an hour to 23^0 C and the sample was measured afterwards. During the measurement, the temperature of the solution remained constant. The resulting reflectivity signal normalized to Fresnel reflectivity of ideally sharp interface is shown in Fig. 7.17, curve 1. After recording the reflectivity signal, the sample was heated further: first to 40^0 C (curve 2) and then to 55^0 C (curve 3) for a half an hour each. As one can see, heating to 55^0 C results in strong reduction of the Kiessig oscillations in the reflectivity signal, therefore sample was cooled back to 23^0 C. After drying for 12 h in ambient conditions the measurement was repeated (curve 4). The reflectivity signal for the curve 4 is obviously more pronounced than for the measurement performed at 55^0 C (curve 3), that indicates partial reversibility of the structural changes in PEM.

In the beginning of the experiment (curves 1, 2) one can see pronounced Kiessig oscillations that arise from Si/p_5, p_5/d_5 and d_5/D_2O interfaces. The p_5d_5 multilayer film is parameterized with 2 box model for the first three curves and with domain model for the curve 4. Such a choice of parametrization is attributed to the changes in PEM structure that occur after heating the sample to 55^0 C and subsequent cooling down. As one can see, the reflectivity signal from curves 1 and 2 in Fig. 7.17, as well as corresponding SLD profiles (cf. Fig. 7.18) are almost the same, while the oscillations of the curve 3 are strongly damped out by high internal roughness of the film suggesting increased interpenetration between the layers.

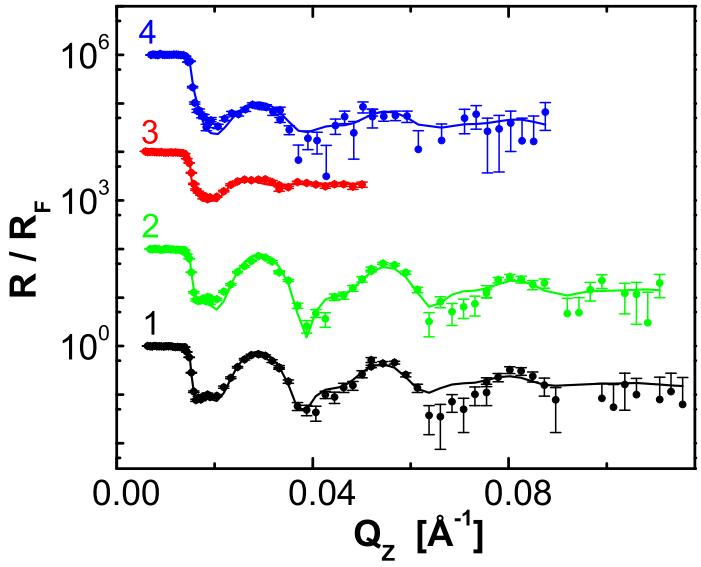

Figure 7.17: Normalized neutron reflectivity curves of p_5d_5 architecture prepared at 15^0 C and 1 mol/L NaCl on Si block. Accordingly to Fig. 7.16 the film was measured at Si/D_2O interface. Here numbers above the curves represent stages in the sequence of the experiments: (1) - after keeping sample for half an hour in 1 mol/L NaCl solution heated to 23^0 C, (2) - to 40^0 C, (3) - to 55^0 C, (4) - cooling back to 23^0 C, and measuring at 23^0 C after drying the sample for 12 hours in ambient conditions. Straight lines are fits. For clarity the curves are shifted by two orders of magnitude vertically.

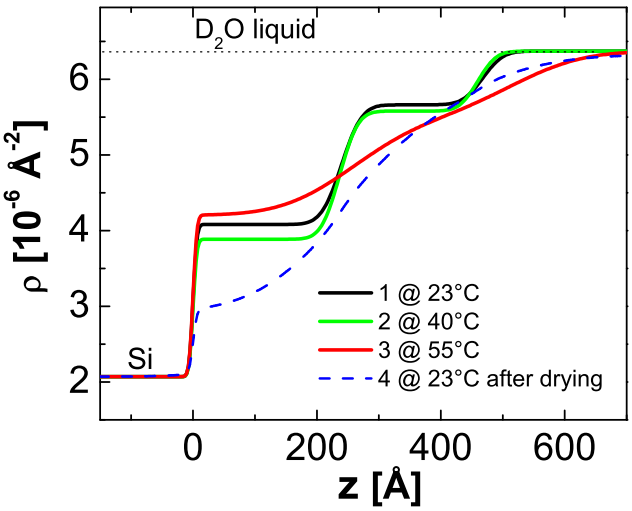

Figure 7.18: The SLD profiles derived from the measurements in Fig. 7.17 are color coded according to the reflectivity curves. Left to right: silicon, p_5 block, d_5 block with higher SLD due to presence of PSS_d and adjacent d_5/D_2O interface.

The fitting routine for the curve 3 with the same parametrization as for curves 1 and 2 (cf. Table 7.2) shows additional increase in total thickness by 10%, where the SLD for both

boxes are nearly constant in comparison to the curve 2. Additionally, the lateral shrinking of the PEM coverage along the edges (about 10%) is visually observed, see Fig. 7.19. Thus, one can conclude that volume of the PEM is constant and no loss of material occur.

box	l [Å]	ρ [Å^{-2}]	σ [Å]
curve 1			
box 1	l_1=234.1	$\rho_p = 3.83 \cdot 10^{-6}$	σ_{int}=17.8
box 2	l_2=l_1	$\rho_d = 5.47 \cdot 10^{-6}$	σ_{out}=49.1
curve 2			
box 1	l_1=231.9	$\rho_p = 3.89 \cdot 10^{-6}$	σ_{int}=19.3
box 2	l_2=l_1	$\rho_d = 5.43 \cdot 10^{-6}$	σ_{out}=44.4
curve3			
box 1	l_1=257.9	$\rho_p = 4.19 \cdot 10^{-6}$	σ_{int}=89.7
box 2	l_2=l_1	$\rho_d = 5.48 \cdot 10^{-6}$	σ_{out}=σ_{int}

Table 7.2: Parameters of the p_5d_5 film derived from the fits to the measurements shown in Fig. 7.17 and the corresponding SLD profiles in Fig. 7.18 according to the used box model. Here the values for the thickness l of protonated and deuterated parts of the film, scattering length density ρ, roughnesses of internal interface σ_{int} and film/D_2O interface σ_{out} are shown for the first 3 curves. Based on X–ray measurements, roughness of the substrate adjacent layer (Si/p_5) is set to 5 Å. SLD of D_2O is set to the calculated value: $\rho_{D_20} = 6.37 \cdot 10^{-6}$ [Å^{-2}].

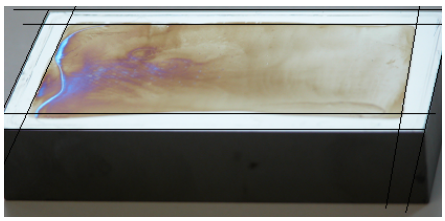

Figure 7.19: Photo of Si block ($8 \times 5 \times 1.5$ cm) after temperature treatment. The loss of the initial shape of the film is indicated by black lines. Initially, surface of silicon block was fully covered. Also, optical inhomogeneity of the film can be seen.

To prove the reversibility of the structural changes, the sample was dried for 12 hours and measured once more at 23^0 C (cf. Fig. 7.17, curve 4). Qualitatively, curve 4 looks similar to the curve 1 except much higher roughness and reduced reflected intensity, suggesting that only a small part of the sample reflect neutrons in the same way like for curve 1. Therefore, domain model that allows incoherent overlap of the reflectivity signals was used. The resulting scattering length density profile is shown in Fig. 7.20 by blue solid line. It is a composition of two weighted SLD profiles indicated by dashed lines: one (brown) with similar parameters like for curve 1 in Fig. 7.18, the other one (gray) for rough interface. According to the fit, area fraction that reflects initial signal is about 10% that corresponds to the visual observations shown above.

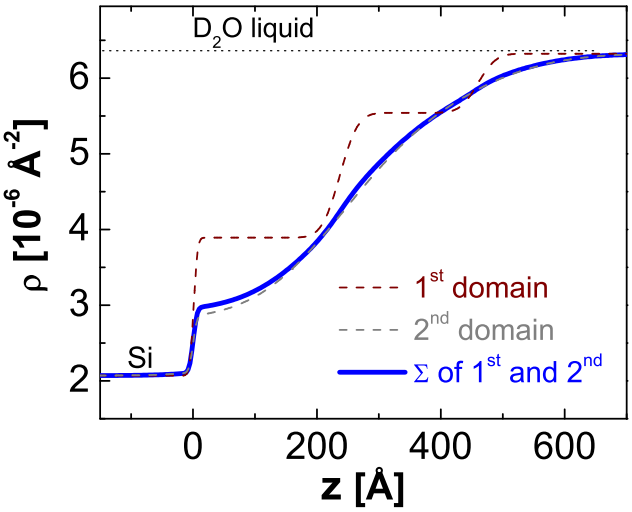

Figure 7.20: The SLD profile derived from the curve 4 in Fig. 7.17 is calculated in frames of the model, which allows incoherent overlap of reflectivity signals of two domains. The resulting SLD (shown by blue solid line here and by dashed line in Fig. 7.18) consists of incoherent contribution from the curve 1 (brown dashed line) and additional rough interface (gray dashed line).

Since no neutron reflectivity measurements were done at 0% r.h. in the beginning of the experiment, it is not possible to determine the amount of tightly bound H_2O inside the layer directly from the SLD. Also, swelling behaviour (thickness increase) is not easy to quantify due to an unknown content of D_2O and H_2O inside the polyelectrolyte multilayer ($x\,V_{H_2O}+y\,V_{D_2O}$). However, one can recalculate amount of water, both H_2O and D_2O using the value of total film thickness obtained from X–ray measurements (not shown here) that were performed immediately after the sample preparation at ambient conditions (25% r.h.). The film thickness first was normalized to 0% r.h. assuming linear swelling of the layer as it was shown in the previous chapter (cf. Fig. 6.6).

When the sample was exposed to D_2O solution, multilayer film swelled by ca. 33% (vol.) in comparison with 0% r.h. This observation is in agrement with our previous results, that allows us to conclude that the swelling of the PEM in 100% vapor and in liquid water is the same irrespective to H_2O or D_2O. Also, assuming full deuteration of PAH after exposure to 100% D_2O (exchange of all 3 protons in PAH monomer is shown in previous chapter) and taking into account swelling by 33%, one obtains 3.5 H_2O molecules in dry state ($n_{H_2O,\,dry}$=3.5), that is consistent with the expected literature value [Gopinadhan2007b].

In general, obtained results suggest that heating of PEM leads either to breaking of the film structure or to lateral shrinking accompanied by enormous internal roughness increase. It can be attributed to hydrophobic interactions, since one may assume that heating of the sample in the solution enables entropically favorable conformations of polyelectrolytes in multilayered film.

The quantitative estimation of bound water in heated PEM seems to be rather difficult. However, qualitative analysis gives information about loss of water by heating the sample in the layer adjacent to substrate. Also, structural changes that arise upon heating seem to be reversible at least on macroscale.

7.3 Effect of Ions: Hofmeister Series

In order to gain a better understanding of internal processes during formation of PEMs, temperature and type of salt counterions (cations and anions) in preparation solutions are varied. The superstructure samples consisting of one deuterated (PAH/PSS_d) layer sandwiched between several protonated (PAH/PSS) layers are prepared with 1 mol/L concentration of salt and investigated by neutron reflectivity in solid/air interface at 0% relative humidity. The $(p_3d)_4$ architecture is used, except for the samples prepared from NaCl at 15^0 C and 35^0 C that have 3 additional protonated bilayers on top: $(p_3d)_4\, p_3$. The latter measurements were already shown in section 7.2.3. Selectively deuterated polyanion layers lead to at least two superstructure interference (Bragg) peaks, allowing for quantification of structural parameters.

Fig. 7.21 shows a set of neutron reflectivity measurements for different cations presented according to the Hofmeister series (Na^+, K^+, Cs^+). The Bragg peaks, which appear due to repeated multilayer structure (regular pattern of deuterated layers), are clearly visible on the linear scale. Thus, one can observe shift of the peaks to the low Q_z values with increasing preparation temperature, which refer to the larger film thickness at higher temperatures for each investigated salt. One the other hand, the position of the peak is independent on the type of salt (for the same temperature), indicating identical film thickness for cation series of investigated salt ions.

Neutron measurements for anion Hofmeister series ($COOH^-$, Cl^-, Br^-) at different preparation temperatures are shown in Fig. 7.22. As one can see, the position of the Bragg peak for PEMs adsorbed from 1 mol/L NaBr is different to one from 1 mol/L NaCOOH prepared at the same temperature. Therefore, films adsorbed from polyelectrolyte solution in presence of NaBr are much thicker than those from NaCOOH. This observation is in agreement with the finding that thickness behaviour for anions follow the Hofmeister series for PSS/PDADMA multilayer system [Salomäki2004b]. Same as for cations, on increase of the preparation temperature, the Bragg peaks shift to lower Q_z values that indicates an increase of the PEM thickness for each investigated salt. The values of the film thickness normalized to the number of bilayers (l_{BL}) for investigated anions are shown in Table 7.3. The behaviour of the thickness per polyelectrolyte bilayer for both, cations and anions as function of preparation temperature can be seen in Fig. 7.23. Here, additional measurement points for PEMs adsorbed from 1 mol/L NaCl and KCl are included to demonstrate thickness increase at higher temperatures. As one can see, rise in the preparation temperature from 5^0 C to 60^0 C causes an increase in the thickness per polyelectrolyte bilayer l_{BL} from 33 Å to 92 Å for PEMs adsorbed from 1 mol/L NaCl. Such strong temperature dependence can be attributed to the hydrophobic effect.

In Fig. 7.24 ratio of the internal roughness σ_{int} and average bilayer thickness (l_{BL}) is plotted as a function of deposition temperature for cations and anions. The increase of $\sigma_{int}/l_{\mathrm{BL}}$ with the temperature can be seen by decline of Bragg peaks. Such behaviour is pronounced for NaCl and KCL. Therefore, it was concluded [Gopinadhan2007b] that interpenetration between the layers is temperature dependent for the investigated system. However, the fact that ratio of the internal roughness and average bilayer thickness decrease for sample adsorbed 1 mol/L CsCl suggest that it is needed to rethink the assumptions that have been made for superstructure samples. Thus, the fit assumptions like constant internal roughness and bilayer thickness (especially in precursor layer) do not fulfill high temperature prepa-

ration requirements as shown by later experiments with block samples. Full set of neutron reflectivity curves for NaCl and KCL is shown in Fig. 7.25. Here the heights of the Bragg peaks are visibly changing with a preparation temperature indicating increase of internal roughness between adjacent interfaces.

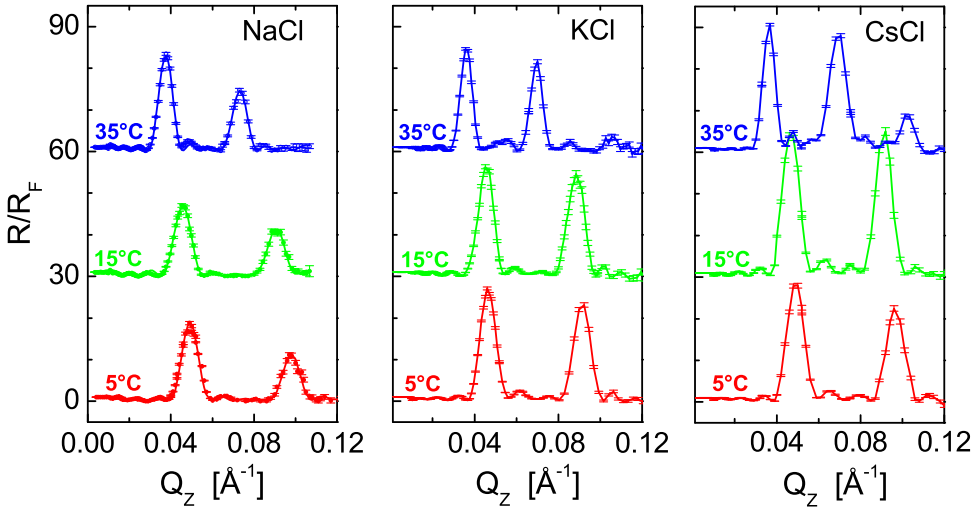

Figure 7.21: Normalized neutron reflectivity curves for PEMs adsorbed from 1 mol/L XCl at temperatures indicated and measured at 0% r.h. Left to right: NaCl, KCl, CsCl according to the Hofmeister cation series. The $(p_3d)_4$ architecture is used, except for the samples prepared from NaCl at 15^0 C and 35^0 C that have additional protonated layers on top: $(p_3d)_4\, p_3$. For clarity the curves are shifted by 30 units vertically.

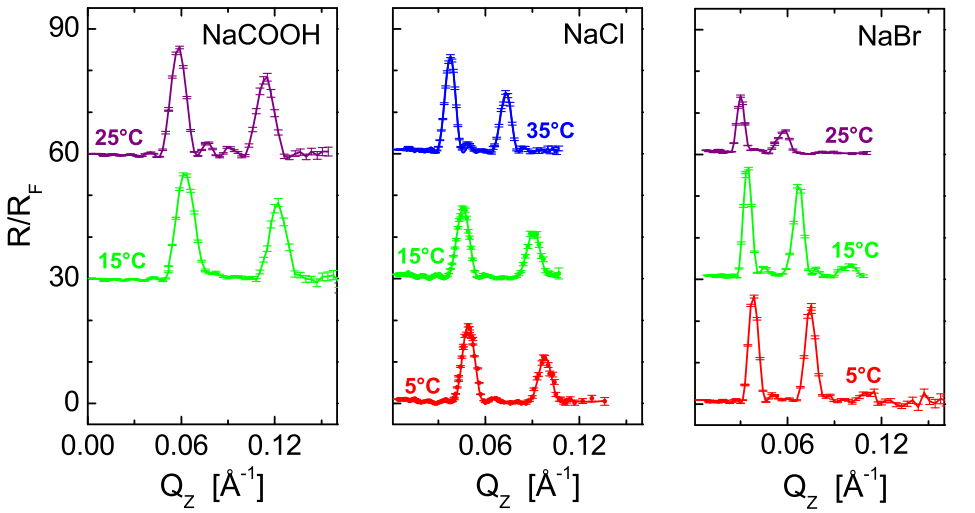

Figure 7.22: Normalized neutron reflectivity curves for PEMs adsorbed from 1 mol/L NaX at temperatures indicated and measured at 0% r.h. Left to right: NaCOOH, NaCl, NaBr according to the Hofmeister anion series. The $(p_3d)_4$ architecture is used, except for the samples prepared from NaCl at 15^0 C and 35^0 C: $(p_3d)_4\, p_3$. For clarity the curves are shifted by 30 units vertically.

T [^{0} C]	$l_{\mathrm{BL,\,NaCOOH}}$ [Å]	$l_{\mathrm{BL,\,NaCl}}$ [Å]	$l_{\mathrm{BL,\,NaBr}}$ [Å]
5	–	33	42.8
15	25.7	34.5	47.6
25	27.7	–	54.8
35	–	44.1	–

Table 7.3: Bilayer thickness for anion series of ions at preparation temperature indicated is derived from the measurements of superstructure samples shown in Fig. 7.22.

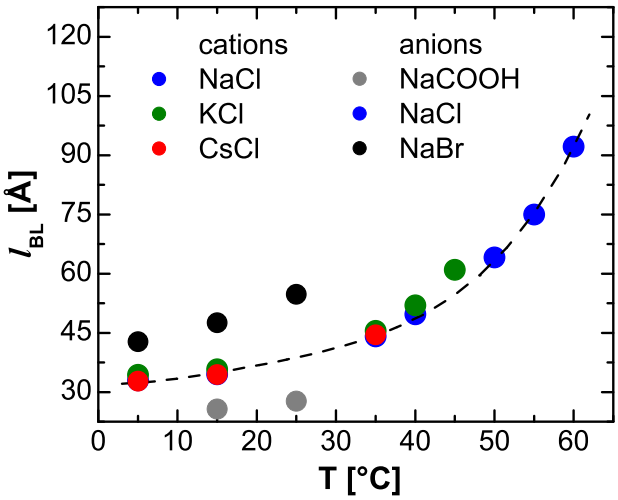

Figure 7.23: Bilayer thickness l_{BL} derived from the measurements shown in Fig. 7.21 and Fig. 7.22 is plotted against preparation temperature for series of cations and anions. To show trend of the bilayer thickness, parameters obtained from the measurements for NaCl and KCl prepared at T$>35^0$ C are included. Full set of measurements for NaCl and KCl is shown in Fig. 7.25.

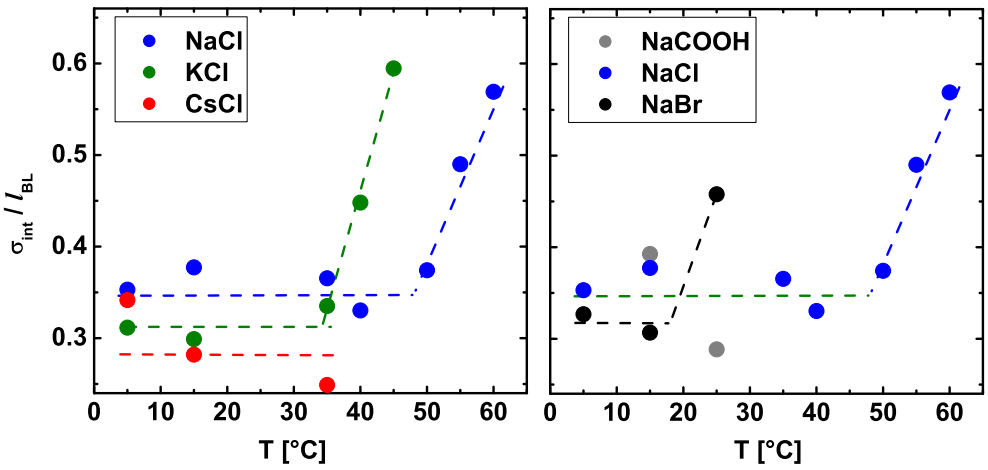

Figure 7.24: Ratio of the internal roughness σ_{int} and average bilayer thickness (l_{BL}) vs. deposition temperature is shown for superstructure samples (cf. Fig. 7.21, 7.22, 7.23).

The height of the 1st superstructure peak is inversely proportional to the amount of bound water, assuming that the water volume fraction is constant throughout the film [Gopinadhan2007b]. One can notice (cf. Fig. 7.21, 7.22, 7.25) that the heights of the Bragg peaks seems to follow the Hofmeister series (except for $HCOO^-$), suggesting different amount of water in the PEM [Ivanova2007]. However, this observation is complex to interpret due to ambiguous parametrization of thin deuterated layers (thin relatively to the roughness of the adjacent interface) sandwiched between thick protonated ones. The scattering length density profile of these thin deuterated layers resembles a Gaussian shape, which one can get either with a large height and a large width or with a small height and a small width (the height of the Gaussian is proportional to the scattering length density of the film and its width to the roughness of the internal interface). Also, the fits appear to be more sensitive to the height of Bragg peaks then to the Kissieg fringes.

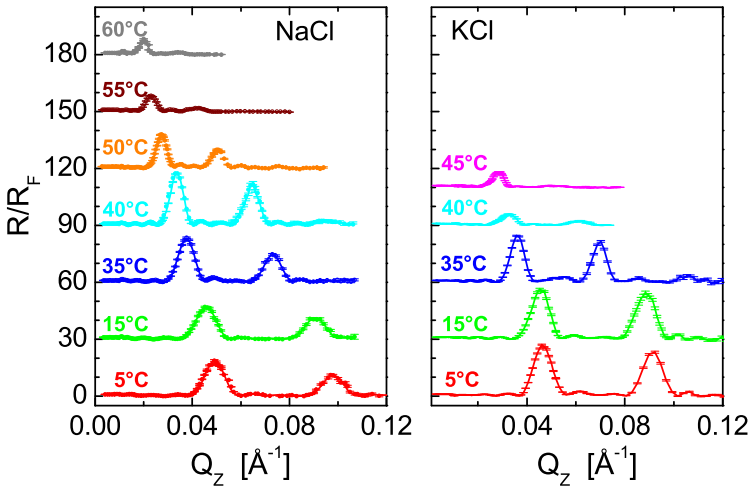

Figure 7.25: Normalized neutron reflectivity curves for PEMs adsorbed from 1 mol/L NaCl and KCl at temperatures indicated and measured at 0% r.h. For clarity the curves are shifted by 30 units vertically.

To avoid ambiguous parametrization of the layers and to find out if the amount of water in the layers is indeed depends on the type of salt, new block architecture consisting of 5 deuterated and 5 protonated blocks (d_5p_5) have been used. The samples are prepared from different types of salts at constant temperature (15^0 C). Measurements are shown in Fig. 7.26 and corresponding SLD profiles in Fig. 7.27. Using simple two box parametrization one can obtain water amount directly from the values of scattering length density of deuterated and protonated blocks respectively (cf. Table 7.4 and eq. 6.3).

In contrast to the assumptions based on the superstructure measurements, the amount of water appears to be the same (1 to 2 H_2O molecules per PAH/PSS and PAH/PSSd pair) for all investigated salts at 0% r.h., although values for bilayer thickness corresponds to the values obtained with superstructure samples. Thus, for all used cations average film thickness per polyelectrolyte bilayer seems to be the same (about 33 Å from superstructure samples and 35 Å from block samples) and increases for anions according to the Hofmeister series: $HCOO^- < Cl^- < Br^-$ (from 26 Å to 43–48 Å).

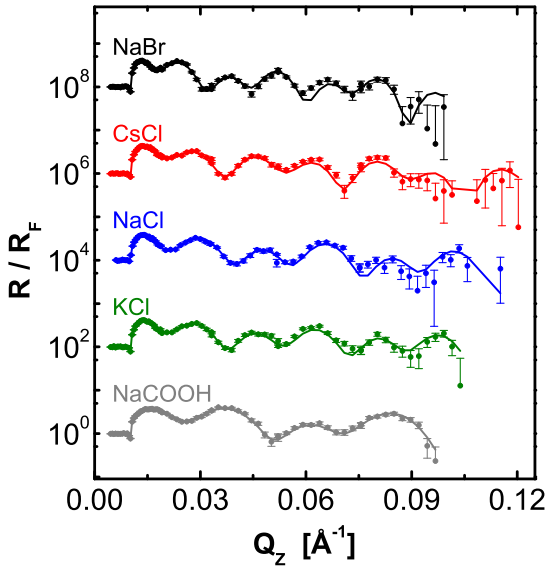

Figure 7.26: Normalized neutron reflectivity curves of d_5p_5 architecture prepared at 15^0 C in presence of 1 mol/L salt indicated and measured in 0% r.h. Straight lines are fits. For clarity the curves are shifted by 2 orders of magnitude relative to R/R_F axis.

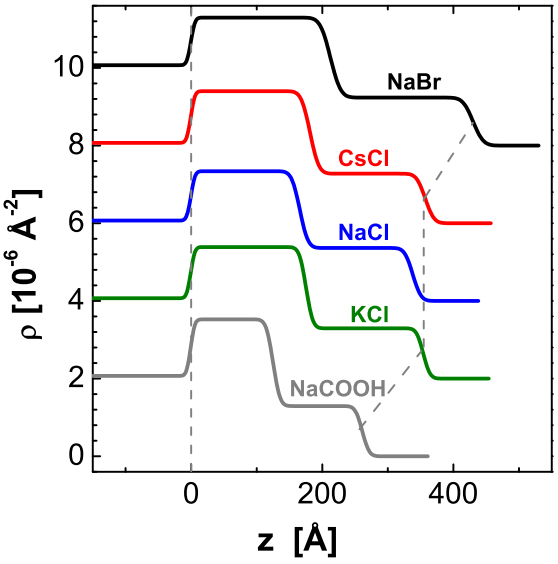

Figure 7.27: The SLD profiles derived from the measurements in Fig. 7.26. Left to right: silicon, d_5 and p_5 blocks. Increase of the film thickness for anions (and constant value for cations) is shown by gray dashed line. For clarity the curves are shifted by two relative to SLD axis.

d_5p_5	NaCOOH	KCl	NaCl	CsCl	NaBr
protonated block					
l_p [Å]	125.7	178.7	172.3	175.7	217.6
ρ_p [10^{-6} Å^{-2}]	1.292	1.294	1.363	1.276	1.235
$l_{BL,p}$ [Å]	25.1	35.7	34.5	35.1	43.5
n_{H_2O}	1.5	1.5	1.1	1.6	1.8
deuterated block					
l_d [Å]	136.0	175.9	166.0	181.9	212.7
ρ_d [10^{-6} Å^{-2}]	3.522	3.384	3.337	3.398	3.294
$l_{BL,d}$ [Å]	27.2	35.2	33.2	36.4	42.5
n_{H_2O}	1.2	1.6	1.7	1.6	1.9
σ_{sub} [Å]	5	5	5	5	5
$\sigma_{air} = \sigma_{int}$ [Å]	8.3	8.1	9.9	10.6	12.3

Table 7.4: Parameters of the d_5p_5 film prepared at 15^0 C in presence of 1 mol/L salts indicated. Data are deduced from the fits to the measurements shown in Fig. 7.26 and the corresponding SLD profiles in Fig. 7.27. Here length of the protonated block (l_p), length of the deuterated block (l_d), corresponding scattering length density (ρ_p and ρ_d), bilayer thickness (l_{BL}) for each block and amount of light water per PAH/PSS monomer pair (n_{H_2O}) calculated from SLD according to eq. 6.3 are presented.

Roughness at the film/air interface appear to be the same like inner roughness and slightly dependent on the kind of salt for anions (cf. Table 7.4). However, the ratio of

internal roughness and average bilayer thickness ($\sigma_{int}/l_{\mathrm{BL}}$) found to be the same (about 0.3) for all PEMs prepared at 15^0 C. Thus, one can conclude that average bilayer thickness and internal roughness for anions are dependent on type of salt for and follow Hofmeister series.

7.4 Discussion

The main findings obtained in this chapter can be summarized as follows:

(i) Experimental observations demonstrate that it is possible to decrease both the range and the amplitude of the electrostatic force by using an ion concentration of at least 0.1 mol/L in the solution. The latter effect enables to suggest that electrostatic attraction between oppositely charged molecules is no longer a driving force for multilayer build–up at higher salt concentrations and one has to take into account additional contributions (secondary interactions). Since the observed onset of the temperature–dependent forces on PEMs growth corresponds to the Debye screening length that exceeds the size of water molecule, but smaller than PSS backbone chain, the secondary interactions are short–ranged and the characteristic range is of the same order of magnitude as the molecular dimensions. Good candidate would be hydrophobic attraction of the chains that increases with the temperature.

(ii) Interpenetration between the layers is found to be temperature dependent for PEMs adsorbed from 1 mol/L salt. For example, the thickness ratio for p_5d_5 block architecture (outer to inner block length) prepared from 1 mol/L NaCl is changing from 1.1 for the sample prepared at 15^0 C, to 1.2 for 35^0 C and 1.7 for 50^0 C. Such behaviour can be attributed to the zone model for polyelectrolyte multilayer film growth. Also, in precursor block adjacent to the substrate no water bound to polyelectrolyte monomer pair is found in dry conditions.

(iii) Heating of PEMs after preparation leads either to breaking of the film structure (in case of PEMs adsorbed on Si wafer) or to lateral shrinking accompanied by enormous internal roughness increase (in case of PEMs on Si block). The shrinking process can be described by two competing attractive forces: increased hydrophobic attraction between layers that increases with temperature and water expulsion during heating. Thus, heating–induced shrinking of microcapsules accompanied by exclusion of hydration water is observed [Déjugnat2007]).

(iv) The PEM bilayer thickness is independent of the type of cations in polyelectrolyte solution and increases on temperature rise. Whereas, it is dependent on type of anions (larger for chaotropic ions), which is in accordance with previously published results [Salomäki2004b]. The length ratio of the blocks for d_5p_5 architecture is found to be the same (about 1.0) for all kind of salts for samples adsorbed at 15^0 C, although the average bilayer thickness is different for anions. The internal roughness of PEMs adsorbed from 1 mol/L salt at 15^0 C amounts about 30% of the average bilayer thickness for all investigated salts (cations and anions). The amount of water in PEMs adsorbed from 1 mol/L seems to be independent on the preparation temperature or type of salt for d_5p_5 architecture (1 to 2 H_2O molecules per PAH/PSS and PAH/PSSd pair at 0% r.h.) in contrast to the previous results with superstructure samples. Important to note that only inversed p_5d_5 architecture turned out to be sensitive to the precursor zone due to low contrast in scattering length density of protonated block and silicon substrate.

7.5 Conclusion

PEM thickness and composition are shown to be strongly influenced by temperature during and after preparation, as well as by concentration and type of salt. It is shown that the secondary interactions such as hydrophobic interactions can overcome electrostatic repulsion and become the major contributing factor for the layer formation and resulting structures. An increase in the preparation temperature increases the thickness per polyelectrolyte layer pair, if the salt concentration in the deposition solution exceeds 0.1 mol/L. Interpenetration between the layers (internal roughness of adjacent interfaces) is temperature dependent and increases on temperature rise. The length of deuterated and protonated blocks for samples adsorbed at 15^0 C is found to be the same for all kind of salts, although the average bilayer thickness is different. The polyelectrolyte bilayer thickness is independent of the kind of salt for cations and increases on increases on rise of deposition temperature. The amount of water in polyelectrolyte multilayers adsorbed from 1 mol/L is found to be independent on the preparation temperature or kind of salt (about 1.5 H_2O molecule per monomer pair at 0% r.h. except for precursor layer, where no bound water is found).

Chapter 8

Tuning of Lateral Structure within the PEMs

8.1 Introduction

The vertical properties of polyelectrolyte multilayers (PEMs) explored by X–ray and neutron reflectivity have been discussed in chapters 6 and 7. However, in spite of the fact that all potential applications (in biotechnology, medicine or industry) require basic understanding of the PEM structure and control in the process of layer formation, less is known about the lateral polymer distribution within an adsorbed multilayer. Multilayered polyelectrolyte films containing various inorganic nanoparticles (e.g. silica, magnetites, gold and semiconductors) have been a subject of intensive research last years.

Metallic nanoparticles have attracted special interest since they exhibit different optical, electrical, magnetic and chemical properties from bulk materials because of their small sizes and large surface to volume ratio [Heilmann2003]. An important feature in the optical response of nanoparticles is the surface plasmon excitation (collective oscillation of the conduction electrons under the irradiation of light), resulting in appearance of a resonance band in the absorption spectra. For silver as well as for other noble metals, the plasmon resonance occurs in the near UV–Visible region, that simplifies experimental optical study of such metal nanoparticles. Therefore, metal–containing polymer films, where metal nanoparticles are used as structural elements of the films attract special interest. The first example of layered nanocomposite films prepared from colloidal metallic particles is shown in [Schmitt1997]. The spatial distribution of the metal particles provides information about lateral film structure and physical properties of the film. The interpenetration of an adsorbed layer into the adjacent film depends on its position during the adsorption process. Furthermore, extensive management of the nanostructure is possible during the deposition process of polymer films with embedded nanoparticles because of the self–assembly due to the charge reversal.

To probe lateral properties of PAH/PSS multilayers, silver nanoparticles embedded into thin poly (allylamine) hydrochloride/ polystyrene sulfonate (PAH/PSS) films are used. An advantage of silver nanoparticles (Ag NPs) is their small size (about 10 nm diameter) similar to, yet slightly larger than a protein molecule. Also, different dependence of the bulk dielectric constant of silver on the wavelength of light [Lide2003] makes absorption spectra more susceptible to aggregation of the particles. By immersing the Ag monolayer into polyelectolyte system, changes within the colloidal silver were investigated with the opti-

cal absorption spectra, by means of X–rays and directly visualized with the atomic force microscope (AFM).

8.2 Silver Nanoparticles Embedded into PEM

To monitor formation and lateral properties of PEM, negatively charged silver nanoparticles have been immersed into PAH/PSS polyelectrolyte system. The architecture of the multilayer system is schematically shown in Fig. 8.1.

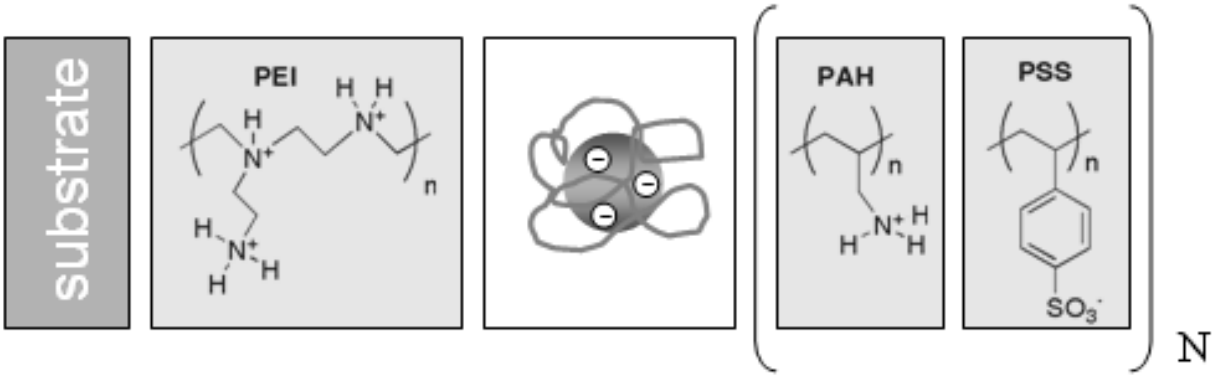

Figure 8.1: Schematic of the PEI/Ag/$(PAH/PSS)_N$ architecture adsorbed onto planar substrate, where N is number of polyelectrolyte pairs. Chemical structures of the utilized polyelectrolytes and schematic of silver colloid with its poly (vinyle alcohole) shell are included.

UV–Vis absorption measurements confirm formation of silver nanoparticles (prepared by chemical reduction method according to the description in section 3.1). The corresponding intense absorption peak, predicted by Mie theory (cf. section 4.2.3), is observed around 400 nm for silver colloidal solution. After adsorption of particles onto the surface (by immersing a quartz glass into colloidal solution), intensity of the absorption peak reduce drastically due to difference in filling factors of bulk solution and silver nanoparticle layer (several orders of magnitude), yet position is kept the same (cf. Fig. 8.2, black curve). The spectra of polyelectrolyte multilayers on top of silver nanoparticle layer adsorbed onto PEI functionalized surface are shown for integer number N of $(PAH/PSS)_N$ polyelectrolyte bilayer (cf. Fig. 8.2), except for the first PAH layer (N=0.5) directly on top of the silver. The absorption measurements are performed each time after one polyelectrolyte layer is adsorbed. For clarity, left shown only spectra obtained up to 4 BL and right – spectra from 4 to 7 BL on top of the silver.

Fig. 8.2a,c show UV–Vis absorption spectra for Ag monolayer immersed in polyelectrolyte multilayers, where first PAH layer is adsorbed from salt free solution and all following PEs from solution containing 1 mol/L KCl. Presence of salt in PAH solution causes an unexpected low–energy absorption peak which is typical for dimer formation (cf. Fig. 8.2b). This peak almost disappear after additional adsorption of PEMs. Yet, the peak width (full width at half maximum, or FWHM) remains increased compared to the original Ag NP monolayer. As one can see, with an increasing number of PAH/PSS bilayers a continuous red–shift of the absorption spectra as well as an increase in the absorbance can be observed. This can be

attributed to the formation of a polyelectrolyte film with high index of refraction (n ≈ 1.5) covering the Ag nanoparticles formerly exposed to air with its small index of refraction (n=1) [Kreibig1995], [Eck2001]. Independent if aggregation occurred or not, with increasing number of deposited polyelectrolyte layers the position of the absorption maximum shifts to larger wavelengths (from ca. 400 to 430 nm). For the higher number of layers (cf. Fig. 8.2c) reduction of the peak intensity peak can be observed. This can be attributed to deagragation or rearrangement of nanoparticles in PEMs and will be discussed in details below.

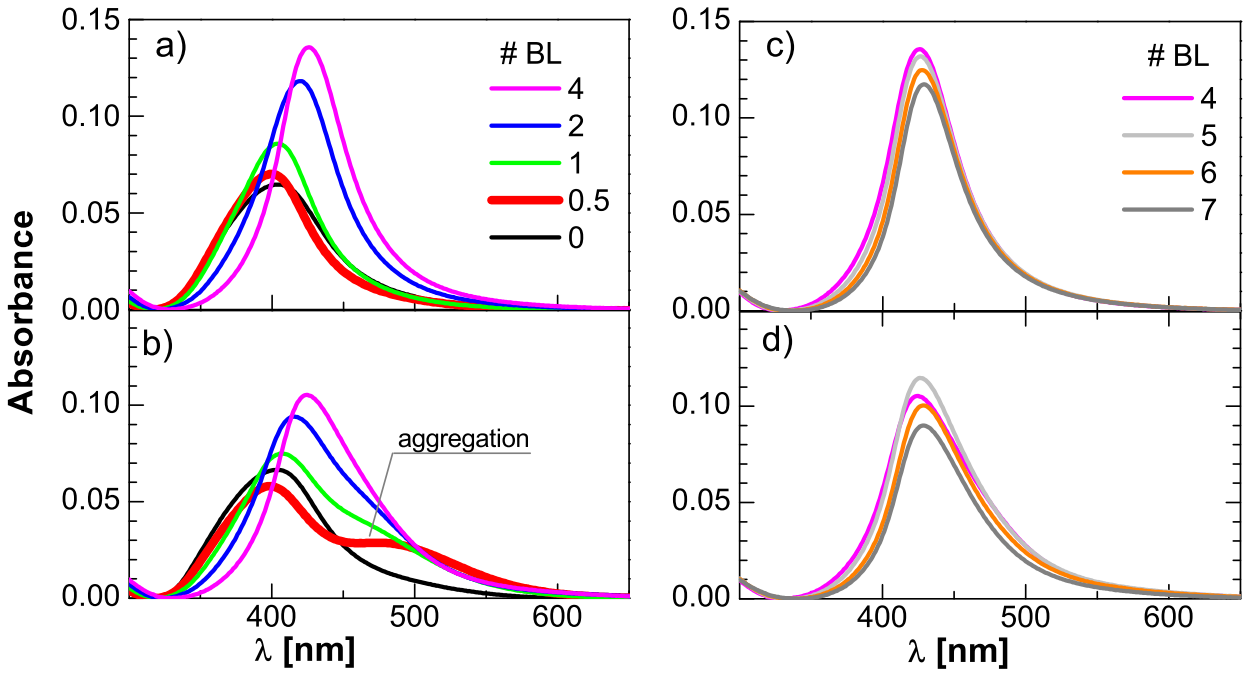

Figure 8.2: UV–Vis absorption spectra of PEI/AgNP/$(PAH/PSS)_N$ for different numbers of bilayers N adsorbed on Ag NP monolayer (N=0), measured in air. For clarity, left shown only spectra obtained up to 4 BL and right – spectra from 4 to 7 BL. Top panel (a and c): All polyelectrolytes, except the first PAH layer, are adsorbed from 3 mmol/L polyelectrolyte solution (with respect to the monomer concentration) containing 1 mol/L KCl salt. The first PAH layer, directly on top of the AgNP (N=0.5) is adsorbed from salt free solution. Bottom (b and d): The same as the top panel, yet the first PAH layer is adsorbed from the same concentration of salt as other polyelectrolytes (1 mol/L KCl). One can notice additional absorption peak at the higher wavelength.

From the measured absorption spectra, were extracted such parameters like amplitude and the wavelength corresponding to the maximum of the absorption (extinction) (cf. Fig. 8.3) and normalized integrated adsorption (cf. Fig. 8.4). According to the red–shift (i.e. λ_{max}, the position of the maximum of the absorbance A), saturation is achieved after four deposited bilayers. Similarly, the absorption intensity reaches its maximum value A_{max} for five deposited bilayers. However, then peak maxima do not shift, which suggest that nanoparticles are fully covered by PEMs. Qualitatively, the red–shift and the increased absorbance are found in numerical simulation according to the Mie theory [Kreibig1995], yet quantitative agreement deviates by a factor two [Schmitt1999]. Another deviation between theory and experiment concerns the width of the absorption peak; the experimental

peak is always broader which can be attributed to defects in the crystalline structure of the nanoparticles.

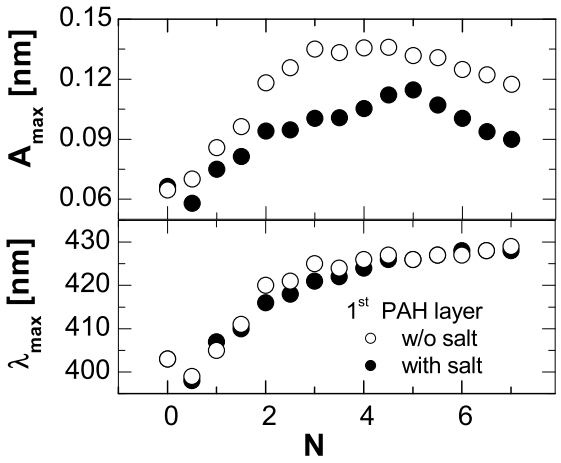

Figure 8.3: Maximum values of the absorbance (top) and the corresponding wavelength (bottom) are plotted as function of the number of polyelectrolyte bilayers N deposited on Ag NP monolayer. All data are deduced from the spectra in Fig. 8.2. The difference of the investigated films is the salt content in the adsorption solution of the first PAH layer, either salt–free (open circles, measurements depicted in Fig. 8.2a,c) or 1 mol/L KCl (full circles, cf. Fig. 8.2b,d).

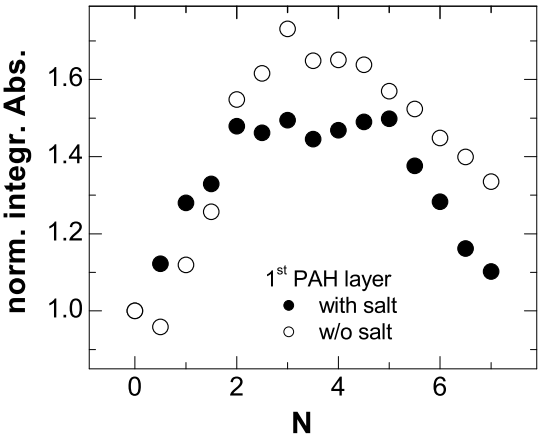

Figure 8.4: The normalized integrated absorbance of spectra shown in Fig. 8.2 is plotted as function of the number of polyelectrolyte bilayers N deposited on Ag NP monolayer. Integration limits are: from a local minimum of absorption (ca. 330 nm) to 600 nm. The difference of the investigated films is the salt content in the adsorption solution of the first PAH layer, either salt–free (open circles, measurements depicted in Fig. 8.2a,c) or 1 mol/L KCl (full circles, cf. Fig. 8.2b,d).

8.2.1 Optical Properties of Silver Monolayer

To ensure that only one monolayer of Ag nanoparticles is adsorbed, AFM measurements in air are performed after adsorption of colloidal Ag onto microscopically flat quartz surface. Apparently, presence of the initial PEI layer support adhesion of Ag nanoparticle to the substrate in contrast to amine–modified substrate [Schmitt1997]. Ag nanoparticles are found to be homogeneously distributed over the surface (presumably due to electrostatic repulsion) with average radius of colloids about 5 nm, as obtained by averaging over the height of more than 2000 nanoparticles.

The adsorption kinetic is studied for Ag NPs adsorbed from original (as prepared) and for 11 times diluted colloidal solution. As expected, reduction of the bulk concentration increase the time necessary to achieve the same surface coverage (cf. Fig. 8.5). Here the surface coverage Γ is plotted as function of square root of the adsorption time. A surface coverage of 536 particles/μm^2 is found for Ag NPs adsorbed from the original solution for 30 min by means of AFM (i.e. by counting the particles per unit area). A longer adsorption time does not lead to an increased coverage, suggesting saturation. Therefore, these adsorption time was chosen for all presented measurements. Assuming spherical Ag

nanoparticles (with particle radius ca. 5 nm) and knowing amount of Ag in colloidal solution, concentration of nanoparticles c_p is calculated to be $1.55 \cdot 10^{19}$ particles/m^3 that corresponds to the molar concentration c=25 nmol/L. It has been previously noted [Schmitt1999] that in case of negligible inplain particle interaction, molar extinction γ_c is the same for the colloidal monolayer measured in water and colloidal solution. However, if the extinction coefficient as determined from the Ag NP monolayer immersed in water is applied to measurements in the solution, molar concentration c=16 nmol/L is found. Apparently, some silver ions either did not react, or they precipitated. With such a low nanoparticle concentration, the diffusion process of the Ag nanoparticles to the surface is dominated by bulk diffusion.

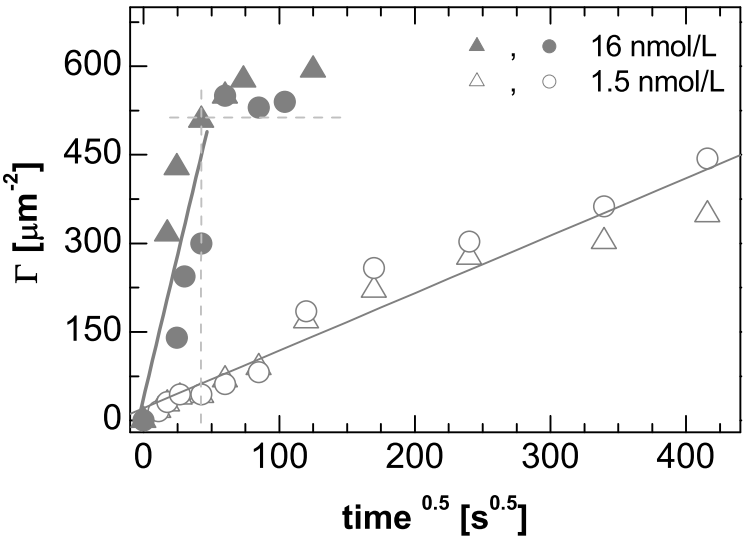

Figure 8.5: Surface coverage Γ of the silver nanoparticles (Ag NP) is plotted against square root of the deposition time for two different particle concentrations. The sample surface is positively charged due to prior adsorption of PEI. Ag NPs adsorbed from different solutions: original solution (full symbols, 16 nmol/L) and diluted solution (1.5 nmol/L). Results of UV–Vis measurements are given by triangles, those from AFM measurements by circles.

concentration c [10^{-9} mol/L]	fitted slope [10^{12} m^{-2}s$^{-1/2}$]	diffusion constant D [10^{-13} m^{2}s^{-1}]	particle radius R_p [nm]
16	(9.65 ± 2.50)	7.9	272
1.46	(0.97 ± 0.05)	9.6	224

Table 8.1: Parameters from the diffusion measurements presented in Fig. 8.5.

The diffusion constant D of a sphere in a solution with viscosity η is given by the Stokes–Einstein equation [Israelachvili1992]:

$$\mathrm{D} = \frac{\mathrm{kT}}{6\pi\eta \mathrm{R_H}} \tag{8.1}$$

where $k_B = 1.38 \cdot 10^{-23}$ JK^{-1} - Boltzmann constant, T = 293 K - solution temperature, R_H - hydrodynamic radius (also called Stokes–Einstein radius) of the Ag NPs with their polyvinyl alcohol shell. Obviously, R_H exceeds the radius of the metallic nanoparticles R_p observed with AFM.

During the adsorption process it is assumed that each particle which touches the surface sticks. Therefore, the surface coverage depends additionally on the bulk concentration c and the adsorption time t:

$$\Gamma = 2c\sqrt{Dt/\pi} \tag{8.2}$$

The equation above predicts dependence of the surface coverage to the root of the adsorption time (cf. Fig. 8.5). The absorption of a monolayer is calculated according to eq. 4.20 (cf. section 4.2). The product between nanoparticle concentration c and pathlength through the medium d can be expressed as surface coverage Γ. Thus, in air, one obtains molar extinction $\gamma_{c,max}(air)$=$1.42 \cdot 10^9$ $L \cdot mol^{-1} \cdot cm^{-1}$. This value is similar to the one found for gold nanoparticles with 13 nm diameter [Schmitt1999] and exceeds the values for organic dye molecules ($10^4 - 10^5$ $L \cdot mol^{-1} \cdot cm^{-1}$ [Atkins2006]) by a few orders of magnitude.

Averaging over both, AFM and UV–Vis measurements in air shown in Fig. 8.5, a diffusion coefficient of D=$8.4 \cdot 10^{13}$ $m^{-2}s^{-1/2}$ is obtained (cf. Table 8.1), which corresponds to a hydrodynamic radius R_H of 254 nm (cf. eq. 8.1). However, even assuming a very bulky polyvinyl alcohol shell, R_H is an order of magnitude too large. There are various causes for the apparent increase of the diffusion constant like, precipitation or nanoparticle aggregation may lead to an overestimation of the nanoparticle concentration c. Yet, the neutral PVA shell which slows down the binding of the nanoparticles to the substrate seems to be the main cause. The binding mechanism between the Ag NP and the PEI is purely electrostatic, due to the attraction between the Ag NP negative surface charge and the positively charged PEI monomers. For the electrostatic binding of the Ag NPs and the PEI, the PVA shell either has to move aside so that the AgNP sit directly on the PEI layer or some PEI chains penetrate the PVA shell and attach to the Ag NPs. The latter case is much more likely, since PEI is a branched polyelectrolyte, and surface forces measure on approach of two PEI covered surfaces electrosteric forces, which are due to PEI branches extending into solution [Pericet-Camara2006]. Therefore, the adsorption kinetics is quantitatively consistent with a process dominated by bulk diffusion, yet with an apparent increase of the diffusion constant. The slowdown can be attributed to the complicated electrostatic binding of a charged nanoparticle with a neutral shell to a surface covered with oppositely charged polyelectrolyte.

As mentioned earlier, optical properties of silver nanoparticles are governed by the surface plasmon resonance which is sensitive to the dielectric constant of the surrounding material (adsorbates, embedding host media, substrates). When the silver nanoparticle monolayer is immersed in solutions of different dielectric constants (cf. Fig. 8.6), a red shift accompanied by an increase in the absorbance is observed. This shift is attributed to the increase of ε_m, the dielectric constant of the surrounding medium. Yet, the measured positions of the absorption maxima (λ_{max}) are systematically larger than the calculated ones (cf. Fig. 8.7). Here simulated values are obtained according to equations 4.28, 4.31 and 4.32 (filling factor comes from AFM measurements) and the increase of the absorbance as well as magnitude of the red–shift are in good agreement with measurements. Concept of non–ideal NPs (with defects in the crystalline structure) may explain observed difference between calculations and measurements.

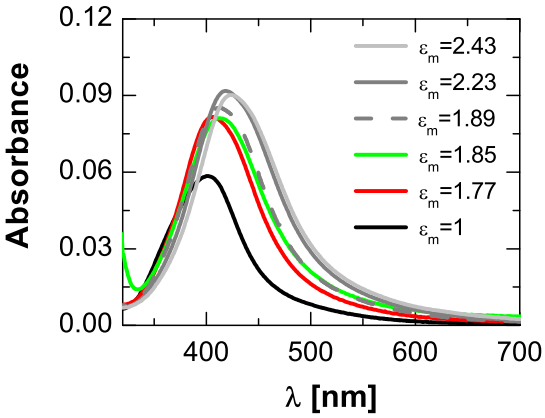

Figure 8.6: UV–Vis absorption spectra of an Ag NP monolayer (surface coverage 536 NP/μm^2) on PEI is measured in the media with different dielectric constants as indicated (air, water, acetone, hexane, toluene and bromobenzene). Note that nanoparticles adsorbs onto both sides of the quartz glass, therefore value for the measured absorbance of the nanoparticle monolayer was corrected for each curve.

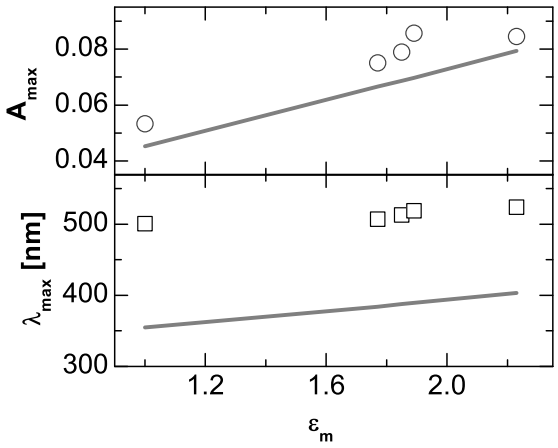

Figure 8.7: Maximum values of the absorbance (top), and the corresponding wavelength (bottom) for measured (open symbols) and simulated (solid line) spectra vs dielectric constant of the surrounding media. The parameters for the simulation are: particle radius R_p=5 nm, filling factor f=0.03.

8.2.2 Aggregation of Silver Nanoparticles

The double peak of the absorption measurement shown in Fig. 8.2b suggests that silver nanoparticles form dimers after deposition of the first PAH layer from a solution containing 1 mol/L KCl. To observe the Ag NP aggregation directly as caused by the coiled adsorption of PAH (from 1 mol/L KCl solution), the PEI/AgNP/PAH films (PAH layer prepared with and without salt) are imaged by AFM in air (cf. Fig. 8.8). To apply only small forces (pN), intermittent contact or so–called tapping mode is used.

The surface coverage as determined by object count of the freshly prepared Ag NP film is 536 particles/μm^2, the height distribution is fairly broad, yet there are almost no Ag NPs with diameters exceeding 20 nm cf. Fig. 8.8, left). After the deposition of PAH layer from 1 mol/L KCl solution, aggregation is obvious; the apparent coverage is reduced by almost a factor of two to 311 particles/μm^2 (cf. Fig. 8.8, middle). Therefore, at this stage one can talk of imaging "objects", not of isolated nanoparticles. The size distribution as determined from height histograms is broader - some particles are 25 nm thick, some are very small, suggesting that they are almost embedded in the polyelectrolyte layers. When PAH layer is adsorbed from salt–free solution, the particle count is unchanged within error (523 instead of 536 particles per μm^2). Always, when PAH is adsorbed onto the Ag NPs, the particle height appears slightly increased (from 8.7 nm to 10.4 or 9.4, if PAH is adsorbed from salt–free or 1 mol/L KCl solution, respectively). An increase of the height is to be expected due to PAH being adsorbed on top of the Ag nanoparticles, yet it is difficult to quantify because the baseline (height zero) is disturbed, especially when PAH is adsorbed in coiled conformation with the accompanying larger surface coverage.

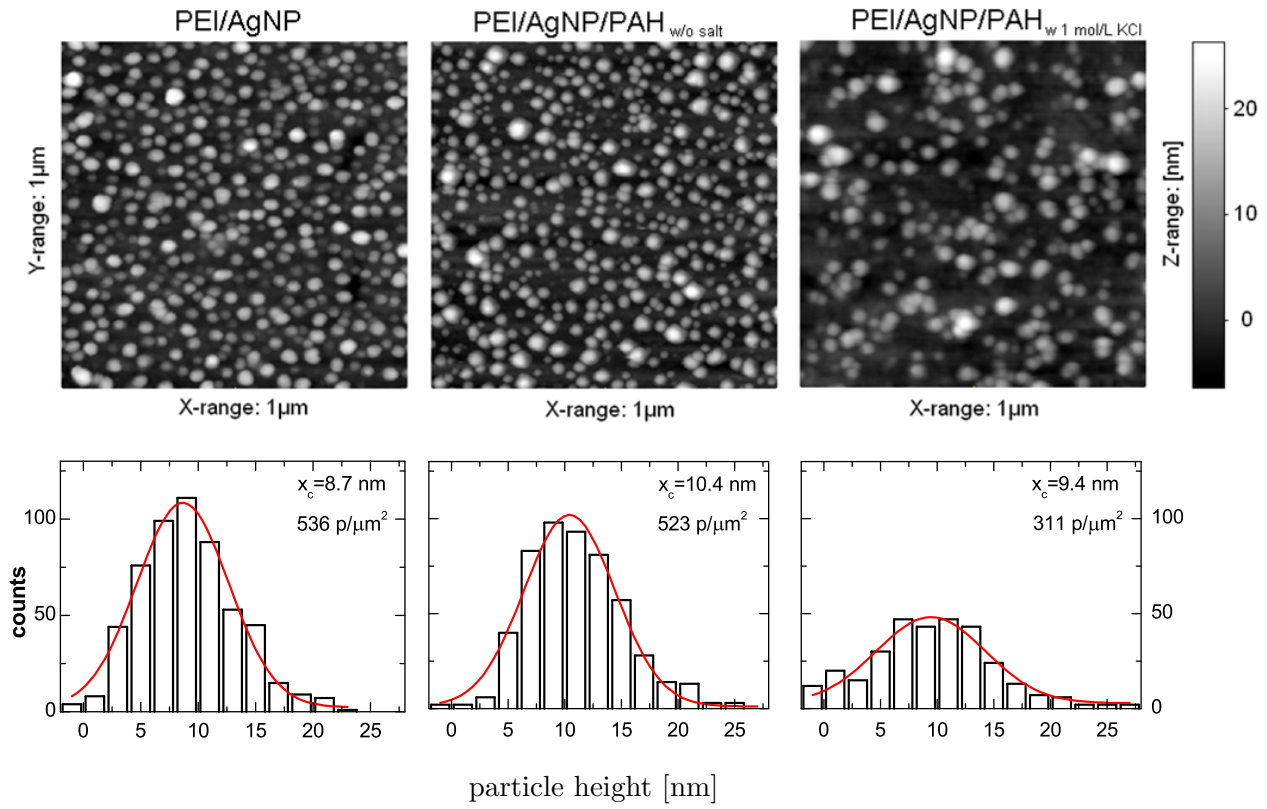

Figure 8.8: Top row: Topographic AFM images of PEI/AgNP film as deposited from original Ag solution for 30 min (left), and of PEI/AgNP/PAH films with PAH layer adsorbed from salt–free (center) or from 1 mol/L KCL solution (right). Bottom row: Height histograms of isolated/embedded/aggregated Ag NPs in the different films depicted on the top. The lines are fits to a Gaussian. The histograms are obtained from at least three different images.

Qualitatively, observed aggregation can be explained in the following way: From 1 mol/L KCl, the PAH adsorbs in a coiled conformation on top the Ag NPs, the coil extends into the subphase [Block2007], [Block2008]. To cause Ag NP aggregation, the same PAH chain has to adsorb onto two different Ag NPs and bridge the gap between the nanoparticles without touching the substrate. This way, an attraction between the two Ag nanoparticles is mediated. However, the situation is different when first PAH layer is adsorbed from salt–free solution (cf. Fig. 8.2a). Here, only an increase in absorbance is observed, the peak width (FWHM) remains unchanged. According to the literature [Decher1997], [Lowack1998], [Cho2005], in salt–free solution the PAH chain is stretched, and it adsorbs flatly onto any substrate, so there are no chains extending into solution and no chains can bridge several NPs. Therefore, no attraction between two negatively charged Ag NPs is induced.

If this model is valid, then the size and shape of the PAH have to match interparticle separation and the particle surface, to allow for bridging or flat adsorption, respectively. Since PAH is electrostatically repelled from the PEI, the PAH molecules are confined to the Ag NP surfaces. The comparison of the area per single flatly adsorbed PAH molecule and the surface of a spherical nanoparticle shows that one Ag NP can provide sufficient area for one PAH molecule: half the surface area of a spherical nanoparticle is $2\pi R_p^2 = 254\text{nm}^2$ (for particles with radius R_p=4.5 nm). A PAH molecule with 56 kDa (cf. Section 3.1) has a degree of polymerization of 600. The volume per monomer is 0.097 nm^3, the monomer

length is 0.25 nm. Assuming a cuboid shape for a monomer yields an area per monomer of 0.375 nm^2. Therefore, the minimum area per PAH molecule is 225 nm^2, assuming the molecule adsorbs with each monomer touching the surface. The minimum area per PAH molecule is a bit less than half the Ag NP surface and one can safely assume that on each nanoparticle adsorbs exactly one PAH molecule. On the other hand, if PAH adsorbs from 1 mol/L salt, only a fraction of the chain binds to the substrate, the larger part of the chain extends into the solution [Block2009]. Therefore, in principle, one PAH molecule can adsorb onto two different Ag NPs, provided the dimensions are appropriate. The radius of gyration R_g is calculated according to the theory of Benoit [Benoit1953], excluded volume effects are taken into account. For the degree of polymerization n=600, the radius of gyration R_g=13 nm and the end-to-end distance R_{ee}=32.5 nm are obtained.

Assuming that freshly adsorbed nanoparticles (particle coverage 536 particles/μm^2) form a hexagonal lattice, they should be separated by 46.4 nm. Thus, mean separation is less than twice the end-to-end distance (65 nm). Therefore, it is physically possible that one adsorbing chain bridges between two Ag NPs. However, after aggregation, the particle count is reduced (311 particles/μm^2) leading to an average aggregate separation of 60.9 nm. This value is very similar to twice the end-to-end distance, suggesting that an aggregate is the center of the adsorption and is surrounded by a shell of PAH molecules extending into solution, a bit reminiscent of a surface micelle.

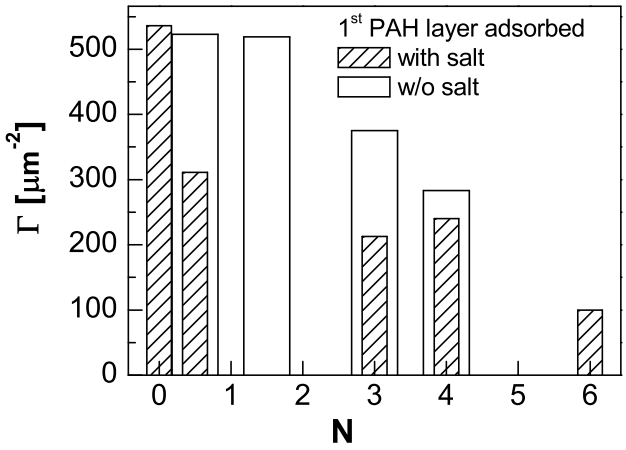

Figure 8.9: Histogram over surface coverage (objects per μm^2) as function of the number of deposited polyelectrolyte bilayers N adsorbed on Ag NP monolayer (N=0). After the first PAH layer (adsorbed from 1 mol/L KCl) coverage is drastically reduced. When PAH layer is adsorbed without salt, the particle count remain almost unchanged. With increasing number of deposited PAH/PSS bilayers, more and more Ag NPs are embedded in the PEM.

To find out how fast the space between Ag NPs is filled by subsequently adsorbed polyelectrolytes, PEI/AgNP/(PAH/PSS)$_N$ multilayers with N as the number of deposited bilayers are imaged by AFM (cf. Fig. 8.9). Additional polyelectrolyte bilayers on top of the Ag monolayer do not introduce a significant change: after three and four bilayers 40 to 45% of the original number of objects remains visible. Only after six deposited polyelectrolyte bilayers, the number of discernible objects decreases substantially (to 19%). This suggests that the objects are really Ag NPs aggregates, may be not touching but close together, tilted with respect to the substrate and more difficult to embed in a few polyelectrolyte layers.

Even when never aggregation occurred (1st PAH layer is adsorbed from salt–free solution) the number of discernible objects decreases with increasing polyelectrolyte multilayer thickness (cf. Fig. 8.9). When three PAH/PSS bilayers are placed on top of the Ag NP layer consisting of isolated nanoparticles, only 375 objects/μm^2 can be distinguished (30% of the Ag NPs are totally engulfed, 70% are visible). When four PAH/PSS bilayers are deposited, only 54% of the original objects can be recognized. Once aggregation occurred with its signature double peak in the absorption spectrum (cf. Fig. 8.2b), the Ag NPs remain close (cf. Fig. 8.8) and number of objects on the surface (resolved with AFM) is only half the number of the Ag NPs suggesting Ag NP groups. This is consistent with the UV–Vis absorption spectra, which show an increased width and a decreased intensity of the peaks (cf. Fig. 8.2 and Fig. 8.3).

In order to investigate off–plane agglomeration on Ag NPs caused by adsorption of coiled PAH molecules, UV–Vis measurements at different incident angles have been performed on the PEI/AgNP/PAH$_{(1\ \mathrm{mol/L\ KCl})}$ films. For the UV–Vis experiments reported up to now, the incident light was parallel to the surface normal (the light field is parallel to the surface plane), or $\Theta = 0^0$ following the definitions of Fig. 8.10.

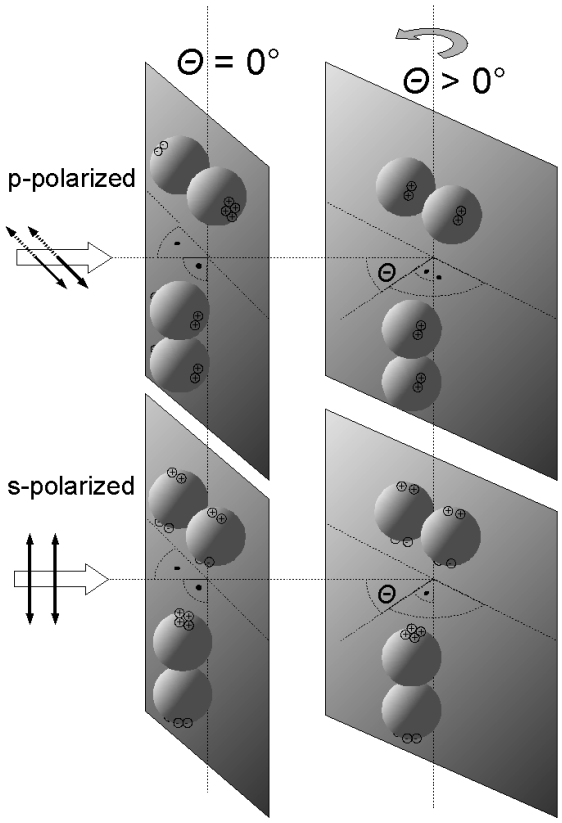

Figure 8.10: Schematic of angle–dependent polarized UV–Vis spectroscopy. Polarisation directions of a nanoparticle pair are schown for s– and p–polarized light at two different incident angles Θ.

If the angle of incidence is increased, the s–polarized light (where electric field vector is normal to the plane of incidence) is still polarized within the surface plane, therefore the absorption spectra should not change, a feature observed in Figure 8.11. For p–polarized light, where the electric field vector is along the plane of incidence, the scattering geometry is very different. The angle between the p–polarized light field and the monolayer plane is identical to the angle of incidence (cf. Fig. 8.10). On increasing the angle of incidence to 90^0 (cf. Fig. 8.10), the polarized light does probe the polarizability of the Ag NPs in the direction normal to the substrate.

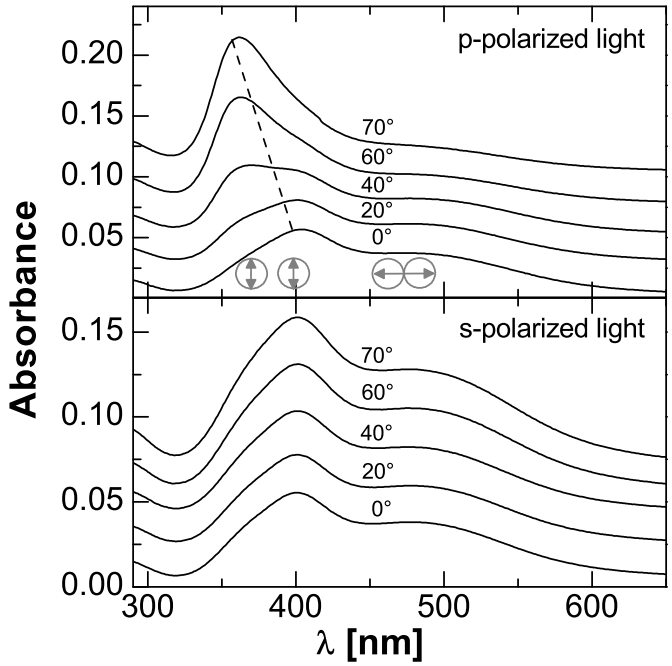

Figure 8.11: Absorption spectra of the PEI/AgNP/PAH film with the PAH layer adsorbed from 1 mol/l KCL (cf. spectrum in Fig. 8.2b) with the spectrometer geometry as depicted in Fig. 8.10. P- and s–polarized light at different incident angles is used (bottom to top in each frame: $\Theta = 0$, 20, 40, 60, 70^0). Spectra are arbitrarily shifted relative to each other. Gray circles represent positions of the peak maxima corresponding to transversal- and longitudinal polarization modes.

For isolated nanoparticles the absorption peak is dominated by the transversal polarization mode (perpendicular to the axis connecting two nanoparticles), shown in the Fig. 8.11. Longitudinal mode along the pair axis of the particles becomes significant in case of lateral aggregates. Therefore, by using light with different polarization states, it is possible tune the strength of the absorption peaks. The p–polarized absorption spectrum of the PEI/AgNP/$\text{PAH}_{(1\ \text{mol/L KCl})}$ with the pronounced double peak structure is shown in Figure 8.11 for various angles of incidence. On increase of the angle Θ, the low–energy shoulder corresponding to the longitudinal excitation decreases yet does not disappear completely. Concomitantly, the low energy peak corresponding to the transversal mode experiences a blue–shift. Confirming the AFM images (cf. Fig. 8.8), some dimers are tilted with respect to the surface or are outright three–dimensional.

8.2.3 Rearrangement of Nanoparticles beneath a PEM

To understand the optical measurements shown in Fig. 8.2, the distinctive absorption spectra of approaching Ag NPs are simulated numerically. [1] As it was shown earlier, with increasing number of deposited bilayers the absorption maximum increases (cf. Fig. 8.3). However, the never–aggregated Ag nanoparticles (i.e. first PAH layer adsorbed from salt–free solution) exhibit a larger absorption maximum $A_{\max}$, independent how many polyelectrolyte bilayers are deposited on top of the Ag NP layer. The effect gets more pronounced when more than two polyelectrolyte bilayers are deposited (cf. Figs. 8.2, 8.3). Obviously, the absorbing PSS layer penetrates into the PAH layer and successfully competes with the Ag NP surface for PAH monomers to form electrostatic bonds. Also, the PSS chains partly bind to the PEI layer not covered by Ag NPs and fill the space between the Ag NPs.

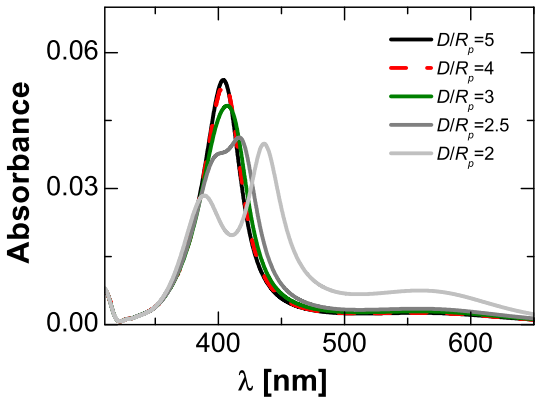

Figure 8.12: Simulated absorption spectra of two approaching silver nanoparticles separated by a distance D. The particles touch, if ratio $D/R_p = 2$. Used parameters are: particle radius R_p= 5 nm, filling factor $f = 0.03$, dielectric constant of surroundings ε_m=2.25.

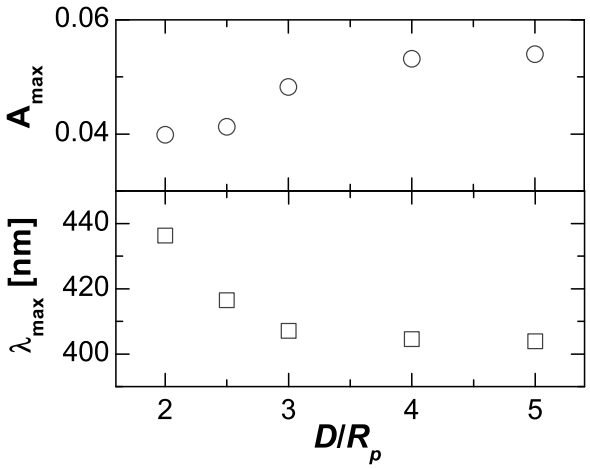

Figure 8.13: Maximum values of the absorbance (top), and the corresponding wavelength (bottom) for spectra shown in Fig. 8.12 are plotted as a function of normalized separation distance D/R_p.

Figure 8.12 shows calculated extinction spectra of approaching and aggregated Ag nanoparticle pairs (with the data for $\varepsilon(\lambda)$ according to [Lide2003]). The absorption according to equations 4.28, 4.31 and 4.32 is calculated as function of the Ag NP separation D and normalized with respect to the radius R_p of the Ag NPs. One observes a red–shift of the maximum and a simultaneous decrease in the absorbance (cf. Fig. 8.13). For gold nanoparticles, the same red–shift is obtained, yet accompanied with an increase in the absorbance [Schmitt1999]. This is a qualitative difference caused by the quantitatively different dependence of e for the different materials. For a second weak maximum at smaller wavelengths is found. The second maximum is also found for the gold nanoparticles. When the particles touch, the absorbance at the longer wavelength is attributed to the longitudinal mode, the shorter one to the transversal mode (cf. Fig. 8.14).

[1] These and all following simulations are performed by Olaf Soltwedel, Institute of Physics, Greifswald

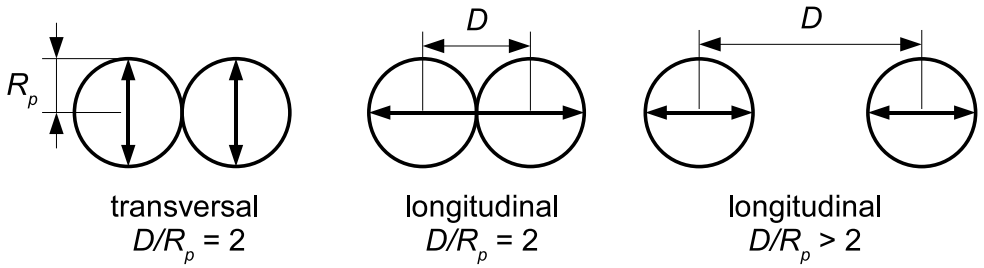

Figure 8.14: Excitation modes of an interacting nanoparticle pair. Particle radius R_p, center to center separation distance between particles D and respective ratio D/R_p are indicated. In case of $D/R_p = 2$ the nanoparticles are touching.

As the simulations depicted in Figure 8.12 show, the absorption maximum decreases when the nanoparticles are close to each other, with their centres separated by 1.5 - 2 particle diameters (or the gap between the Ag NP surfaces between 0.5 and 1 particle diameter). In this case, the position of the absorption maximum is not affected, only the amplitude. The reduced amplitude of the absorption peaks bears evidence of the still close Ag NPs, even after the deposition of four polyelectrolyte bilayers.

With X–ray reflectivity the electron density profile perpendicular to the substrate surface is probed (cf. Fig. 8.15). X–rays are reflected, when the electron density changes drastically, causing interference patterns. As one can see from the lowest plot (cf. Fig. 8.15), the PEI layer covered by a Ag NP monolayer shows one minimum at very high Q_z, indicating a very thin film. When an additional PAH layer from high salt condition is adsorbed, the reflected intensity decays slowly, no minimum can be detected. This indicates an extremely rough film/air interface. When more polyelectrolyte layers are adsorbed, an interference patterns with a sequence of minima and maxima ensues. The more polyelectrolyte layers are adsorbed, the narrower are the interference minima indicating increased film thickness. Such X–ray reflectivity curves are often obtained when film formation is monitored [Decher1997], [Büscher2002]. However, on close inspection deviations from the typical cosine–function can be observed: with one or two bilayers on the silver nanoparticles, the curves increase after a minimum faster than they decay towards the next minimum (cf. Fig. 8.15). The corresponding electron density profiles can be seen in Fig. 8.16. Two–slab model, and sometimes a three–slab model turns out to be necessary to describe the electron density profile of the investigated film. The expected electron density of a polyelectrolyte layer with embedded Ag NPs is 0.487 $Å^{-3}$ (considering the electron density of bulk silver 2.753 $Å^{-3}$ and volume fraction of the Ag NPs about 3%). This value is substantially less than electron density of SiO_2 (0.659 $Å^{-3}$) and only slightly more than for the pure polyelectrolyte layer with 1.5 water molecules per PAH/PSS monomer pair (0.417 $Å^{-3}$). Thus, the most dramatic changes in the electron density occur at the substrate/film interface and the film/air interface (cf. Fig. 8.16) and therefore, it is no surprise that the reflectivity curves resemble the somewhat modulated interference patterns of simple polyelectrolyte films.

Table 8.2 provides the parameters (including model constraints) deduced from the fits to the measurements shown in Fig. 8.15. As one can notice, the modeled electron density consists of as few slabs and especially as few parameters as possible. However, for some films one or two slabs are necessary to model the complicated roughness of the film and therefore, some parameters do not have any specific physical meaning.

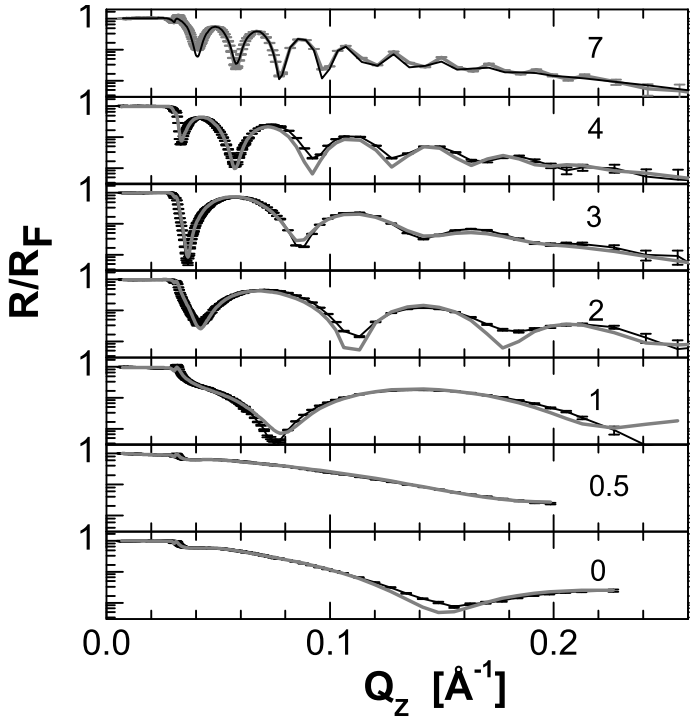

Figure 8.15: Normalized X–ray reflectivity curves of the PEI/Ag/$(PAH/PSS)_N$ films for different number of bilayers N as indicated. All polyelectrolytes are adsorbed from solution containing 1 mol/L KCl. Straight lines are fits; points with error bars are measured data.

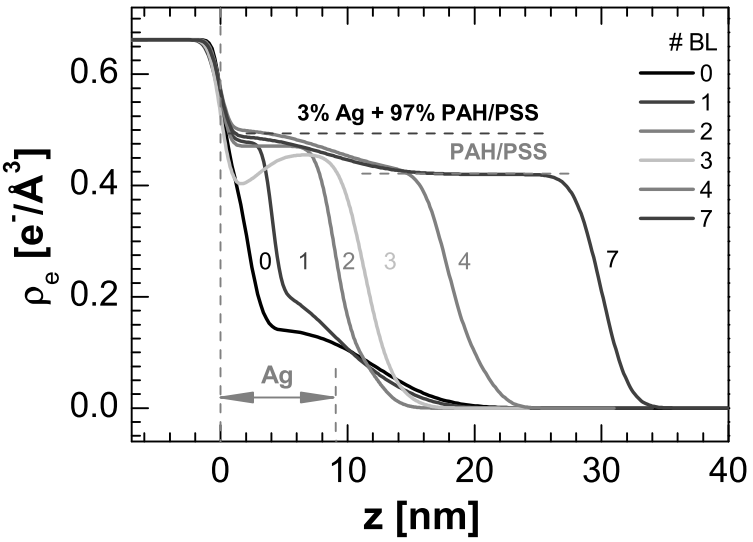

Figure 8.16: The electron density profiles deduced from the fits to measurements shown in Fig. 8.15. Left to right: silicon/film interface (positioned at z=0) and polyelectrolyte film with embedded Ag NP layer (average diameter indicated by the arrow), depending on the film structure.

For example, for the pure Ag NP film on PEI, three slabs provide a good fit. The slab

adjacent to the substrate surface has a rather high electron density, slightly exceeding the one of a polyelectrolyte multilayer, and consistent with a film consisting of a polyelectrolyte multilayer with embedded Ag NPs. But it is thin, only 2 nm, whereas the Ag NP layer is 10 nm thick. In the electron density profiles one recognizes that the lower part of the Ag NPs is already embedded in a polyelectrolyte multilayer, while the upper part, covered by polyelectrolyte, extends into the air (cf. Fig. 8.16). The more polyelectrolyte layers are adsorbed, the more the Ag NPs are embedded. Apparently, the Ag NPs remain close to the substrate and vertically immobile.

At first approach, one may think that the Ag NPs should be embedded in the polyelectrolyte film when the film thickness exceeds the Ag NP diameter. This is achieved after depositing three bilayers (all from 1 mol/L KCl), cf. Fig. 8.17. However, absorption spectra indicate only partial coverage of the Ag NPs after the deposition of three bilayers (cf. Figures 8.2 and 8.3). It is necessary that the top of every Ag NP is embedded by polyelectrolyte. According to the electron density profiles, after depositing seven PAH/PSS bilayers (all from 1 mol/L KCl solution), the Ag NPs are completely surrounded by a polyelectrolyte multilayer. The electron density profile shows adjacent to the substrate an increased electron density (due to the embedded Ag NPs), which decays slowly towards the value of the pure polyelectrolyte film. Then, the electron density is constant, until it decays fast towards the air. With four bilayers on top of the Ag NPs, the pure polyelectrolyte film density is almost achieved. Therefore, it makes sense that according to UV–Vis measurements, four to five bilayers are necessary to achieve complete nanoparticle enclosure (cf. Fig. 8.3). This suggests that a few nanoparticles have moved away from the substrate surface, presumably during aggregation.

Parameters	N=0	N=1	N=2	N=3	N=4	N=7
SiO_2						
ρ_e [Å^{-3}]	0.659	0.659	0.659	0.659	0.659	0.659
σ_{sub} [Å]	5.0	7.4	5.7	7.1	6.1	6.3
Box 1						
l_1 [Å]	19.5	42.6	89.2	$l_1 = l_3$	90	85.7
ρ_e [Å^{-3}]	0.455	0.479	0.468	0.392	0.501	0.489
σ_{int} [Å]	9.8	5.8	10.5	$l_1/2$=15.7	$l_1/2$=45	$l_1/2$=42.9
Box 2						
l_2 [Å]	19.5	42.6	30.6	81.0	87.8	214.7
ρ_e [Å^{-3}]	0.137	0.217	0.122	0.468	0.418	0.418
σ_2 [Å]	$l_2/2$=9.8	$l_2/2$=21.3	$l_2/2$=15.3	$l_2/2$=40.5	$\sigma_2=\sigma_{out}$	16.8
Box 3						
l_3 [Å]	83.8	53.9	–	31.3	32.8	–
ρ_e [Å^{-3}]	0.137	0.096	–	0.057	0.182	–
σ_{out} [Å]	$l_3/2$=41.9	$l_3/2$=27.0	–	$l_3/2$=15.7	14.4	–

Table 8.2: Parameters for PEI/AgNPs/$(PAH/PSS)_N$ architecture fitted with a model consisting of two or three slabs, therefore σ_2 is either internal or outer (film/air) roughness. If length of the boxes (l), electron density (ρ_e) or roughness σ are coupled to each other, corresponding constrain is indicated. All polyelectrolytes are adsorbed from 1 mol/l KCL at 20^0 C.

The film with three polyelectrolyte bilayers on top of the Ag NPs is something of a maverick, there is a decreased electron density adjacent to the substrate, suggesting the polyelectrolyte partially dewetted the substrate. This observation was not reproduced for other films. For seven PAH/PSS bilayers, the model for the film consists of two slabs. The first layer is 8.6 nm thick. Its electron density is found to be the one expected for a film consisting of 3% Ag NPs and 97% polyelectrolyte. The second slab consists of polyelectrolyte film only; the fit also yields an electron density consistent with expectations (cf. Table 8.2).

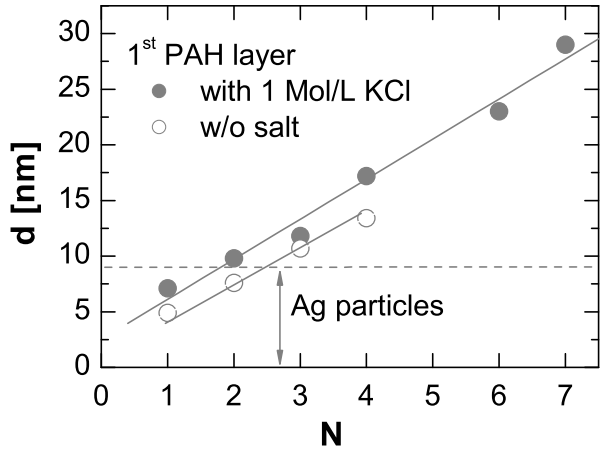

Figure 8.17: Thickness of the polyelectrolyte film vs number of PAH/PSS bilayers on top of Ag nanoparticle monolayer. Full symbols refer to the measurements shown in Fig. 8.15. When the first PAH layer is adsorbed from salt free solution, open symbols are used. The height of the Ag NPs is given as determined from AFM.

In Fig. 8.17 the thickness of the polyelectrolyte film as function of the number of deposited polyelectrolyte bilayers is shown. Again, the well-known linear growth of the film thickness is found. The bilayers thickness is 3.6 nm, well in agreement with the literature [Büscher2002], [Gopinadhan2007b]. If the first PAH layer is adsorbed from salt–free solution (reflectivity data are not shown), then the total film thickness is somewhat smaller (cf. Fig. 8.17). Yet the thickness per deposited PAH/PSS bilayer is the same. Finally, it is interesting to compare the film thickness necessary to embed an Ag NP layer which never aggregated (first PAH layer adsorbed from pure water, maximum absorption peak after three to four polyelectrolyte bilayers) with the thickness of an Ag NP in which aggregation occurred after the deposition of the first PAH layer (from 1 mol/L salt solution, maximum absorption after four to five bilayers). In the case of the never–aggregated Ag NPs, a polyelectrolyte film thickness of 10.7 - 13.4 nm is necessary to engulf the Ag NP layer. In contrast, the film thickness necessary to embed the once aggregated Ag NPs is 17.2 - 21 nm (cf. Fig. 8.17).

To find out how tightly the polyelectrolytes are bound to the Ag NPs [Lu2007], the absorption spectra of PEI/Ag/$(PAH/PSS)_N$ films are measured in solution (cf. Figs. 8.18, 8.19). For the first four deposited layers, the measurements in air show a continuous increase of the absorption maximum while the measurements in water show a drastic increase after the deposition of one bilayer, then the absorption intensity remains fairly constant. Obviously, the adsorption of two or three additional polyelectrolyte layers does not change the composition of the surrounding. The only effect which is seen is a monotonous shift

of the position of the adsorption peak to larger wavelengths. This suggests that the close surroundings of an Ag NP consists of a mixture of polyelectrolyte and water. Considering the small changes on addition of another polyelectrolyte layer, one may conclude that water dominates. The few polyelectrolyte molecules adjacent to the Ag NPs can move and rearrange themselves, when an additional polyelectrolyte layer is adsorbed which may cause the changed position of the absorption peak. Furthermore, the disappearance of the Ag NP aggregation peak after deposition of the first PSS layer (cf. Fig. 8.2b) is consistent with such rearrangements.

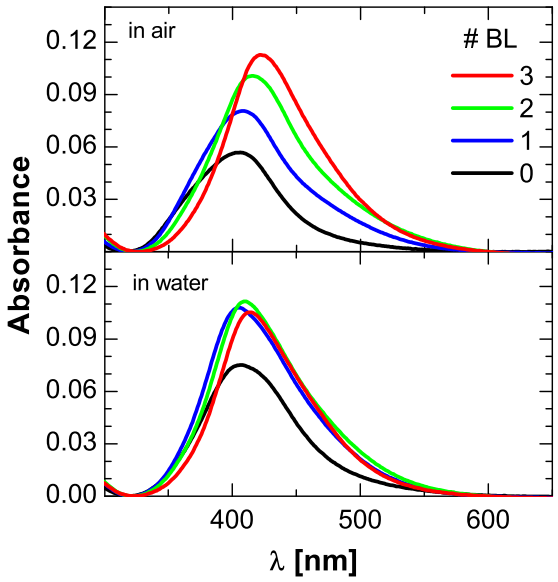

Figure 8.18: UV–Vis absorption spectra of PEI/Ag/(PAH/PSS)$_N$ architecture for different numbers of bilayers N adsorbed on Ag NP monolayer (N=0) and measured in air (top), in water (bottom). The first PAH layer was adsorbed from high concentrated salt solution (1 mol/L KCl).

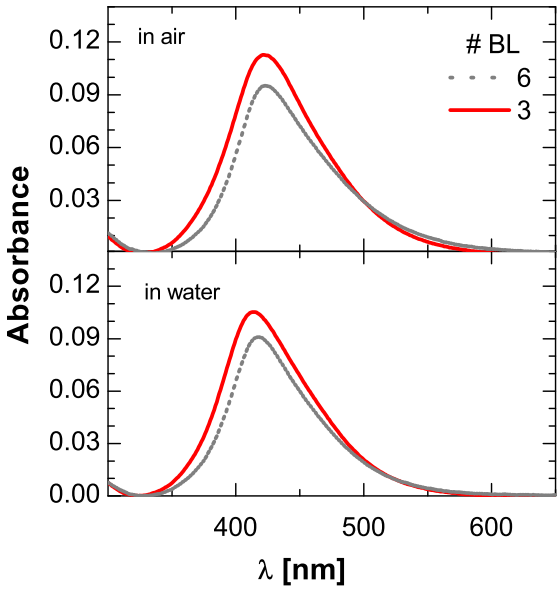

Figure 8.19: UV–Vis absorption spectra of PEI/Ag/(PAH/PSS)$_N$ architecture for N=3, 6 adsorbed on Ag NP monolayer (N=0) and measured in air (top), in water (bottom). The first PAH layer was adsorbed from high concentrated salt solution (1 mol/L KCl).

Additionally, the absorption measurements in water show a decrease of the maximum absorption intensity for 6 deposited polyelectrolyte layers (cf. Fig. 8.19), compared to three layers (cf. Fig. 8.18). This decrease is very similar to the one observed in air, when the 5th, 6th and 7th polyelectrolyte bilayers are deposited (cf. Fig. 8.2). It suggests partial approach of the Ag nanoparticles due to the penetration of the additional layers inside the PEM. Interpenetration of the layers is shown with neutron reflectivity, which is sensitive to scattering length density (SLD) gradients along to the surface normal [Decher1997], [Gopinadhan2007b], [Ivanova2008]. It was found that polyanion layer (PSS$_d$) extends into the neighboring polyanion layers and a bit into the next–nearest layers (both top and bottom) for PAH/PSS system. These lateral movements and rearrangements progress towards the substrate, even though the adsorbing layer does not get close to the substrate. Since an adsorbing layer does penetrate at most three bilayers we suggest that the polyelectrolyte adsorption causes lateral rearrangements of the underlying layers and forces some Ag NPs closer to

each other. In the future it will be interesting to explore how many layers are necessary to provide a steady state adjacent to the substrate.

8.3 Discussion

Our results demonstrate that after adsorption of a PAH layer (in presence of high salt) on top of the silver nanoparticle monolayer, particle aggregation occurs, as evidenced by the double peak of the absorption spectrum, and the decrease by a factor of two of the objects counted by AFM. On adsorption of the next polyanion (PSS) layer, the double peak disappears, yet the particle count remains reduced as does the adsorption maximum, suggesting that aggregated nanoparticles remain a few nm apart. This self–deaggregation property of the Ag NPs probably originates from formation of interpenetrated multilayer structures.

If the PAH layer covering the Ag nanoparticles is adsorbed from salt–free solution, the lateral aggregation is suppressed and number of objects remains the same. It allows us to assume that the aggregation is mediated by the PAH adsorbing in coiled conformation, the assumption which is supported by the geometric characteristics of the investigated system (mean distance between Ag NPs after deposition, radius of gyration and end-to-end distance of PAH in 1 mol/L salt solution). Furthermore, PAH from a salt–free solution adsorbs in a flat conformation, therefore, each PAH molecule is localized on a specific nanoparticle.

During polyelectrolyte multilayer build up, the well-known red–shift of the absorption spectra occurs, which is attributed to the changing dielectric constant of the surroundings. Interestingly, the aggregation caused by the first PAH layer (adsorbed from high salt conditions) is partially reversible. If a PSS layer is adsorbed on top of the PAH layer, the double peak disappears. Furthermore, polarized absorption spectroscopy and X–ray reflectivity indicate that the aggregated Ag NPs are tilted with respect to the substrate. However, small angle reflection experiments on Ag/PE multilayer show that the Ag NPs remain close to the substrate. Combining X–ray reflectivity and UV–Vis absorption it is concluded that a 10.7–13.4 nm thick PEM film is necessary to completely embed those Ag NPs which never aggregated and remained flat. Once aggregated Ag NPs need a substantially thicker film (17.2–21 nm). Finally, slight decreases in the absorption intensity is observed, when more than 4 or 5 polyelectrolyte bilayers are deposited on top of silver nanoparticle monolayer. Assuming penetration of the adsorbing polyelectrolytes into the underlying layers one can explain lateral rearrangements of some Ag NPs. These results show the great potential of surface plasmonic techniques for detection of complicated film structures and their changes, which can be critical for sensing applications.

8.4 Conclusion

The lateral and vertical aggregation of silver nanoparticles (ca. 5 nm radius) prepared as the first negatively charged layer of polyelectrolyte multilayer film (with PAH and PSS as polycation/polyanion pair) is probed with optical absorption spectroscopy, atomic force microscopy and X–ray reflectometry. In case of adsorption high salt containing PAH layer on top of the nanoparticle monolayer, the appearance of a second UV–Vis absorbance peak indicates formation of silver aggregates.

Condition for polyelectrolyte multilayer build–up avoiding nanoparticle aggregation is explored. Measured absorption spectra of silver nanoparticles are proved to be very sensitive to the dielectric constant of different liquids and additional polyelectrolyte layers covering the particles. According to the absorption spectra, the never–aggregated Ag NPs are embedded after three to four deposited polyelectrolyte bilayers, the once–aggregated Ag NPs need four to five bilayers, which is consistent with the non–flat arrangement of the dimers observed with the p–polarized absorption spectroscopy. AFM as well as UV–Vis spectroscopy with polarized light under variation of the angle of incidence show that the aggregates are three–dimensional. This indicates that adsorption of additional polyelectrolyte layers compresses the nanoparticle aggregates. Thus, adsorption of polyelectrolytes in presence of high salt exert lateral forces onto the nanoparticles leading to their aggregation. A simple strategy to tune lateral properties of polyelectrolyte multilayers is provided.

Part IV

Thesis Summary

Summary

This thesis presents the results of experimental investigations of the vertical and lateral properties of polyelectrolyte multilayer films (PEMs) adsorbed on a solid support. PEMs are a new class of organic thin films based on self–assembly layer-by-layer (LbL) processes of oppositely charged polyelectrolytes (charged polymers). The LbL assembly technique allows precise control of film thickness within a few nanometers and makes PEM systems especially interesting for technical applications. Thin films are prepared by alternating exposure of a hydrophilic substrate to solutions of oppositely charged polyelectrolytes. In this work, synthetic polycation poly (allylamine hydrochloride) (PAH) and polyanion poly (styrene sulfonate) (PSS) have been used.

In order to understand the phenomenological behaviour of multilayer formation, the role of driving forces of different nature has been investigated. Range and amplitude of the electrostatic force during PEM build–up, has been shielded by use of high salt concentration in the deposition solution. Akin to most neutral polymers in water, the solvent quality of polyelectrolyte declines on the temperature rise. The thickness of the multilayer film increases with temperature at high salt, as well as with increasing salt concentration. However, common theories of PEM build–up are based on classical electrostatic theory that does not explain temperature effect on the film thickness. As a foundation of any theory, role of non–elecrostatic (secondary) forces is explored in this thesis.

Four complementary methods have been combined to investigate the properties and composition of PEMs. X–ray reflectivity is sensitive to electron density gradients, and therefore provides information about film thickness, average electron density and interfacial roughness between materials of different electron densities (like PEM and air). Neutrons are the unique probe that is sensitive to the internal order of the multilayers (scattering length density variation) due to selective deuteration of the layers (PSS replaced by PSS_d). Therefore neutron reflectivity at V6 beamline, at the research reactor BER II, Helmholtz Centre for Materials and Energy (former Hahn-Meitner-Institute), was used in this work. Ultraviolet–visible (UV–Vis) light induces the characteristic absorption peak of polyelectrolytes and metallic nanoparticles, therefore with UV–Vis absorption spectroscopy is possible to probe the aggregation of metallic nanoparticles embedded into PEM by measuring their absorption spectra (imaginary part of the refraction index). Atomic force microscopy (AFM) allows to observe lateral structures at nano–level and to obtain surface topology of the films. Application of only small forces (pN) is achieved by use of a intermittent contact (tapping) mode in air.

The experimental results reported in this thesis provide information concerning the influence of preparation conditions as well as post–deposition treatment. By varying the temperature of the polyelectrolyte solution during preparation, concentration and type of salt ions in the deposition solution, changing the relative humidity and temperature after preparation, the following results were achieved:

- PEM architecture consisting of thick, relative to the roughness of the adjacent interface, protonated and deuterated blocks (we call it block architecture) is used as a new approach in neutron reflectivity experiments. It provides the possibility to quantify interfaces and allows to obtain the roughness of an internal interface as independent parameter, an improvement compared to the classical superlattice structure.

- Swelling of PEMs in light and heavy water (H_2O and D_2O) is found to be completely reversible in terms of film thickness (linear swelling) and partially reversible in terms of film/air and inner roughness. Besides reversibility, swelling behavior seems to be independent of preparation temperature, since it was checked on four different block architectures prepared at 15^0 C and 35^0 C. Fully protonated (deuterated), as well as mixed protonated/deuterated and deuterated/protonated architectures are used. The data presented here indicate that after immersion of samples in D_2O all three protons in the amino group of each polycation monomer are substituted by deuterium ions. The majority of the tightly bound water molecules found in the freshly prepared, dried films remain in the film and are not replaced by D_2O molecules at 100% r.h. D_2O. Interestingly, independent of the number of tightly bound water molecules inside the film, about the same amount of water molecules per monomer pair is incorporated during the swelling.

- The film thickness of PEMs prepared at 15^0 C in presence of 1 mol/L salt in polyelectrolyte solution is found to increase with the type of anions according to the Hofmeister series and to be independent of the type of cations, which is in good agreement with the literature. Roughness at the film/air interface seems to be the same as the inner roughness and dependent on the type of salt for anions. The amount of bound water is found to be constant for all types of investigated salts at 15^0 C (1 to 2 H_2O molecules per PAH/PSS and PAH/PSSd pair at 0% relative humidity).

- The onset of temperature effects on PAH/PSS multilayer growth is explored by systematic variation of temperature and salt concentration in polyelectrolyte deposition solutions. An increase in the preparation temperature increases the thickness per polyelectrolyte layer pair, if the salt concentration exceeds 0.1 mol/L suggesting that electrostatic forces determine adsorption of PEMs only at low salt concentration. Interpenetration between the layers is also found to be dependent on preparation temperature for PEMs prepared in presence of 1 mol/L NaCl. Thus, the thickness ratio of deuterated and protonated blocks (outer to inner block length) for architecture consisting of 5 blocks each changes from 1.1 for the sample prepared from 15^0 C, to 1.2 for 35^0 C and 1.7 for 50^0 C. This can be attributed to the zone model for polyelectrolyte multilayer film growth.

- Observed changes in PEM conformation by post–deposition heating was found to result in either breaking of the film structure, or in lateral shrinking accompanied by enormous internal roughness increase. Adsorption of PEM onto an Ag nanonoparticle monolayer in the presence of high salt concentration (1 mol/L KCl) exerts lateral forces between the negatively charged nanoparticles leading to their aggregation. However, adsorption of the first polycation layer from the salt–free solution suppresses aggregation. Thus, a simple strategy to tune lateral properties of polyelectrolyte multilayers is provided.

Summarizing the main results, the unambiguous parametrization of the investigated system for neutron reflectivity measurements enables to obtain detailed information about internal interfaces. The approach presented here for polyelectrolyte multilayer architectures consisting of thick protonated and deuterated blocks can be used in order to distinguish different zones of the thin film growth which can be described as precursor and core zones. Thus, almost no bound water is found in precursor layers at 0% relative humidity, which suggests that water is mobile and the precursor layer is not in the glassy state like in the central zone of the PEM. Swelling behaviour of the PEMs (reversibility of the swelling) can be understood in terms of equilibrium reactions. Explored influence of temperature and type of salt used during preparation contributes to a better understanding of the formation of PEMs. The dependence of the film thickness on preparation temperature, concentration and the type of salt can be described by the hydrophobic nature of the effect. Experimental observations demonstrate that it is possible to decrease both the range and the amplitude of the electrostatic force by using an ion concentration of at least 0.1 mol/L in the solution. The role of secondary interactions such as hydrophobic attraction of the chains that can overcome electrostatic repulsion and become the major contributing factor for the layer formation and resulting structures is emphasized.

Symbols and Abbreviations

Through this thesis the CGS system of units is used. Along with Ångstrom (1 Å=10^{-10} m) nanometer (1 nm=10^{-9} m=10 Å) is often used although it is not a part of CGS system.

A	absorbance of the material
α	polarizability
B	Jones–Dole viscosity coefficient
b	scattering length [Å]
β	absorption of the material
c	molar concentration [mol/L]
c_p	particle concentration [m^{-3}]
d	path length through the medium [nm]
d_N	deuterated part of PEM
D	diffusion constant
D	center to center distance of neighboring particles
e	elementary charge
ε	dielectric function
ε_m	dielectric function of the medium
ε_0	electric permittivity of vacuum $8.8 \cdot 10^{-12}$ [Fm^{-1}]
f	filling factor
γ	extinction coefficient [cm^{-1}]
γ_c	molar extinction coefficient [$L \cdot mol^{-1} \cdot cm^{-1}$]
I	intensity of light
I_0	incident intensity of light
I	ionic strength of the solution [mol/L]
k	order of the Bragg peak
k_B	Boltzmann constant $1.38 \cdot 10^{-23}$ [JK^{-1}]
κ	imaginary part of the refractive index
l	thickness of the layer [nm] or [Å]
l_{BL}	thickness of the bilayer [nm] or [Å]
λ	wavelength [nm]
λ_D	Debye screening length [nm]
m_{H_2O}	amount of light water molecules per monomer pair in the swollen film
m_{D_2O}	amount of heavy water molecules per monomer pair in the swollen film
N	number of bilayers (polyelectrolyte pairs)
N	number of deuterated repeat units
N_d	number density

N_e	number of electrons
n	degree of polymerization
n	refractive index (real part for nanoparticles and complex for X–rays and neutrons)
n_{H_2O}	amount of tightly bound light water molecules per monomer pair
$n_{H_2O,\,dry}$	amount of tightly bound light water molecules per monomer pair at 0% r.h.
$n_{water,\,swell}$	amount of water molecules (H_2O and D_2O) per monomer pair in the swollen film
η	viscosity
p_N	protonated part of PEM
ρ	scattering length density (SLD) [$Å^{-2}$]
ρ_e	electron density (ED) [$Å^{-3}$]
R_F	Fresnel reflectivity
R	reflectivity
R_g	radius of gyration of the polymer
R_H	hydrodynamic radius
R_p	particle radius [nm]
r_e	classical electron radius [m]
r.h.	relative humidity [%]
σ	roughness [Å]
σ_{int}	internal roughness [Å]
σ_{out}	film/air roughness [Å]
T	temperature of the solution [^{0} C] or [K]
t	adsorption time
θ_i	incident angle
V	volume (molecular)
ω_p	plasma frequency
Q_z	momentum transfer normal to surface [$Å^{-1}$]
z_0	distance between layers

BL	bilayer or polyelectrolyte layer pair
ED	electron density
PEI	poly (ethylene imine)
PAH	poly (allylamine hydrochloride)
PSS	poly (styrene sulfonate)
PSS_d	deuterated poly (styrene sulfonate)
PEM	polyelectrolyte multilayer
SLD	scattering length density
UV	ultraviolet
Vis	visible

Bibliography

[Adamson1997] A. W. Adamson and A. P. Gast. *Physical Chemistry of Surfaces.* Wiley, New York (1997).

[Ahrens1997] H. Ahrens, S. Förster, and C. A. Helm. Polyelectrolyte brushes grafted at the air/water interface. *Macromol.*, **30**, 8447–8452 (1997).

[Ahrens2004] H. Ahrens, K. Büscher, D. Eck, S. Förster, C. Luap, G. Papastavrou, J. Schmitt, R. Steitz, and C. A. Helm. Poly(sterene sulfonate) self–organization: Electrostatic and secondary interactions. *Macromol. Symp.*, **211**, 93–105 (2004).

[Als-Nielsen1985] J. Als-Nielsen. Solid and liquid surfaces studied by synchrotron X–ray diffraction. In G. R. Hubbard, C. S. Barrett, P. K. Predicki, and D. E. Leyden, editors, *Advances in Solid State Physics, vol. 25*, pages 1–2. Springer (1985).

[Antipov2004] A. A. Antipov and G. B. Sukhorukov. Polyelectrolyte multilayer capsules as vehicles with tunable permeability. *Adv. in Col. and Interf. Sci*, **111**, 49–61 (2004).

[Atkins2006] P. W. Atkins. *Physical Chemistry.* W. H. Freeman and Company, New York (2006).

[Bae1995] J. S. Bae, E.-R. Kim, and H. Lee. Self-assembled multilayer films of fullerene–diaminododecane on (MeO)Si(CH_3)$_2$(CH2)$_4$$NH_2$–modified oxide surfaces. *Langmuir*, **71**, 2063–2064 (1995).

[Benoit1953] H. Benoit and P. Doty. Light scattering from non–gaussian chains. *J. Phys. Chem.*, **57**, 958–963 (1953).

[Berndt1992] P. Berndt, K. Kurihara, and T. Kunitake. Adsorption of poly(styrenesulfonate) onto an ammonium monolayer on mica: A surface forces study. *Langmuir*, **8**, 2486–2490 (1992).

[Bhushan2004] B. Bhushan. *Springer Handbook of Nanotechnology.* Springer, Berlin (2004).

[Biesalski2002] M. Biesalski, J. Rühe, R. Kügler, and W. Knoll. Polyelectrolytes at solid surfaces: Multilayers and brushes. In S. K. Tripathy, J. Kumar, and H. S. Nalwa, editors, *Handbook of polyelectrolytes and their applications Volume 1: Polyelectrolyte–based multilayers, self–assemblies and nanostructures*, pages 39–63. American Scientific Publishers (2002).

[Binnig1986] G. Binnig, C. F. Quate, and C. Gerber. Atomic force microscopy. *Phys. Rev. Lett.*, **56**, 930–933 (1986).

[Block2007] S. Block and C. A. Helm. Measurement of long–ranged steric forces between polyelectrolyte layers physisorbed from 1 M NaCl. *Phys. Rev. E*, **76**, 030801 (2007).

[Block2008] S. Block and C. A. Helm. Conformation of poly(styrene sulfonate) layers physisorbed from high salt solution studied by force measurements on two different length scales. *J. Phys. Chem. B*, **112**, 9318–9327 (2008).

[Block2009] S. Block and C. A. Helm. Single polyelectrolyte layers adsorbed at high salt conditions: polyelectrolyte brush domains coexisting with flatly adsorbed chains. *Macromol.*, **42**, 6733–6740 (2009).

[Bogdanovic2002] G. Bogdanovic, T. Sennerfors, B. Zhmuda, and F. Tiberga. Formation and structure of polyelectrolyte and nanoparticle multilayers: Effect of particle characteristics. *J. Col. and Interf. Sci.*, **255**, 44–51 (2002).

[Born1999] M. Born and E. Wolf. *Principles of Optics: Electromagnetic Theory of Propagation, Interfarence and Diffraction of Light*. Cambridge University Press, Cambridge (1999).

[Boström2004] M. Boström, D. R. M. Williams, and B. W. Ninham. Why the properties of proteins in salt solutions follow a Hofmeister series. *Curr. Opin. Col. and Interf. Sci.*, **9**, 48–52 (2004).

[Bronstein2000] I. N. Bronstein, K. A. Semendjajew, G. Musiol, and H. Mühlig. *Taschenbuch der Mathematik*. Harri Deutsch, Frankfurt a. M. (2000).

[Büscher2002] K. Büscher, K. Graf, H. Ahrens, and C. A. Helm. Influence of adsorption conditions on the structure of polyelectrolyte multilayers. *Langmuir*, **18**, 3585–3591 (2002).

[Butt2003] H. J. Butt, K. Graf, and M. Kappl. *Physics and chemistry of interfaces*. Wiley, Weinheim (2003).

[Cacace1997] M. G. Cacace, E. M. Landau, and J. Ramsden. *J. Q. Rev. Biophys.*, **30**, 241–277 (1997).

[Cho2001] J. Cho, K. Char, J.-D. Hong, and K.-B. Lee. Fabrication of highly ordered multilayer films using a spin self–assembly method. *Adv. Mat.*, **13**, 1076–1078 (2001).

[Cho2005] J. Cho, K. Char, J.-D. Hong, and K.-B. Lee. Polyelectrolyte–mediated surface interactions (WP_4). *Adv. Colloid Interface Sci.*, **173**, 114–115 (2005).

[Christenson1992] H. K. Christenson. In M. E. Schrader and G. Loeb, editors, *Modern Approaches to Wettability: Theory and Applications*, page 29. Plenum Press (1992).

[Cornelsen2008] M. Cornelsen. *Dissertation*. Greifswald (2008).

[Dähne2001] L. Dähne, S. Leporatti, E. Donath, and H. Möhwald. Fabrication of micro reaction cages with tailored properties. *J. Am. Chem. Soc.*, **123**, 5431–5436 (2001).

[Daillant2009] J. Daillant and A. Gibaud, editors. *X–ray and Neutron Reflectivity: Principles and Applications*. Springer, Berlin (2009).

[Decher1991] G. Decher and J.-D. Hong. Buildup of ultrathin multilayer films by a self-assembly process: Consecutive adsorption of anionic and cationic bipolar amphiphiles on charged surfaces. *Makromol. Chem. Macromol. Symp.*, **46**, 321–327 (1991).

[Decher1997] G. Decher. Fuzzy nanoassemblies: Toward layered polymeric multicomposites. *Science*, **218**, 1232–1237 (1997).

[Déjugnat2007] C. Déjugnat, K. Köhler, M. Dubois, G. B. Sukhorukov, H. Möhwald, T. Zemb, and P. Guttmann. Membrane densification of heated polyelectrolyte multilayer capsules characterized by soft X-ray microscopy. *Adv. Mater.*, **19**, 1331–1336 (2007).

[Demtröder2005] W. Demtröder, editor. *Experimentalphysik 3: Atome, Moleküle und Festkörper*. Springer, Berlin (2005).

[Dill2003] K. A. Dill and S. Bromberg. *Molecular driving forces: Statistical thermodynamics in chemistry and biology*. Garland Science, New York (2003).

[Donath1998] E. Donath, G. B. Sukhorukov, S. A. Davis F. Caruso, and H. Möhwald. Neuartige Polymerhohlkörper durch Selbstorganisation von Polyelektrolyten auf kolloidalen Templaten. *Angew. Chem.*, **110**, 2323–2327 (1998).

[Drake2006] G. W. F. Drake, editor. *Handbook of Atomic, Molecular, and Optical Physics*. Springer, Würzburg (2006).

[Dubas1999] S. T. Dubas and J. B. Schlenoff. Factors controlling the growth of polyelectrolyte multilayers. *Macromol.*, **32**, 8153–8160 (1999).

[Eck2001] D. Eck and C. A. Helm. Plasmon Resonance Measurements of the Adsorption and Adsorption Kinetics of a Biopolymer onto Gold Nanocolloids. *Langmuir*, **17**, 957–960 (2001).

[Elzbieciak2008] M. Elzbieciak, M. Kolasinska, and P. Warszynsky. Characteristics of polyelectrolyte multilayers: The effect of polyion charge on thickness and wetting properties. *Col. and Surf. A*, **321**, 258–261 (2008).

[Fou1996] A. C. Fou, O. Onisuka, M. Ferreira, and M.F. Rubner. Fabrication and properties of light-emitting diodes based on self-assembled multilayers of poly(phenylene vinylene). *J. Appl. Phys.*, **79**, 7501–7509 (1996).

[Fragnetto-Cusani2001] G. Fragnetto-Cusani. Neutron reflectivity at the solid/liquid interface: exmples of applications in biophysics. *J. Phys.: Condens. Matter*, **13**, 4973–4989 (2001).

[Giessibl2003] F. J. Giessibl. Advances in atomic force microscopy. *Reviews of Modern Physics*, **75**, 949–983 (2003).

[Gopinadhan2005] M. Gopinadhan, H. Ahrens, J.-U. Günther, R. Steitz, and C. A. Helm. Approaching the precipitation temperature of the deposition solution and the effects on the internal order of polyelectrolyte multilayers. *Macromol.*, **38**, 5228–5235 (2005).

[Gopinadhan2007a] M. Gopinadhan. *Preparation and Characterization of Nano–composite Films*. Doctoral thesis, Greifswald (2007).

[Gopinadhan2007b] M. Gopinadhan, O. Ivanova, H. Ahrens, J.-U. Günther, R. Steitz, and C. A. Helm. The influence of secondary interactions during the formation of polyelectrolyte multilayers: layer thickness, bound water and layer interpenetration. *J. Phys. Chem. B*, **111**, 8426–8434 (2007).

[Görnitz1997] E. Görnitz, M. Hahn, W. Jaeger, and H. Dautzenberg. Sedimentation equilibrium studies of synthetic polyelectrolytes by means of interface optical methods. *Progr. Coll. Polym. Sci*, **107**, 127–135 (1997).

[Haller1978] I. Haller. Covalently attached organic monolayers on semiconductor surfaces. *J. Am. Chem. Soc.*, **100**, 8050–8055 (1978).

[Hamley1994] I. W. Hamley and J. S. Pedersen. Analysis of neutron and X–ray reflectivity data: Theory. *J. Appl. Cryst.*, **27**, 29–35 (1994).

[Heilmann2003] A. Heilmann. *Polymer films with embedded metal nanoparticles*. Springer, Heidelberg (2003).

[Hiller2002] J. Hiller, J. D. Mendelsohn, and M. F. Rubner. Reversibly erasable nanoporous anti-reflection coatings from polyelectrolyte multilayers. *Nat. Mat.*, **1**, 59–63 (2002).

[Hollas2004] J. M. Hollas. *Modern Spectroscopy*. Wiley, Weinheim (2004).

[Holzmann2007] J. Holzmann, R. Ludwig, A. Geiger, and D. Paschek. Pressure and Salt Effects in Simulated Water: Two Sides of the Same Coin? *Angew. Chem. Int. Ed.*, **46**, 8907–8911 (2007).

[Hübsch2004] E. Hübsch, V. Ball, B. Senger, G. Decher, J. C. Voegel, and P. Schaaf. Controlling the growth regime of polyelectrolyte multilayer films: Changing from exponential to linear growth by adjusting the composition of polyelectrolyte mixtures. *Langmuir*, **20**, 1980–1985 (2004).

[Huff2009] H. Huff, editor. *Into the Nano Era: Moore's Low and Beyond Planar Silicon CMOS*. Springer, Berlin (2009).

[Iler1966] R. K. Iler. Multilayers of colloidal particles. *J. Col. Interf. Sci.*, **21**, 569–594 (1966).

[Israelachvili1992] J. Israelachvili. *Intermolecular and surface forces, 2nd ed.* Academic, London (1992).

[Ivanova2007] O. Ivanova, O. Soltwedel, M. Gopinadhan, J.-U. Günter, M. Cornelsen, R. Steitz, and C. A. Helm. Internal order and water content of polyelectrolyte multilayers. *BENSC experimental report*, (2007).

[Ivanova2008] O. Ivanova, O. Soltwedel, M. Gopinadhan, R. Köhler, R. Steitz, and C. A. Helm. Immobile light water and proton–deuterium exchange in polyelectrolyte multilayers. *Macromol.*, **41**, 7179–7185 (2008).

[Jaber2006] J. A. Jaber and J. B. Schlenoff. Recent developments in the properties and applications of polyelectrolyte multilayers. *Curr. Opin. Col. and Interf. Sci.*, **11**, 324–329 (2006).

[Jean1999] M. Saint Jean, S. Hudlet, C. Guthmann, and J. Berger. Van der Waals and capacitive forces in atomic force microscopies. *J. Appl. Phys.*, **86**, 5245–5249 (1999).

[Jessel2003] N. Jessel, F. Atalar, P. Lavalle, J. Mutterer, G. Decher, P. Schaaf, J.-C. Voegel, and J. Ogier. Bioactive Coatings Based on a Polyelectrolyte Multilayer Architecture Functionalized by Embedded Proteins. *Adv. Mat.*, **15**, 692–695 (2003).

[Joanny1999] J. F. Joanny. Polyelecrolyte adsorption and charge inversion. *Eur. Phys. J. B*, **9**, 117–122 (1999).

[Jones1999] R. A. L. Jones and R. W. Richards. *Polymers at Surfaces and Interfaces*. Cambridge University Press, Cambridge (1999).

[Jones2002] R. A. L. Jones. *Soft condensed matter*. Oxford University Press, Oxford (2002).

[Kleman2003] M. Kleman and O. D. Lavrentovich. *Soft Matter Physics: An Introduction*. Springer, New York (2003).

[Klitzing2003] R.v. Klitzing, J. E. Wong, S. Schemmel, and R. Steitz. Is there an odd/even effect of the water content of polyelectrolyte multilayers? *BENSC Annual Reports*, **1**, 145–146 (2003).

[Klitzing2004] R.v. Klitzing, J. E. Wong, W. Jaeger, and R. Steitz. Short range interactions in polyelectrolyte multilayers. *Curr. Opin. in Coll. and Interf. Sci*, **9**, 158–162 (2004).

[Klitzing2006] R.v. Klitzing. Internal structure of polyelectrolyte multilayer assemblies. *Phys. Chem. Chem. Phys.*, **8**, 5012–5033 (2006).

[Köler2009] R. Köler, I. Dönch, P. Ott, A. Laschewsky, A. Fery, and R. Krastev. Neutron reflectometry study of swelling of polyelectrolyte multilayers in water vapors: Influence of charge density of the polycation. *Langmuir*, **25**, 11576–11585 (2009).

[Kotelyanskii2004] M. Kotelyanskii and D. N. Theodorou, editors. *Simulation Methods for Polymers*. Marcel Dekker, New York (2004).

[Kreibig1995] U. Kreibig and M. Vollmer. *Optical Properties of Metal Clusters*. Springer–Verlag, Berlin (1995).

[Kügler2002] R. Kügler, J. Schmitt, and W. Knoll. The swelling behavior of polyelectrolyte multilayers in air of different relative humidity and in water. *Macromol. Chem. Phys.*, **203**, 413–419 (2002).

[Kunz2004] W. Kunz, P. Lo Nostro, and B. W. Ninham. The present state of affairs with Hofmeister effect. *Curr. Opin. in Coll. and Interf. Sci*, **9**, 1–18 (2004).

[Ladam2000] G. Ladam, P. Schaad, J. C. Voegel, P. Schaaf, G. Decher, and F. Cuisinier. In situ determination of the structural properties of initially deposited polyelectrolyte multilayers. *Langmuir*, **16**, 1249–1255 (2000).

[Lee1982] P. C. Lee and D. Meisel. Adsorption and surface–anhanced raman of dye on silver and gold sols. *J. Phys. Chem.*, **86**, 3391–3395 (1982).

[Lide2003] D. R. Lide, editor. *CRC Handbook of Chemistry and Physics,* 84^{th} *edition.* CRC Press, USA (2003).

[Lifshin1999] E. Lifshin, editor. *X–ray characterization of materials.* Wiley-VCH, Weinheim (1999).

[Lösche1998] M. Lösche, J. Schmitt, G. Decher, W.G. Bouwman, and K. Kjaer. Detailed structure of molecularly thin polyelectrolyte multilayer films on solid substrates as revealed by neutron reflectometry. *Macromol.*, **31**, 8893–8906 (1998).

[Lowack1998] K. Lowack and C.A. Helm. Molecular mechanisms controlling the self–assembly process of polyelectrolyte multilayers. *Macromol.*, **34**, 823–833 (1998).

[Lu2007] C. Lu, H. Mohwald, and A. Fery. Plasmon resonance tunable by deaggregation of gold nanoparticles in multilayers. *J. Phys. Chem.*, **111**, 10082–10087 (2007).

[Lvov1995] Y. Lvov, K. Ariga, I. Ichinose, and T. Kunitake. Assembly of multicomponent protein films by means of electrostatic layer-by-layer adsorption. *J. Am. Chem. Soc.*, **117**, 6117–6123 (1995).

[Marra1983] J. Marra, H. A. van der Schee, G. J. Fleer, and J. Lyklema. *Adsorption from solution.* Academic Press, New York (1983).

[Mattox2003] D. M. Mattox. *The foundations of vacuum coating technology.* Noyes Publications, New York (2003).

[Mie1908] G. Mie. Beiträge zur Optik trüber Medien, speziell kolloidaler Metallösungen. *Ann. Phys.*, **25**, 377–445 (1908).

[Mironov2004] V. L. Mironov. *Fundamentals of Scanning Probe Microscopy.* NT-MDT, Nizhniy Novgorod (2004).

[Neff2006] P. A. Neff, A. Naji, C. Ecker, B. Nickel, R. v. Klitzing, and A. R. Bausch. Electrical detection of self–assembled polyelectrolyte multilayers by a thin film resistor. *Macromol.*, **39**, 463–466 (2006).

[Netz1999] R. R. Netz and J.-F. Joanny. Complexation between a semiflexible polyelectrolyte and an oppositely charged sphere. *Macromol.*, **32**, 9026–9040 (1999).

[Netz2003] R. R. Netz and D. Andelman. Neutral and charged polymers at interfaces. *Phys. Rep.*, **380**, 1–95 (2003).

[Nicol2003] E. Nicol, J.-L. Habib-Jiwan, and A. M. Jonas. Polyelectrolyte multilayers as nanocontainers for functional hydrophilic molecules. *Langmuir*, **19**, 6178–6186 (2003).

[Notea2006] C. Notea, S. Kosmellaa, and J. Koetz. Poly(ethyleneimine) as reducing and stabilizing agent for the formation of gold nanoparticles in w/o microemulsions. *Colloids Surf. A*, **290**, 150–156 (2006).

[Okubo1999] T. Okubo and M. Suda. Absorption of polyelectrolytes on colloidal surfaces as studied by electrophoretic and dynamic light-scattering techniques. *J. Col. and Interf. Sci.*, **213**, 565–571 (1999).

[Oura2003] K. Oura, V. G. Lifshits, A. A. Saranin, A. V. Zotov, and M. Katayama. *Surface Science: An Introduction*. Springer, Berlin (2003).

[Overbeek1976] J. Th. G. Overbeek. Polyelectrolytes, past, present and future. *Pure and Appl. Chem.*, **46**, 91–101 (1976).

[Parka2005] H. B. Parka, H.-S. Shinb, Y. Moo Leea, and J.-W. Rhim. Annealing effect of sulfonated polysulfone ionomer membranes on proton conductivity and methanol transport. *J. of Membr. Sci.*, **247**, 103–110 (2005).

[Parratt1954] L.G. Parratt. Surface studies of solids by total reflection of X-Rays. *Phys. Rev.*, **95**, 359–369 (1954).

[Parsegian1995] V. A. Parsegian. Hopes for Hofmeister. *Nature*, **378**, 335–336 (1995).

[Pauleau2002] Y. Pauleau, editor. *Chemical Physics of Thin Film Deposition Process for Micro- and Nano–Technologies*. Kluwer Academic Publishers, Dordrecht (2002).

[Paulo2002] Á. S. Paulo and R. García. Unifying theory of tapping-mode atomic-force microscopy. *Phys. Rev. B*, **66**, 041406 (2002).

[Pedersen1994] J. S. Pedersen and I. W. Hamley. Analysis of neutron and X–ray reflectivity data. II. Constrained least–squares methods. *J. Appl. Cryst.*, **27**, 36–49 (1994).

[Penfold2000] J. Penfold. Neutron scattering for surface characterization. *Current Science*, **78**, 1458–1466 (2000).

[Pericet-Camara2006] R. Pericet-Camara, G. Papastavrou, S. H. Behrens, C. A. Helm, and M. Borkovec. Interaction forces and molecular adhesion between pre–adsorbed poly (ethylene imine) layers. *J. Colloid and Interface Sci.*, **296**, 496–506 (2006).

[Reinhardt2008] K. A. Reinhardt and W. Kern, editors. *Handbook of Silicon Wafer Cleaning Technology, sec. ed.* William Andrew, New York (2008).

[Rubinstein1989] I. Rubinstein, S. Steinberg, Y. Tor, A. Shanzer, and J. Sagiv. Selective action of artificial membranes. *Nature*, **337**, 426–429 (1989).

[Salomäki2003] M. Salomäki, K. Loikas, and J. Kankare. Effect of polyelectrolyte multilayers on the response of a quartz crystal microbalance. *Anal. Chem.*, **75**, 5895–5904 (2003).

[Salomäki2004a] M. Salomäki, T. Laiho, and J. Kankare. Counteranion–controlled properties of polyelectrolyte multilayers. *Macromol.*, **37**, 9585–9590 (2004).

[Salomäki2004b] M. Salomäki, T. Laiho, and J. Kankare. The Hofmeister Anion Effect and the Growth of Polyelectrolyte Multilayers. *Langmuir*, **20**, 3679–3683 (2004).

[Salomäki2005] M. Salomäki, I. A. Vinokurov, and J. Kankare. Effect of temperature on the buildup of polyelectrolyte multilayers. *Langmuir*, **21**, 11232–11240 (2005).

[Schlenoff1998] J. B. Schlenoff, H. Ly, and M. Li. Charge and Mass Balance in Polyelectrolyte Multilayers. *J. Am. Chem. Soc.*, **120**, 7626–7634 (1998).

[Schlenoff2000] J. B. Schlenoff, S. T. Dubas, and T. Farhat. Sprayed polyelectrolyte multilayers. *Lagmuir*, **16**, 9968–9969 (2000).

[Schmidt2005] W. Schmidt. *Optical Spectroscopy in Chemistry and Life Sciences.* Wiley-VCH, Darmstadt (2005).

[Schmitt1996] J. Schmitt. *Dissertation.* Mainz (1996).

[Schmitt1997] J. Schmitt, G. Decher, W. J. Dressick, S. L. Brandow, R. E. Geer, R. Shashidhar, and J. M. Calvert. Preparation and optical properties of colloidal gold monolayer. *Adv. Mater.*, **9**, 61–65 (1997).

[Schmitt1999] J. Schmitt, P. Mächtle, D. Eck, H. Möhwald, and C. A. Helm. Preparation and optical properties of colloidal gold monolayer. *Langmuir*, **15**, 3256–3266 (1999).

[Schöler2002] B. Schöler, G. Kumaraswamy, and F. Caruso. Investigation of the influence of polyelectrolyte charge density on the formation of multilayer thin film prapared by the layer–by–layer technique. *Macromol.*, **35**, 889–897 (2002).

[Schönhoff2003a] M. Schönhoff. Layered polyelectrolyte complexes: Physics of formation and molecular properties. *J. Phys.: Condens. Mat.*, **15**, R1781–R1808 (2003).

[Schönhoff2003b] M. Schönhoff. Self–assembled polyelectrolyte multilayers. *Curr. Opin. Col. and Interf. Sci.*, **8**, 86–95 (2003).

[Schönhoff2007] M. Schönhoff, V. Ball, A. R. Bausch, C. Dejugnat, N. Delorme, K. Glinel, R. v. Klitzing, and R. Steitz. Hydration and internal properties of polyelectrolyte multilayers. *Col. Surf. A*, **303**, 14–29 (2007).

[Sharpe2008] W. N. Sharpe, editor. *Handbook of Experimental Solid Mechanics.* Springer, New York (2008).

[Shiratori2000] S. S. Shiratori and M. Rubner. pH-Dependent Thickness Behavior of Sequentially Adsorbed Layers of Weak Polyelectrolytes. *Macromol.*, **33**, 4213–4219 (2000).

[Sommer1989] L. Sommer. *Analytical absorption spectrophotometry in the visible and ultraviolet: The principles.* Elsevier Science Ltd, Budapest (1989).

[Steitz2000] R. Steitz, V. Leiner, R. Siebrecht, and R.v. Klitzing. Influence of the ionic strength on the structure of polyelectrolyte films at the solid/liquid interface. *Col. Surf. A*, **163**, 63–70 (2000).

[Stockton1997] W. B. Stockton and M. Rubner. Molecular–level processing of conjugated polymer. *Macromol.*, **30**, 2717–2725 (1997).

[Strobl1996] G. Strobl. *The Physics of Polymers, 2nd ed.* Springer, Berlin (1996).

[Stuart1991] M. A. C. Stuart, G. J. Fleer, J. Lyklema, W. Norde, and J. M. H. M. Scheutjens. *Adv. Col. Interf. Sci.*, **34**, 477 (1991).

[Sukhorukov1998] G. B. Sukhorukov, E. Donath, H. Lichtenfeld, E. Knippel, M. Knippel, A. Budde, and H. Möwald. Layer-by-layer self assembly of polyelectrolytes on colloidal particles. *Col. Surf. A*, **137**, 253–266 (1998).

[Tan2003] H. L. Tan, M. J. McMurdo, G. Q. Pan, and P. G. Van Patten. Temperature dependence of polyelectrolyte multilayer assembly. *Langmuir*, **19**, 9311–9314 (2003).

[Tanford1980] C. Tanford. *The hydrophobic effect: Formation of micelles and biological membranes, 2nd ed.* Wiley, New York (1980).

[Tieke2000] B. Tieke, F. van Ackern, L. Krasemann, and A. Toutianoush. Ultrathin self-assembled polyelectrolyte multilayer membranes. *Eur. Phys. J. E*, **5**, 29–39 (2000).

[Tolan1999] M. Tolan. *X–ray Scatering from Soft–Matter Thin Films.* Springer, Heidelberg (1999).

[Torikai2007] N. Torikai, N. L. Yamada, A. Noro, M. Harada, D. Kawaguchi, A. Takano, and Y. Matsushita. Ultrathin self-assembled polyelectrolyte multilayer membranes. *Neutron reflectometry on interfacial structures of the thin films of polymer and lipid*, **39**, 1238–1246 (2007).

[Ulman1991] A. Ulman. *An introduction to ultrathin organic films: From Langmuir–Blodgett to self–assembly.* Academic Press, San Diego (1991).

[van der Lee2007] A. van der Lee, F. Salahb, and B. Harzallahb. A comparison of modern data analysis methods for X–ray and neutron specular reflectivity data. *J. Appl. Cryst.*, **40**, 820–833 (2007).

[Villarrubia1994] J. Villarrubia. Morphological estimation of tip geometry for scanned probe microscope. *Surf. Sci.*, **321**, 287–300 (1994).

[Williams1996] P. M. Williams, K. M. Shakesheff, M. C. Davies, D. E. Jackson, C. J. Robers, and S. J. B. Tendler. Blind reconstruction of scanning probe microscope image data. *J. Vac. Sci. Technol.*, **B14**, 1557–1562 (1996).

[Wittmera2007] C. R. Wittmera, J. A. Phelpsa, W. M. Saltzmanb, and Paul R. Van Tassela. Fibronectin terminated multilayer films: Protein adsorption and cell attachment studies. *Biomat.*, **28**, 851–860 (2007).

[Wong2004] J. Wong, F. Rehfeldt, P. Hänni, M. Tanaka, and R.v. Klitzing. Swelling behavior of polyelectrolyte multilayers in saturated water vapor. *Macromol.*, **37**, 7285–7289 (2004).

[Zabel1994] H. Zabel. X-ray and neutron reflectivity analysis of thin films and superlattices. *Appl. Phys. A*, **58**, 159–168 (1994).

[Zhai2004] L. Zhai, A. J. Nolte, R. E. Cohen, and M. F. Rubner. pH-Gated Porosity Transitions of Polyelectrolyte Multilayers in Confined Geometries and Their Application as Tunable Bragg Reflectors. *Macromol.*, **37**, 6113–6123 (2004).

[Zhu2007] Y. Zhu and J. Shi. A mesoporous core-shell structure for pH-controlled storage and release of water-soluble drug. *Micro- and Mesoporous Mat.*, **103**, 243–249 (2007).

Acknowledgements

This work would have been impossible without the help of many people and I want to seize this opportunity to thank them.

Without my academic advisor, Prof. Christiane A. Helm, who has been providing me with her support and guidance for all these years, this thesis would not have come into being. I am very grateful for all her valuable critique and emotional feedback, that changed me and my view of things.

I would like to thank all members of Prof. C. A. Helm's group, previous and current for their contribution. Special thanks to Dr. Heiko Ahrens (and his magic hands), Dr. Manesh Gopinadhan, Dr. Jens–Uwe Günther, Stephan Block, Matthias Cornelsen and Peter Nestler. I appreciate your time and your patience. I also thank for the help and excellent support provided by Jana Freitag, Hans–Joachim Schmidt and Frank Scheffter.

Many thanks to all coauthors and collaborators, especially to Prof. Rainer Hippler, Dr. Roland Steitz, Dr. Ralf Köhler, Dr. Harm Wulff, Dr. Marion Quass, Dr. Shyjumon Ibrahimkutty and Dr. Matthis Höhne. Special thanks to Helmholtz Centre for Materials and Energy, former Hahn-Meitner-Institut, Berlin and International Max–Planck Research School of Bounded Plasma, Greifswald.

I thank Dr. Robert Kourist and his family, Dr. Svetlana Gurevich, Dr. Vasile Vartolomei, Vladimir Sushkov, Sergey Stepanov, Marina Ganeva, Vladimir Danilov and all of those unique people I just can't name here for their help and emotional support. Very special thanks to Dr. Evgeny Gurevich and Dr. Noelle Walsh for their reading this manuscript.

I would like to express here my gratitude to Olaf Soltwedel – my colleague and the father of my child, – for all his understanding and patience during the period of my work on this thesis. I cannot underestimate both his professional and personal input that helped this work to be written.

Finally, I would like to thank my committee members.

Lebenslauf

Persönliche Daten:

Name:	Oxana Ivanova
Geburtsdatum:	06.04.1980
Geburtsort:	Sankt-Petersburg, Russland

Schulbildung:

09/1987 – 06/1997	Städtische Oberschule Nr. 292, Sankt-Petersburg, Russland

Studium:

09/1997 – 02/2004	Physikstudium an der Staatlichen Universität Sankt-Petersburg, Russland:
06/2001	**Bachelorabschluß**, Thema der Abschlussqualifikationsarbeit: "Messung der absoluten Konzentration von metastabilen $A^3\Sigma$ Stickstoffmolekulen in einem $Ar + N_2$ Plasma".
02/2004	**Masterabschluß**, Thema der Abschlussqualifikationsarbeit: "Studie und Charakteriesierung von aufgedampften organischen Silikonfilmen in einem DBD plasma bei amospharischem Druck".

Tätigkeiten am Institut für Physik der Ernst-Moritz-Arndt Universität:

08/2001 – 12/2001	Stipendiat des DAAD
06/2002 – 11/2002	wissenschaftlicher Hilfskraft
08/2003 – 10/2003	Stipendiat des IAESTE
11/2004 – 09/2007	Stipendiat des Landesgraduiertenkollegs
10/2007 – 12/2009	wissenschaftlicher Mitarbeiter
seit 2005	Mitglied der "Deutschen Physikalischen Gesellschaft (DPG)
seit 2005	Mitglied der "Internationalen Max–Plank Research School of Bounded Plasma (IMPRS)"
seit 2007	Im Sonderforschungsbereich SFB–Transregio 24

Beginn der Dissertation: 15. November 2004 unter der Anleitung von Prof. Dr. C. A. Helm

---

(Oxana Ivanova)

Greifswald, den 10.05.2010

Publications

- Olaf Soltwedel, **Oxana Ivanova**, Peter Nestler, Madlen Müller, Ralf Köhler, and Christiane A. Helm "Interdiffusion in Polyelectrolyte Multilayers" *Macromolecules* 43 (2010) 7288-7293
- Olaf Soltwedel, **Oxana Ivanova**, Matthias Höhne, Manesh Gopinadhan, and Christiane A. Helm "Aggregation and Rearrangement within a Silver Nanoparticle Layer during Polyelectrolyte Multilayer Formation" *Langmuir* (2010)
- **Oxana Ivanova**, Olaf Soltwedel, Manesh Gopinadhan, Ralf Köhler, Roland Steitz, and Christiane A. Helm "Strong Binding of Light Water and Proton–Deuterium Exchange in Polyelectrolyte Multilayers" *Macromolecules* 41 (2008) 7179-7185
- Marion Quaas, Harm Wulff, **Oxana Ivanova**, Christiane A. Helm "Plasma chemical reactions of thin nickel films" *Surf. Interface Anal.* 40 (2008) 552-555
- Marion Quaas, **Oxana Ivanova**, Harm Wulff, and Christiane A. Helm "Influence of reactive plasmas on thin Ni-films" *Z. Kristallogr. Suppl.* 27 (2008) 295-302
- Manesh Gopinadhan, **Oxana Ivanova**, Heiko Ahrens, Jens–Uwe Günther, Roland Steitz, and Christiane A. Helm "The Influence of Secondary Interactions during the Formation of Polyelectrolyte Multilayers: Layer Thickness, Bound Water and Layer Interpenetration" *J. Phys. Chem. B* 111 (2007) 8426–8434
- Shyjumon Ibrahimkutty, Manesh Gopinadhan, **Oxana Ivanova**, Marion Quaas, Harm Wulff, Christiane A. Helm, and Rainer Hippler "Structural deformation and lattice parameter studies of size selected silver clusters" *Eur. Phys. J. D* 37 (2006) 409–415

Conference Contribution

- Olaf Soltwedel, **Oxana Ivanova**, Madlen Müller, Ralf Köhler, and Christiane A. Helm "Block Architecture for Neutron Reflectivty Investigation of Internal Interfaces of Polyelectrolyte Multilayers".
  Harm Wulff, Marion Quaas, Heiko Ahrens, **Oxana Ivanova**, and Christiane A. Helm "Formation of palladium hydrides in low temperature Ar/H2-plasma".
  DPG Spring Meeting, Regensburg, Germany, March 21–26, 2010.

- **Oxana Ivanova** et. al. "Immobile Light Water and Proton–Deuterium Exchange in Polyelectrolyte Multilayers" (oral presentation).
  Marion Quaas, Heiko Ahrens, **Oxana Ivanova**, Harm Wulff, and Christiane A. Helm "Formation of metal hydrides of 8b elements under plasma exposure".
  DPG Spring Meeting, Dresden, Germany, March 22–27, 2009.

- Harm Wulff, Marion Quaas, **Oxana Ivanova**, and Christiane A. Helm "Formation of nikel hydrides in reactive plasmas".
  European Powder Diffraction Conference (EPDIC-11), Warsaw, Poland, September 18–22, 2008.

- **Oxana Ivanova**, Manesh Gopinadhan, Olaf Soltwedel, Roland Steitz, and Christiane A. Helm "Isotope Effects in Partially Deuterated Polyelectrolyte Multilayers".
  Oxana Ivanova, Olaf Soltwedel, Manesh Gopinadhan, Jens-Uwe Günther, Matthias Cornelsen, Roland Steitz, and Chrstiane A. Helm "Water incorporation in poylectrolyte multilayers: Hofmeister effect?".
  Marion Quaas, Harm Wulff, **Oxana Ivanova**, and Christiane A. Helm "Zur Bildung von Ni-Hydriden in reaktiven Plasmen".
  72^{th} *Annual Meeting DPG*, Berlin, Germany, February 25–29, 2008.

- **Oxana Ivanova**, Olaf Soltwedel, Manesh Gopinadhan, Jens-Uwe Günther, Matthias Cornelsen, Roland Steitz, and Christiane A. Helm "The influence of temperature and the Hofmeister cation effect on the growth and composition of polyelectrolyte multilayers".
  Manesh Gopinadhan, **Oxana Ivanova**, Heiko Ahrens, Jens-Uwe Günther, Roland Steitz, and Christiane A. Helm "Polyelectrolyte Multilayers: Influence of Secondary Interactions on Internal Order, Layer Thickness & Bound Water".
  International Soft Matter Conference, Aachen, Germany, October 1–4, 2007.

- Marion Quaas, **Oxana Ivanova**, Christiane A. Helm, Harm Wulff "Plasma–chemical reactions of small nickel clusters".

12^{th} *European Conference on Applications of Surface and Interface Analysis*, Brussel, Belgium, September 9–14, 2007.

- Manesh Gopinadhan, **Oxana Ivanova**, Heiko Ahrens, Jens-Uwe Günther, Olaf Soltwedel, Roland Steitz, and Christiane A. Helm "Polyelectrolyte Multilayers: Influence of Secondary Interactions on Internal Order, Layer Thickness & Bound Water".
  14^{th} *BENSC User's Meeting at Helmholtz Centre for Materials and Energy*, Berlin, Germany, May 23–24, 2007.

- Manesh Gopinadhan, **Oxana Ivanova**, Heiko Ahrens, Jens-Uwe Günther, Roland Steitz, and Christiane A. Helm "The Influence of Secondary Interactions during the Formation of Polyelectrolyte Multilayers: Layer Thickness, Bound Water and Layer Interpenetration".
  Marion Quaas, **Oxana Ivanova**, Christiane Helm und Harm Wulff "Ni-Filme in reaktiven Plasmen".
  71^{th} *Annual Meeting DPG*, Regensburg, Germany, March 26–30, 2007.

- **Oxana Ivanova**, Manesh Gopinadhan, Matthias Höhne and Christiane A. Helm "Evidence of nanoparticles aggregation in polyelectrolyte multilayers".
  6^{th} *International Symposium on Polyelectrolytes*, Dresden, Germany, September, 4–8, 2006.

Declaration

Here by I declare that this work has so far neither been submitted to the Faculty of Mathematics and Natural Sciences at the Ernst-Moritz-Arndt-University of Greifswald nor to another scientific institution for the purpose of the degree of doctorate. Furthermore I declare that I have written this work by myself and that I have not used any other resources, other than mentioned earlier in this work.

Hiermit erkläre ich, dass diese Arbeit bisher von mir weder an der Mathematisch–Naturwissenschaftlichen Fakultät der Ernst-Moritz-Arndt-Universität Greifswald noch einer anderen wissenschaftlichen Einrichtung zum Zwecke der Promotion eingereicht wurde. Ferner erkläre ich, dass ich diese Arbeit selbständig verfassst und keine anderen als die darin angegebenen Hilfsmittel benutzt habe.

Oxana Ivanova